Title
Symmetry-Sensitive Optical Probes of Quantum Antiferromagnets

Author
Little, Arielle Ann

Publication Date
2020

Peer reviewed|Thesis/dissertation

Symmetry-Sensitive Optical Probes of Quantum Antiferromagnets

by

Arielle Little

A dissertation submitted in partial satisfaction of the
requirements for the degree of

Doctor of Philosophy

in

Physics

in the

Graduate Division

of the

University of California, Berkeley

Committee in charge:

Professor Joseph Orenstein, Chair
Professor Feng Wang
Professor Sayeef Salahuddin

Spring 2020

Symmetry-Sensitive Optical Probes of Quantum Antiferromagnets

Abstract

Symmetry-Sensitive Optical Probes of Quantum Antiferromagnets

by

Arielle Little

Doctor of Philosophy

University of California, Berkeley

Professor Joseph Orenstein, Chair

Antiferromagnetism (AFM) underlies some of the most fascinating and widely-studied questions in modern condensed matter physics. The work presented here applies the unique capabilities of polarization-resolved optical techniques to the study of phase transitions, magnetic ground states, and excitations in two AFM materials: α-$RuCl_3$ and $Fe_{1/3}NbS_2$. While the motivation for each project is quite different, these two compounds share a few common properties: both are layered materials where the magnetism can be treated as quasi-two dimensional, and both order antiferromagnetically at low temperature and zero applied field. Throughout this dissertation, we will explore how the interesting properties of both systems emerge from the physics of frustrated magnetism.

First, we consider the low-energy magnetic excitations in the Kitaev quantum spin liquid candidate material, α-$RuCl_3$. While this material orders at $T_N = 7$ K in zero applied field, it can be driven into a magnetically disordered phase by the application of an in-plane magnetic field with a critical field $H_c \sim 7.5$ T. In the ordered phase and in zero applied magnetic field, inelastic neutron scattering measurements observed peaks consistent with magnons, in addition to an unusual continuum of scattering centered at zero wave vector. This continuum was found to persist above H_c and was interpreted as a possible signature of fractionalized excitations, begging the question of whether a field-induced spin liquid phase may exist in the vicinity of H_c.

Tracking the evolution of the magnetic excitations in α-$RuCl_3$ is thus of central importance to understanding the proximity of this system to a fractionalized spin liquid. Using time-domain terahertz (THz) spectroscopy, we quantitatively characterize the zero wave vector spectrum of this material in the phase space of temperature, applied field

and THz polarization. Below H_c we observe two sharp single-magnon absorption peaks and two broad multi-magnon peaks on top of a large continuum of absorption. This THz continuum does not depend on temperature or field. By way of spectral weight analysis we attribute this feature largely to electric dipole, rather than magnetic dipole absorption. We find that the spectral weight from magnetic absorption at low energies is largely accounted for by magnons, rather than fractional excitations, and the contribution from a potential magnetic continuum does not grow even approaching H_c. Furthermore, the high resolution of the THz spectra enables close comparison with theoretical models. Below the Nèel temperature and critical field, we find that the essential features of our data are reproduced by calculations based on linear spin wave theory when a C_3-breaking distortion of the honeycomb lattice and the presence of structural domains are taken into account. We quantify the magnon selection rules, identify a low-field crossover transition and provide insight into the values of parameters in the magnetic Hamiltonian describing α-$RuCl_3$.

In the second part of this dissertation, we study the transition metal dichalcogenide (TMD) compound, $Fe_{1/3}NbS_2$, where AFM order arises at T_N $\sim$45 K on a triangular Fe-superlattice intercalated between TMD layers. Notably, current-induced resistance switching and multi-stable memory effects were recently observed in this material when cooled into the magnetic phase. We develop a photo-thermally modulated scanning birefringence microscopy technique which enables the detection of rotational symmetry breaking as as function of temperature and spatial location on the sample. In $Fe_{1/3}NbS_2$ we detect a sudden onset of optical birefringence at T_N, indicating the lowering of C_3 rotational symmetry of the triangular lattice to at most C_2 in the AFM phase. Across the sample surface, we image three distinct orientations of this symmetry-breaking, corresponding to three magnetic-nematic domains which are locked to the crystallographic axes of the Fe- superlattice.

Employing the language of nematic order in crystalline materials developed in the context of the tetragonal Fe-based superconductors, we attribute our observations in $Fe_{1/3}NbS_2$ to a coincident magnetic-nematic phase transition at at the Nèel temperature, albeit on the triangular lattice. Qualitatively, at T_N a distortion along one of the three directions of Fe-Fe bonds relieves the geometric frustration of Ising spins on a triangular lattice, allowing one of three degenerate ordered AFM phases to condense. A phenomenological Landau theory shows that nematicity in this compound is analogous to the three-state Potts model, and is hence described by a distinct Z_3 nematic order parameter. These ideas are then tested by showing that that the domain population, and hence the global nematic director, is continuously tunable by the application of uniaxial strain. This suggests that the anisotropy axes of response functions– for instance the resistivity tensor– can be continuously re-oriented by external perturbations such as strain

or even current or magnetic field. In principle, this coupling to the nematic director could mediate the resistive switching behavior observed in $Fe_{1/3}NbS_2$, indicating it may be of interest to search for AFM switching phenomena in the broad class of nematic-magnetic systems.

ACKNOWLEDGMENTS

This dissertation is the culmination of a long journey in the Berkeley Physics department. After finishing undergrad at Cal, I spent a year in the trenches at CERN before coming back to Berkeley for grad school. Once in grad school I became intrigued by the amazing emergent physics to be found in condensed matter systems, and I liked idea of being able to be involved in every aspect of a table-top experiment. I also knew I wanted to work with optics. With this in mind, I joined the Orenstein lab at somewhat of a turning point in the lab's research direction. As a result I got the awesome opportunity to build up the lab's research capabilities by commissioning new experimental equipment and exploring new materials systems. I soon realized I was also extremely fortunate in getting the opportunity to work under Joe Orenstein's mentorship. Joe is a deep thinker and versatile scientist with the unique ability to contribute meaningfully to both experimental technique development and fundamental theory. He is also, undoubtedly, the Physics-Golf Biathlon World Champion. Thank you Joe.

I am also very grateful to my undergraduate research advisor, Joel Fajans, as well as Will Bertsche who was one of my mentors at CERN. In fact I must acknowledge the entire ALPHA collaboration from the years 2011-2012, who all inspired me to continue in physics. The challenging, incredibly fun, and sometimes harrowing experience of building a new apparatus in an accelerated time frame with you all is something I will never forget.

In grad school I have been fortunate to work with some inspiring colleagues. My lab mates Shreyas Patankar, Eric Thewalt, and Dylan Rees offered great camaraderie, collaboration, and taught me more about politics and other random things than I ever thought I'd learn in physics grad school. Postdoc Liang Wu taught me about THz spectroscopy and mentored me in our work on α-$RuCl_3$. I learned a great deal from working with postdoc Changmin Lee, a talented physicist and wonderful colleague, on our birefringence microscopy and strain projects. I am grateful as well to Ritika Dusad and to the newer lab members Yue Sun, Ronnie Spitzer and Veronika Sunko who I know continue to take the group's research to new levels.

Of course it is the technical staff at the ALS and Building 2 at LBL who keep the research going in the Orenstein lab going smoothly. In particular I'm grateful to Rene Delano, Derrick Crofoot, Rick Bloemhard and the ALS electronics shop for helping me get all the right components together and working to build up the lab. Thanks as well to Gil Torres and Eduardo Flores for keeping Building 2 operational and clean, for the friendly interactions, and for helping me navigate unforeseen logistical and equipment challenges.

I am also grateful to have had the support of several staff scientists at the ALS beam lines for help with x-ray measurements.

I have had the pleasure of working with many collaborators outside of our group. Arnab Banerjee, Paige Kelley, Stephen Nagler and company at ORNL provided us with beautiful α-$RuCl_3$ crystals and worked with us to try and unravel the complicated story of this fascinating material. Erik Aldape and Ehud Altman at Berkeley provided excellent theoretical support. Thanks to Derrick Boone and David Goldhaber-Gordon at Stanford for friendly collaboration and some interesting data. I've also been lucky to collaborate quite a bit with the James Analytis group at Berkeley. In particular Caolan John and Spencer Doyle grew the TMD crystals for the work presented here. It was a pleasure as well to work with Nityan Nair and Eran Maniv. The masters of nematic order, Rafael Fernandes and Jörn Venderbos, helped us put together the story of nematicity in $Fe_{1/3}NbS_2$ with a very nice free energy theory and always answered my questions.

I am grateful to Cliff Hicks, Andy Mackenzie and their groups for hosting me at MPI Dresden in 2016. It was enriching to visit their Institute and learn a little bit about transport measurements and uniaxial strain. Cliff also provided us with a uniaxial strain device which will be used in future measurements in the Orenstein lab.

Thanks to my teaching colleagues in the Physics 111 lab in particular Eric Hunter, Erik Urban, Celeste Carruth, Alexey Drobizhev, Johnathan Ma, Victoria Xu, Sachi Wagaarachchi. Thanks to Don Orlando, now retired, for keeping the 111 lab running for so long. Physics 111 was the course that originally solidified my interest in physics as an undergrad and it was an honor to teach in graduate school. Cheers to the entire entering class of 2013, but in particular to my condensed matter cohort buddies Trinity Joshi, Zahra Pedramrazi, Halleh Balch and Stephanie Mack who navigated grad school with me. Thanks to everyone who worked on SWPS events with me– in particular Simca Bouma, Slyvia Lewin, Clio Sleator, and QinQin Yu. In the Berkeley Physics department, I'd also like to thank Claudia Trujillo, Joelle Miles, Donna Sakima, Anne Takizawa, Stephen Pride Raffel, Anthony Vitan, and Carlos Bustamante.

Thanks to all my housemates at Blake Street for the camaraderie, commiseration, and good advice. I am grateful also to many people from outside of the physics world, in particular my friends from undergrad and the Berkeley Student Co-ops who have stuck with me through the years. Thanks to my great friends in the NCNCA and on the Cal Cycling team. In fact was the grad students on Cal Cycling who first told me as an undergrad that I too could be a scientist. My cycling teammates have mentored me in a professional context as well in bike racing. Thanks for always letting me draft you.

Finally, of course thanks to my family for all of the love and support.

CONTENTS

LIST OF FIGURES

ABBREVIATIONS

THZ Terahertz

TDTS Time-Domain Terahertz Spectroscopy

OAP Off-Axis Parabolic mirrors

FFT Fast Fourier Transform

FTIR Fourier Transform Infrared Spectroscopy

QSL Quantum Spin Liquid

KSL Kitaev Spin Liquid

SOC Spin-Orbit Coupling

LSWT Linear Spin Wave Theory

TMD Transition Metal Dichalchogenide

1

INTRODUCTION

> "A large number of antiferromagnetic materials is now known... They are extremely interesting from the theoretical viewpoint, but do not seem to have any applications."
>
> –Louis Néel, Nobel Prize Lecture, December 11, 1970

Spontaneous magnetization refers to the ordering of magnetic moments below some transition temperature, in the absence of an applied field. Ordered magnetic states in solids arise from the alignment of electron spins (magnetic moments) localized on the crystalline lattice cites. Ferromagnetism (FM) describes a configuration where the prefer spins align below a Curie temperature T_C. In antiferromagnets (AFMs) spins prefer to be anti-aligned below a Néel temperature T_N and the ordered phase is periodic modulations of magnetic moment, or a spin density wave.

Now, antiferromagnetism is well-studied topic. It is covered in its most basic form in many introductory texts and has become a part of our elementary vocabulary as condensed matter physicists. However, when it was first experimentally detected in the 1930s [1], it was somewhat of a mystery[1] [9]. At the time, phase transitions in FMs were understood to obey the Curie-Weiss law for magnetic susceptibility:

$$\chi = \frac{C}{T - T_c} \tag{1.1}$$

Which was derived, originally from classical thermodynamic arguments which considered the response of paramagnetic electron moments to a mean dipolar field (see Weiss molecular field model below). This model accurately predicts the phase transition in a FM: when spontaneous magnetization sets, i.e. the spins align, χ becomes divergent at at T_c.

There are of course many magnetic materials which do not obey this law– including some paramagnetic metals and of course AFMs. As such materials were discovered, new

1 This discussion was inspired by a seminar given by Prof. Nicola Spaldin in 2019, where she referred to AFM as a "hidden order," see Ref. [9]

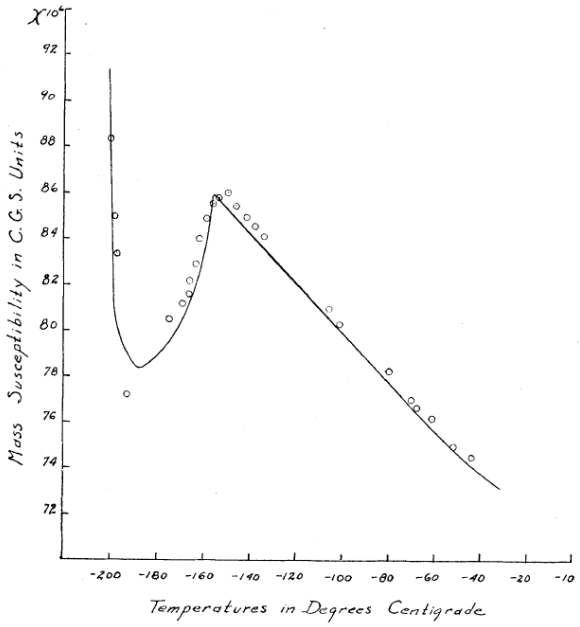

Figure 1.1: A beautifully hand-drawn plot showing the magnetic susceptibility of antiferromagnetic MnO as a function of temperature, at the time a surprising result. Reprinted Figure with permission from Ref. [1] as follows: Rayen Welch Tyler, Physical Review, volume 44, page 776, November 1st, 1933. Copyright 1933 by the American Physical Society.

theoretical descriptions clearly became necessary. As Louis Néel describes in his Nobel lecture: "At this time... The existence of the straight Curie-Weiss lines in the ($1/\chi$, T) representation was so well-established that when an experiment gave a curve it was rather preferred to break it down into a series of of straight lines, each corresponding to a different magnetic state obeying the Curie-Weiss law." [10]. Even now, there is much to be learnt from that.

One such early measurement, on the cubic material MnO, resulted in the susceptibility curve in Fig. 1.1 which was soberly reported by Rayen Tyler in Physical Review in 1933 [1]. Evidently, this curve comes to a cusp instead of a divergence– now we know this as the susceptibility for an AFM [11] but at the time it didn't make sense within the Weiss Molecular field idea. This curve obeys the Curie-Weiss law up until -155 C (that is about 118 K) but the Curie temperature would be negative. How could the average molecular field be negative? From the point of view of the lab bench, also, one can imagine that this curve must have seemed quite mysterious. Ferromagnets may be trained by a relatively small applied external field; the bulk magnetization properties presented here

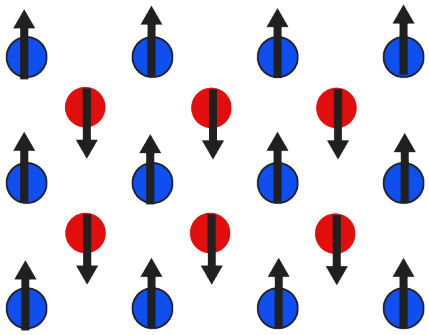

Figure 1.2: Cartoon of two ferromagnetic sublattices A (blue) and B (red) which are antiferromagnetically coupled to one another.

may have seemed strangely quite robust. What's more, neutron scattering had not yet been developed.

The resolution to this mystery is of course the development for which Louis Néel shared the Nobel Prize in 1970. Starting out by considering fluctuations in the molecular field, he eventually realized that the negative Curie temperature could described by negative exchange interactions between local spins. This may arise if the spins are arranged on two sublattices A and B which spontaneously magnetize such that the spins are anti-aligned, that is with saturation magnetizations $\mathrm{M}_A = -M_B$, as illustrated in Fig. 1.2. As such the ordering temperature for AFMs, T_N, now bears Néel's name. The two-sublattice model was confirmed in MnO by neutron scattering measurements taken in 1951 [12]; the results this study are now used as an example to illustrate AFM order in Kittel's textbook [11].

In contemporary times, AFM broadly underlies some of the most interesting and relevant phenomena in modern condensed matter physics research. Some of these problems were likely beyond the wildest dreams of Nèel and his contemporaries, the glaring example being high-temperature superconductivity. In both the Cuprates and Iron-based superconductors, the low temperature, low doping phase is an AFM. In the Cuprates, the AFM phase is a AFM Mott insulator which when doped with charge carriers, becomes a superconductor. A fundamental connection between the physics of doping a AFM Mott insulator and superconductivity first suggested by Andersen, stemming from his earlier prediction of a novel spin liquid (Resonating Valence Bond) state [13] in geometrically frustrated AFMs– the idea being that the hole-doping of such a state will lead to the emergence of mobile charge carriers analogous to Cooper-pairs [14, 15]. While research

on high temperature superconductors persists, the search for quantum spin liquids in real materials is now a field now all on it is own.

Quite recently, AFMs have generated significant interest in a completely different context. These days much of materials-based research is driven by potential applications in computing. In the past few years AFM thin films, as well as single crystals of $Fe_{1/3}NbS_2$ [8] have been shown to be stably switchable between resistance states upon application of electrical current pulses. Such resistive-switching AFMs are potentially applicable in magnetic memory devices offering faster switching response, lower threshold switching current, and the possibility to scale to smaller dimensions than their ferromagnetic counterparts [16].

It is in this modern context of antiferromagnetism that we return to to Nèel's cynical assertion that these materials are theoretically interesting but perhaps lacking in applications. However, we note that for a material, or an idea, to be useful, it doesn't necessary have to be applicable. The discovery of AFM has indeed proven useful: The basic physics involved is essential to our yet-developing understanding of quantum spin liquids and superconductivity– topics which have in turn taught us a great deal about fundamental nature of quantum matter. It is indeed from a landscape of such useful ideas that application-driven ideas may eventually emerge. The work presented in this dissertation tends much more toward the "useful" than the "applicable" but touches on a bit of both, and a possibly on a bit of neither.

In the following sections, we will provide some basic context for the theoretical ideas evoked throughout this dissertation.

1.1 QUANTUM MAGNETISM

The collective ordering of spins requires a quantum description. We may see this this by examining where the Weiss mean field model, which does not include any microscopic description, fails. Above the ordering temperature, both FMs and AFMs are paramagnets– here we consider specifically fixed magnetic moments on lattice cites. We can consider the action of these magnetic moments in response to an external field– in the context of the Weiss Molecular Field theory, where the mean field is given by:

$$\begin{aligned} H_{total} &= H + \boldsymbol{H}_{ex} \\ \boldsymbol{H}_{ex} &= \lambda \mu_o \boldsymbol{M} \end{aligned} \tag{1.2}$$

Where $\boldsymbol{H}$ is an applied external field and $\boldsymbol{H}_e\boldsymbol{x}$ is the "exchange field" which is arising from the ambient dipolar interactions in the material itself, proportional to the total magnetization, $\boldsymbol{M}$.

Solving his classical model, using the magnetization for a paramagnet derived from thermodynamic arguments, one can see that actually does well to describe how the moments will tend to align with the applied field H [17]. It can even predict the phase transition from paramagnetism to ferromagnetic order, and it is in this context that the Curie-Weiss law for FM is derived . However, in this solution, spontaneous magnetization will only occur provided that H_{ex} is large enough compared with k_BT. In real ferromagnetic materials, the exchange field dipolar interactions are extremely weak (order of 10^{-5} eV) compared to the observed transition temperatures [18]. There must be something else at play to generate large enough $\boldsymbol{H}_{ex}$ for FM to occur.

Spontaneous magnetization in solids is thus necessarily a collective phenomenon. It can be derived, at the base level, from the electrostatic Coulomb interaction interaction between neighboring electrons. This is where a quantum mechanical description becomes necessary: these electrons are fermions and thus they occupy states according to the Pauli exclusion principle.

1.1.1 EXCHANGE

To see how this arises, we'll consider a simple example consisting of two electrons interacting via the Coulomb potential, V_{12}.

$$\mathcal{H} = \frac{p_1^2}{2m} + \frac{p_2^2}{2m} - \left(\frac{Ze^2}{r_1}\right) - \left(\frac{Ze^2}{r_2}\right) + \left(\frac{e^2}{|\vec{r}_1 - \vec{r}_2|}\right) = \mathcal{H}_1 + \mathcal{H}_2 + V_{12} \tag{1.3}$$

Where Z is the nuclear charge. The single-particle Hamiltonians $\mathcal{H}_1$ and $\mathcal{H}_2$ can be diagonalized by single particle wavefunctions ϕ_1 and ϕ_2 – in the absence of interactions these two states may be degenerate. In a real solid, these two electrons may be in some localized state that is energetically separated from the rest of the spectrum. The V_{12} term, involving interaction between the electrons, complicates matters. The Coulomb energy C_{12} can be approximated in terms of the single-particle wavefunctions via perturbation theory, following Ref.[17]:

$$C_{12} = \int \phi_1^*(\vec{r}_1)\,\phi_2^*(\vec{r}_2)\,V_{12}\phi_1(\vec{r}_1)\,\phi_2(\vec{r}_2)\,d^3r_1 d^3r_2 \tag{1.4}$$

So the energy eigenvalues for the full Hamiltonian $\mathcal{H}$ necessarily correspond to two-electron wavefunctions ψ. Even though $\mathcal{H}$ is spin-independent, the states ψ are the product of the spatial and spin parts:

$$|\psi\rangle = |\phi\rangle^{\pm}\,|\chi\rangle^{\mp} \tag{1.5}$$

Where $|\phi\rangle$ is the spatial wavefunction $|\chi\rangle = |S, m_s\rangle$ is the spin state. The Pauli exclusion principle requires that ϕ must be antisymmetric. That is, an antisymmetric

spin state requires a symmetric spatial wavefunction and vice versa. For two electrons, there are two values the total spin can take on, $S = 0$ for $m_s = 0$, corresponding to the antisymmetric singlet state ($|\chi\rangle^-$) and $S = 1$ for $m_s = 0, \pm 1$ corresponding to the three-fold degenerate symmetric spin triplet state ($|\chi\rangle^+$). Thus there are four possible representations of ψ:

$$\begin{aligned} |\psi_s\rangle &= |\phi\rangle^+ |\chi\rangle^-;\ S = 0,\ m_s = 0 \\ |\psi_t(m_s)\rangle &= |\phi\rangle^- |\chi(m_s)\rangle^+;\ S = 1,\ m_s = -1, 0, 1 \end{aligned} \tag{1.6}$$

Where the symmetric and antisymmetric spatial wavefunctions are simply:

$$\begin{aligned} |\phi\rangle^+ &= \frac{1}{\sqrt{2}}(\phi_1(\vec{r}_1)\phi_2(\vec{r}_2) + \phi_1(\vec{r}_2)\phi_2(\vec{r}_1)) \\ |\phi\rangle^- &= \frac{1}{\sqrt{2}}(\phi_1(\vec{r}_1)\phi_2(\vec{r}_2) - \phi_1(\vec{r}_2)\phi_2(\vec{r}_1)) \end{aligned} \tag{1.7}$$

Thus, the spin state selects the symmetry of the spatial state. From this, we can already see that the Coulomb interaction lifts the degeneracy of the single particle spatial wavefunctions. As $\mathcal{H}$ does not explicitly contain spin:

$$\mathcal{H} |\phi\rangle^\pm = E_\pm \left|\phi^\pm\right\rangle \tag{1.8}$$

Effectively, the expectation value for V_{12} is different if the system is in the symmetric or antisymmetric spatial state:

$$\begin{aligned} \frac{1}{2}\int [\phi_1^*(\vec{r}_1)\phi_2^*(\vec{r}_2) \pm \phi_1^*(\vec{r}_2)\phi_2^*(\vec{r}_1)]\, V_{12}\, [\phi_1(\vec{r}_1)\phi_2(\vec{r}_2) \pm \phi_1(\vec{r}_2)\phi_2(\vec{r}_1)]\, d^3r_1 d^3r_2 \\ = C_{12} \pm J_{12} \end{aligned} \tag{1.9}$$

Where we have introduced the exchange integral, J_{12}:

$$J_{12} = \int [\phi_1^*(\vec{r}_1)\phi_2^*(\vec{r}_2) V_{12} \phi_1(\vec{r}_2)\phi_2(\vec{r}_1)]\, d^3r_1 d^3r_2 \tag{1.10}$$

One can work through the expectation values for the spin part of the total two-electron wavefunction the in terms of the spin operators $\vec{S} = \vec{S_1} + \vec{S_1}$ for both the triplet and singlet spin states (the algebra is detailed in [17]). The striking result is that for both configurations this quantity simplifies to:

$$\frac{1}{2} + 2\vec{S_1} \cdot \vec{S_2} \tag{1.11}$$

Where $\vec{S_1} \cdot \vec{S_2} = 0$ for the singlet state and $\vec{S_1} \cdot \vec{S_2} = 1$ for the triplet. As a result we can write the expectation value for V_{12}, corresponding the the energy splitting between the between the single-particle wavefunctions as:

$$E_+ - E_- = C_{12} - J_{12}(\frac{1}{2} + 2\vec{S_1} \cdot \vec{S_2}) \tag{1.12}$$

This is origin of the the well-known Heisenberg Hamiltonian, where J_{12} is the exchange coupling. Now we can see how spontaneous magnetization arises. For $J_{12} > 0$ the energy is minimized by triplet spin state; the spins will prefer to be aligned, or ferromagnetic. For $J_{12} < 0$ the spins will prefer the singlet, leading to antiferromagnetic coupling.

This can be generalized to systems with many atoms and many electrons, where the exchange interactions between nearest neighbor spin is written given by the Heisenberg Model:

$$H = -\sum_{\langle i,j \rangle} J_{ij} \vec{S_i} \cdot \vec{S_j} \tag{1.13}$$

Solving this model, in various configurations and iterations, has at this point, occupied physicists for nearly one hundred years.

For our purposes It may be useful to consider a description of physical origin of the coupling J_{ij} offered by Ref. [18]. In FM materials, the spatial wavefunctions of the two localized electrons are antisymmetric, or orthogonal, so they overlap significantly in space and the Coulomb repulsion between sites is large. The electron spins will tend to align to minimize the effects of Coulomb repulsion; the preferred energy state is the triplet. This is familiar for those acquainted with Hund's rules for filling atomic orbitals, where electrons occupy orbital states in a way that maximizes their total spin. The spins interact via direct exchange coupling J_{ij}.

For AFM, in real materials, the picture is a little more complicated– orbital wavefunctions are spatially separated and are not orthogonal; that is the separation between nuclei is large such that there is not much overlap between atomic orbitals. The interactions between the spins in this case depend will depend on competition between Coulomb repulsion and the tendency for spins to hop between sites. This is easiest to see by considering a more general Hamiltonian:

$$H = -t \sum_{i,s} \left(c^\dagger_{i,s} c_{i+1,s} + c^\dagger_{i+1,s} c_{i,\sigma} \right) + U \sum_i n_{i\uparrow} n_{i\downarrow} \tag{1.14}$$

This is the of course the Hubbard model [19]. The first term is derived from tight-binding, and represents nearest-neighbor inter-site hopping where $c^\dagger_{i,s}$ and $c_{i,s}$ are the second-quantized creation and annihilation operators for a particle of spin s on site i.

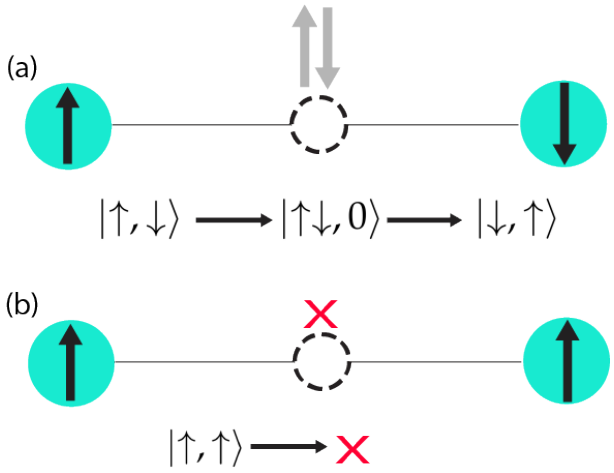

Figure 1.3: Superexchange between two magnetic ions (cyan) mediated by a non-magnetic ion (dashed) (a) Anti-aligned spins may virtually hop between sites via an exchange pathway that includes double occupation of electrons. (b) For aligned spins, double occupation is forbidden by Pauli exclusion

The second term represents the on-site interaction, where $n_{i,s}$ is the spin density operator. This is effectively the energy cost of putting two electrons on the same site.

When the U is large compared to t, we can treat the hopping term as perturbation and expand the Hamiltonian in second-order perturbation theory. The result is an effective Hamiltonian with eigenstates that are doubly occupied by electrons– that is, the neighboring orbitals hybridize, allowing for virtual hopping of spins from site to site. However, if the two spins are in a triplet state, virtual double-occupation is prohibited by Pauli exclusion. Thus the energetically preferred spin state is the antisymmetric singlet which minimizes the kinetic energy associated with hopping. The spins want to be anti-aligned.

As it happens, the operators which connect the double-occupation states ("exchange pathways") may be written in terms of the spin-1/2 operators, S, and we retrieve an effective Hamiltonian of Heisenberg form, with exchange $J \propto -t^2/U$. This calculation is reviewed in Ref. [18].

In magnetic insulators, i.e. compounds containing elements with partially filled $3d$, $4f$, and $5d$ electron shells, including α-$RuCl_3$, this process of virtual hopping is called "superexchange" [20]. The in-direct exchange interaction between two magnetic ions is mediated by a non-magnetic ion, as illustrated in Fig. 1.3. Such compounds are often Mott insulators [21], that is, they are predicted to conduct based on pure band structure, but a large U relative to t leads to the localization of electrons and hence a so-called correlated insulating state.

We have seen how Heisenberg exchange is quite generally applicable. There is a reduction of Heisenberg which is also a powerful tool in the description of magnetism in materials: the Ising model. In this Ising model, the magnetization is confined to lie along a specific "easy" axis, so we may consider interactions between only one component of the spins (this case S_z) and the coupling can be represented as a simple scalar.

$$H = J \sum_{\langle i,j \rangle} S_{z,i} S_{z,j} \tag{1.15}$$

The Ising model is one of the well-known problems in condensed matter physics– it famously does not order in one dimension (and in zero applied field) but in two dimensions or more undergoes a phase transition [22]. It is interesting to note that historically, the Ising model was developed before Heisenberg, both in the 1920s.

There is a useful point about symmetry to be made about these two models. The nearest neighbor Heisenberg model discussed above has a continuous rotational symmetry– the interaction contains the full spin operators and the resulting ground state is invariant under continuous global rotations. The spins can point where they may.

In the Ising model, the interaction is a scalar– spins may either be up or down, +1 or -1. The ground state is invariant under a global spin flip, rather than a rotation, and thus we say the Ising model has a discrete Z_2 symmetry.

As we will see throughout this dissertation, the Ising model is applicable in describing real and even complex magnetic phenomena.

1.1.2 FRUSTRATION

It's remarkable how the seemingly simple Hamiltonians we have discussed thus far can, in various extensions and configurations, describe a large range of magnetic materials and to interesting physics. We have shown above that these interactions arise from a fundamentally quantum description. However the ordered states that result from the simple case of nearest-neighbor Heisenberg coupling may treated semi-classically, as we saw for example by the successful application of the Weiss mean field theory to describe the FM ground state. But of course, there are more things in Heaven and Earth.

This leads us to frustration. Frustration occurs in magnetic systems when there is no configuration of spins which can simultaneously satisfied all of the interactions. This can result from special cases of lattice geometry. The classic example of geometric frustration is a configuration of AFM Ising spins arranged on an equilateral triangular lattice, illustrated in Fig. 1.4.

Where we can imagine if we fix the AFM Ising interaction to be satisfied for the lower two spins, then the top spin would equally feel the exchange from the of the two lower

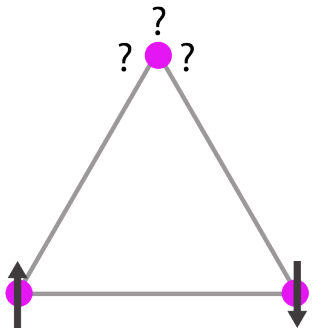

Figure 1.4: Cartoon of AFM Ising model on the triangular lattice with frustrated spins.

spins and thus have no preferred orientation. The ground state is degenerate [23] as there six possible arrangements of spins corresponding to combinations of one up, two down and etc. As a result in the ground state at finite temperature the collective spins (thermally) fluctuate between these six configurations, giving rise to a correlated liquid-like state.

Frustration may also arise from the complication of interactions as opposed to from pure geometry. First off in real materials there are often couplings beyond the first-nearest neighbor interactions we have considered thus far. Furthermore interactions can be anisotropic – for example antisymmetric exchange may arise when spin-orbit coupling is taken into account [24, 25]. As we will see later on, anisotropy may also arise from a combination of complicated interactions and special crystal geometries [4, 26].

In frustrated spin-1/2 systems, quantum fluctuations are on the order of the spin size, and thus spins may fluctuate even down to zero temperature. The resulting ground state is a superposition of many spin configurations, and cannot be written as a quantum mechanical product state [27]. The result is a quantum spin liquid, which we mentioned briefly earlier in the context of High-temperature superconductivity.

So broadly, frustration underlies some of the most interesting phenomena in quantum materials. The quantum spin liquid in particular will be discussed further in Chapter 2.

1.2 ORGANIZATION OF THIS DISSERTATION

This dissertation consists of two major projects, pertaining to two different AFM materials. The first project involves the study of low-energy excitations in the quantum spin liquid

candidate material, α-$RuCl_3$, by terahertz (THz) spectroscopy measurements. The second project centers on the magnetic properties of intercalated transition metal compounds. We began this particular project in hopes of discovering exotic magnetic excitations. What we found was something quite different– a simultaneous nematic-magnetic transition in the compound $Fe_{1/3}NbS_2$, which around the same time was reported to show resistive-switching behavior.

Part 1 contains Chapters 2 through 4 and is devoted to the α-$RuCl_3$ project. Chapter 2 contains an overview of the the search for quantum spin liquids and our motivation to explore magnon excitations in α-$RuCl_3$. Chapter 3 consists of a practical introduction to our technique, as well as detailed descriptions the two THz spectroscopy systems that were constructed in our lab and used to carry out this work. Our results and theoretical interpretation are presented in Chapter 4. The work presented in these chapters ins published in references [28] and [29].

Part 2 contains Chapter 5 through 7 and is devoted to $Fe_{1/3}NbS_2$. Chapter 5 provides an introduction to intercalated transition metal dichalchogenides as well as a primer on the theoretical concepts which will be used to describe the data in the subsequent chapters. Chapter 6 describes the scanning photo-thermal birefringence microscopy technique that we developed and implemented to study this material. Finally, Chapter 7 presents our data on $Fe_{1/3}NbS_2$ and accompanying theoretical analysis, which we hope may provide insight into resistive switching behavior and nematicity in a broader class of materials with 6-fold symmetry. The work presented in these chapters is published in reference [30].

At first glance, these two projects may seem unrelated. In some respects, they are. But upon closer inspection there are indeed broad themes which unite this dissertation as a body of work. Evidently, both materials studied are AFMs which order (in zero applied field) at some finite temperature. In both cases, we make use of the polarization of light to tease out the lowered symmetries of the ordered phase– demonstrating the power of optical polarimetry as a probe of broken symmetry. Finally, while the motivation for each project is very different, as we will see, throughout the following chapters, the interesting physics in both cases arises from frustrated magnetism.

PART I

TERAHERTZ SPECTROSCOPY OF A QUANTUM SPIN LIQUID CANDIDATE

2

THE QUANTUM SPIN LIQUID, THEORY AND REAL MATERIALS

When exchange interactions between neighboring spins in a magnetic system are at odds, the resulting frustration can lead to a highly entangled form of matter with no ordered ground state. Such highly correlated, liquid-like states have come to be known as quantum spin liquids (QSLs). QSLs are commonly defined by what they lack: spontaneous symmetry breaking or of long-range magnetic order. However, QSLs may also be defined by what they entail: a highly entangled ground state which cannot be written as a quantum mechanical product state, with excitations which take the form of quasiparticles with fractional statistics [27, 31, 32].

The QSL is a broad topic in condensed matter physics. Historically, the concept was originally initiated by Andersen in the 1970s, in the context of the resonating valence bond state, where neighboring spin-1/2 moments on a triangular lattice become entangled singlet pairs, giving rise to an insulating, fluctuating ground state as opposed to AFM Néel order [13]. These ideas were later applied to suggest that high-temperature superconductivity in particular in the case of the La-cuprates, may arise from such a QSL state when system is sufficiently charge doped [14].

The QSL state is markedly featureless and difficult to experimentally detect – there being no local order parameter or phase transition. Lattices exhibiting geometric frustration, specifically those based on triangular arrangements of spins such as the Kagome lattice[33], have long been at the center of QSL research. Spin liquid states which emerge from strong geometrical frustration or from complicated long-range interactions are suffer both from theoretical challenges (not exactly solved) and experimental challenges (not realized in physical materials) [34].

A full description of the detailed physics of QSL is beyond the scope of the this thesis, however an extensive review article on the topic may be found in Ref. [31].

2.1 KITAEV HONEYCOMB

A significant step in the development of QSL theory was an alternative, exactly solvable model proposed by Alexey Kitaev [35, 36] in 2003. This model, dubbed the Kitaev spin

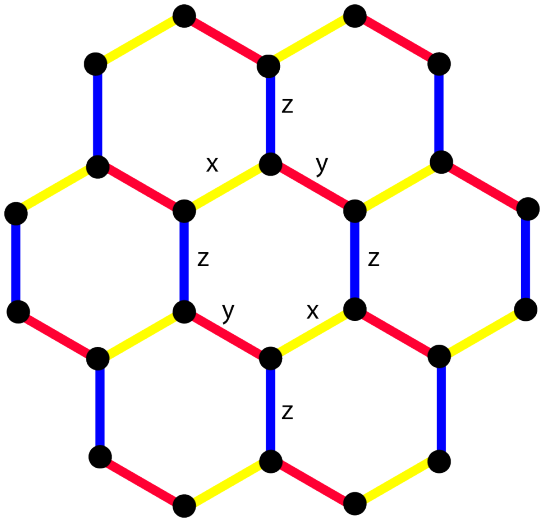

Figure 2.1: Illustration of the Kitaev Honeycomb Model. Each vertex of the honeycomb lattice (black circles) has a spin-1/2 particle with bond-dependent Ising interactions between nearest neighbors. The three types of bonds are labeled to denote which x (yellow), y (red) and z (blue).

liquid (KSL) model, has been the subject of intense interest for the past decade as it is both analytically solvable and potentially realizable in real materials. The model consists of spin-1/2 particles arranged on a two-dimensional hexagonal lattice with a bond-dependent Ising exchange interaction between nearest neighbors. That is,

$$H = -J_x \sum_{\text{x links}} \sigma_j^x \sigma_k^x - J_y \sum_{\text{y links}} \sigma_j^y \sigma_k^y - J_z \sum_{\text{z links}} \sigma_j^z \sigma_k^z \tag{2.1}$$

This Hamiltonian is often written in the abbreviated notation:

$$H = K \sum_{\langle i,j \rangle} S_i^\gamma S_j^\gamma \tag{2.2}$$

Where K the Kitaev exchange coefficient the three bond types are represented by $\gamma = \{\text{x, y, z}\}$. Frustration results from rotation of the Ising axis from bond to bond, rather than the geometry of the lattice. In the exact solution of the KSL model, the spin Hamiltonian is recast in terms of Majorana fermions propagating on the landscape of a static Z_2 gauge field. The exact solution is discussed in mathematical detail in Kitaev's original paper as well as lecture notes presented in Ref. [37] and the thorough review article [31]. Z_2 fluxes are localized and gapped, while the Majorana particles are itinerant and gapless at zero field. It is interesting to note that while the Majorana concept arises from a solution to a modified Dirac equation found in the 1930s, such particles have yet

to be discovered in particle physics; the emergent excitations from the KSL ground state emulate theoretically predicted particles not yet discovered in vacuum.

These excitations have non-local properties– or "mutual statistics" by which they may acquire a Berry phase as they are braided around each other. These unique properties have led to the advancement of topological quantum computing schemes, which are described at length in References [31, 37].

2.2 KITAEV PHYSICS IN REAL MATERIALS

In addition to having an exact solution, the Kitaev honeycomb model has been so widely studied because such bond-anisotropic interactions can be realized in physical materials. The manifestation of Kitaev exchange in real materials was first proposed by Jackeli and Khaliullin [4] in 2009.

These authors considered heavy $4d$ or $5d$ transition metal (TM) Oxide compounds, with strong spin-orbit coupling, where TM ions with partially-filled d-electron levels are arranged on a honeycomb lattice. Each magnetic ion is surrounded by an octahedra of ligand ions (Oxygen, or in the case of α-$RuCl_3$ Chlorine). To reproduce the Kitaev model in such compounds an effective spin-1/2 moment must exist on each TM site. A schematic illustrating how such a condition arises, using the electronic structure of α-$RuCl_3$ as an example, is showing in 2.2 (a). First, the octahedral crystal field splitting separates the degenerate d orbitals into an e_g doublet and a t_{2g} triplet. Spin-orbit coupling (SOC) further separates the t_{2g} state into levels with pseudo-spin $J_{eff} = 3/2$ and $J_{eff} = 1/2$. The resulting J_{eff}=1/2 momenta correspond to Kramer's doublet states which are spin-orbit mixed and thus have anisotropic spin density in real space. The on-site Hubbard interaction further splits the $J_{eff} = 1/2$ band giving rise a Mott-insulating state with a single hole with an effective spin-1/2 moment on each TM site [4].

The resulting magnetic Hamiltonian sensitively depends on the geometry of the TM-ligand octahedra structure in the crystal lattice. Jackeli and Khaliullin considered two possibilities (1) corner-shared octahedra and (2) edge shared octahedra, where the TM-ligand-TM bond angles are precisely 90 degrees, as show in 2.2 (b). In the edge-shared configuration, the hopping amplitude has contributions both from the overlap of the TM d-orbitals themselves, and from two superexchange pathways mediated from the TM d-orbitals through p-orbitals of the upper and lower ligand atom. The opposite superexchange pathways destructively interfere in such a way that the isotropic part of the Hamiltonian cancels.

The remaining d-d orbital exchange interactions depend on which octahedral edge is shared and thus exhibit the bond-directionality familiar to the Kitaev honeycomb, $S_i^\gamma S_j^\gamma$. Additional interactions are symmetry-allowed, in particular direct exchange coupling from

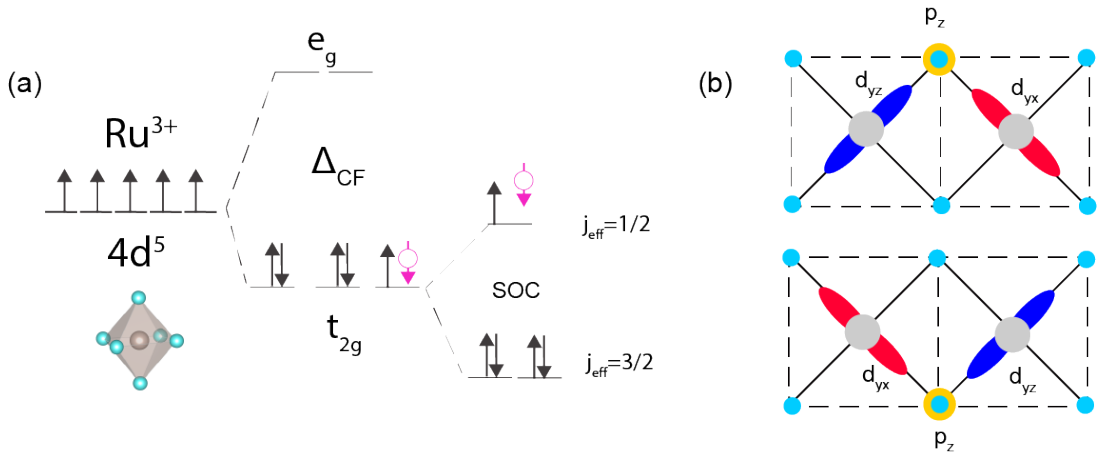

Figure 2.2: (a) Level diagram showing the electronic configuration for a spin-1/2 Mott insulator in α-$RuCl_3$. Black arrows represent electron-occupied spin states, pink arrows represent holes. SOC in α-$RuCl_3$ is ~ 0.15 eV [2]) (Figure adapted from [3]) (b) Cartoon showing the superexchange pathways for idealized 90-degree edge-shared octahedra. Grey circles represent TM ions, while blue circles represent ligand atoms. Top row illustrates the upper superexchange pathway between the TM sites from the blue d_{yz} orbital, mediated through the yellow p_z ligand orbital, to the red d_{yx} orbital. Bottom row represents the lower superexchange pathway. (Figure adapted from [4])

the overlap of d-orbitals even in a idealized crystal gives rise to a complex phase diagram of magnetically ordered states [3, 38]. A more relevant generalized Hamiltonian, then is the a K-H-Γ Model:

$$H = K \sum_{\langle i,j \rangle} S_i^{\gamma} S_j^{\gamma} + \Gamma (S_i^{\alpha_{ij}} S_j^{\beta_{ij}} + S_i^{\beta_{ij}} S_j^{\alpha_{ij}}) + H \tag{2.3}$$

Where H represents Heisenberg exchange of various degrees and Γ represents symmetric coupling of off-diagonal spin components. We will revisit this Hamiltonian in Chapter 4. Of course, non-ideal crystals, where bond angles may not be exactly 90 degrees and etc., may host additional interactions which may bring the farther away from the perfect Kitaev model.

In the years following this seminal theoretical work, there was an explosion on both the experimental and theoretical fronts focused on finding a KSL material, the leading candidates being the various polytypes of Li_2IrO_3 and Na_2IrO_3 [39–42] as well as α-$RuCl_3$ [2, 43]. However, all of these materials order magnetically at low temperatures [40, 42, 44–47] indicating that they are not KSLs (in zero applied field) and that designing a material which emulates the Kitaev model is particularly challenging [34, 48, 49].

Despite the onset of magnetic order at low temperatures in these real materials, it has been suggested quantum-disordered state or even spin-liquid state may be achieved by applying external perturbations such as fields or chemical substitution [50]. Characterizing the nature of the magnetic interactions can help to navigate the rich phase diagrams of these Kitaev materials.

2.3 α-RUCL$_3$: CRYSTAL STRUCTURE AND MAGNETIC GROUND STATE

In α-$RuCl_3$, Ru^{3+} ions in a $4d^5$ configuration are surrounded by edge-shared Cl_6 octahedra and arranged on a honeycomb lattice. Quasi-2D layers are stacked and van der Waals coupled to form bulk α-$RuCl_3$. This material has been studied since the 1960s, and was original thought to be magnetic semiconductor [51]. In light of the development of the KSL model in recent years, this compound has been revisited as a possible KSL candidate. Original it was thought that the heavy Ru^{3+} would not generate strong enough Coulomb repulsion to achieve at Mott insulator [34]. The tides changed when study combining X-ray absorption, optical spectroscopy, and electronic structure calculations which included Spin-Orbit coupling showed that this compound is indeed Mott insulating [43]. Plumb et al. measured optical absorption well below the 1 eV (e_g to t_{2g}) gap [43]– in particular absorption at $\approx$ 200 meV, corresponding to transitions between the split $j_{eff} = 1/2$ and $j_{eff} = 3/2$ (see Fig. 2.2). This characterizes α-$RuCl_3$ as spin-orbit assisted Mott insulator with a $j_{eff} = 1/2$ hole on each site and a promising KSL candidate.

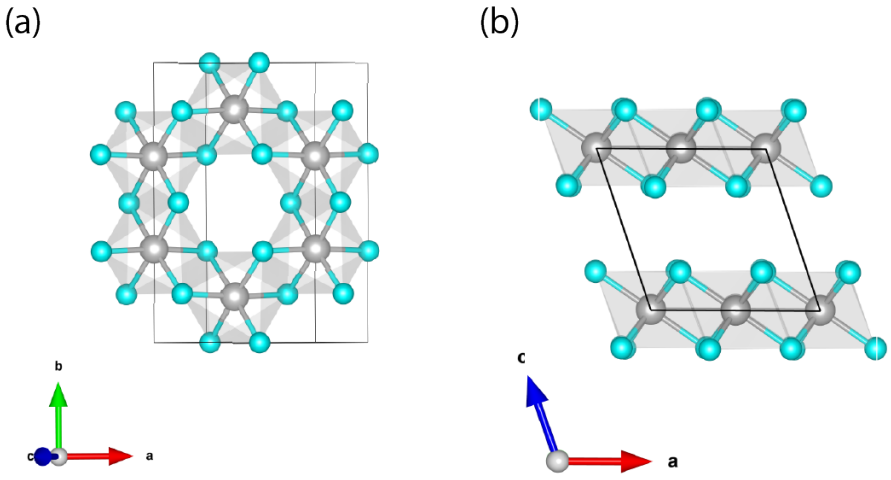

Figure 2.3: Crystal structure of α-$RuCl_3$ showing the monoclinic (C/2m) unit cell (black outline). Ru ions are depicted as grey balls, Cl as turquoise. (a) Projection on the ab plane, showing honeycomb arrangement of Ru ions and edge-sharing Cl octahedra. (b) Projection on the ac plane, showing A-B stacking.

In the past five years, research on α-$RuCl_3$ in the context of Kitaev accelerated, in part because of the availability of large single crystals suitable for inelastic neutron scattering (INS) [7, 52, 53] and optical spectroscopy. In contrast, other popular Kitaev materials such as the Na- and Li- Irridates often form small (less than 1 mm) crystals which make these types of experiments difficult or impossible.

Understanding the crystal structure of this compound has proven challenging, even controversial, as the particular space group of the crystal depends on the stacking arrangement of the $RuCl_3$ layers. The weak bonding of the $RuCl_3$ layers gives rise to stacking faults– anomalies in the layer stacking periodicity– which manifest as diffuse scattering in diffraction experiments and can complicate the interpretation of the data [54]. Many contemporary studies have cited an earlier work, [55], which reported ABC stacking periodicity and the corresponding trigonal $P3_112$ space group. In 2015, Johnson et al. [54] reported that the room temperature crystal structure is in fact monoclinic, with space group $C2/m$ as shown in Fig. 2(a), and single-layer stacking periodicity (ABA) with a shift of $-\mathbf{a}/3$ per layer as shown in Ref. 2.4. These authors also note that monoclinic structure breaks the three-fold rotational symmetry of the perfect honeycomb lattice. There is an in-plane distortion of the Ru-hexagons in which the length of a pair of opposing Ru-Ru bonds parallel to either the a or b axis is longer than the other two by about 0.2% There are three degenerate orientations of this distortion, and crystals may form either as largely single-domain or containing multiple structural domains [54].

Perhaps such sample-to-sample variations are at fault for the difficulty in resolving the crystal structure of this compound. After the revision of the crystal structure to monoclinic, Cao et al. [56] showed that some large crystals are in fact trigonal at room temperature and undergo a structural phase transition from the trigonal structure to the monoclinic structure at around 150 K. Smaller crystals on the other hand are found to be monoclinic at all temperatures. Structural phase transitions in this compound have been reported by several other groups [57, 58], including an x-ray diffraction measurement by Park et al [59] which reported a transition to a rhombohedral ($R\bar{3}$) structure at around 60 K. What's more, the prevalence of stacking faults means that some crystals may contain a large fraction of ABCABC layer stacking in addition to ABA stacking [60]. A detailed summary of what is known about the structure of α-$RuCl_3$ can be found in Ref. [60].

As discussed in Chapter 4, the crystals studied by our optical techniques display broken C_3 symmetry at both high and low temperature. In light of this, for the remainder of this thesis, we will use the $C2/m$ space group to describe the crystal structure of α-$RuCl_3$.

As mentioned previously, α-$RuCl_3$ orders at low temperature. Unsurprisingly, the stacking faults may also play a role in the magnetic properties of this material. Detailed magnetic susceptibility data in Ref. [47] shows a broad peak in the in-plane susceptibility, χ_{ab} at around 14 K, followed sharp drop at 7 K. It is now understood that the transition to Nèel order occurs at 7 K while the higher temperature feature in the data is related to distortions in the crystal and stacking faults. [52, 56, 61]. A large susceptibility anisotropy (χ_{ab} is greater than χ_c by about a factor of 10), reflecting the weak coupling of the van der Waals layers and indicating the moments lie mostly in the honeycomb plane [47].

The form of the zigzag ground state informs further constraints to the possible form of the magnetic Hamiltonian. Ab-initio [50, 62] and exact diagonalization calculations indicate that extra interaction terms beyond the K-H model (Eq. 2.3) in particular third nearest neighbor coupling, J_3, and symmetric off-diagonal coupling Γ_1 are necessary in describing magnetic properties α-$RuCl_3$. Note that these additional interactions are crucial to our linear spin wave theory description of TDTS spectra as detailed in Chapter 4.

Soon after these initial measurements, it was discovered that for in-plane magnetic fields in the range 7 - 8 T, the magnetic order in α-$RuCl_3$ disappears– suggestive of a quantum phase transition to a disordered phase [57, 61, 63, 64]. The nature of this phase and its proximity to the KSL is still of great interest to the research community. As such the phase diagram of α-$RuCl_3$ in magnetic field (Fig. 2.4) has since been studied extensively by a wide range of experimental probes, which we discuss in the following section.

2.4 EXPERIMENTAL SIGNATURES OF A QSL

If in theory the transition to a QSL state occurs in the absence of symmetry breaking, how do we experimentally detect a such state in α-$RuCl_3$? Here, we briefly summarize a few of the techniques applied to study magnetism in α-$RuCl_3$ what the signatures of a QSL may look like in these probes, and what we can learn from TDTS measurements on this system.

2.4.1 MAGNON EXCITATIONS

One approach to the hunt for a QSL state is to study the potential signatures of fractionalized excitations in the magnetic excitation spectra. In α-$RuCl_3$, detection of the predicted Majorana quasiparticles and Z_2 fluxes would indeed be a hallmark of the Kitaev phase.

To search for these exotic modes, however, we must first understand the magnetic excitations we expect from the ordered ground state. The simplest low-energy spin excitation one could imagine, for example, about the Heisenberg ferromagnetic ground state, is the flip of a single spin. In practice, it is energetically preferable for that spin-flip to be effectively "shared" across all the spins. The result is that the lowest-energy ordered excitations about the magnetic ground state consist of the collective oscillations of the ordered spins, magnetic resonance or "spinwaves". The quantization of these oscillations may be treated as quasiparticles with spin-1 Bosonic statistics, called magnons [18, 22].

The creation of a single quasiparticles at a fixed energies and wavevectors, or a "single magnon modes" are the exact eigenstates of the Heisenberg Hamiltonian, and thus spectroscopically correspond to sharp resonances at well-defined energy and momenta. Single-magnon modes can thus generally be written in the terms of quasiparticle creation operator S_k acting on a magnon vacuum to generate a state at momentum $\boldsymbol{k}$:

$$|\mathbf{k}\rangle = S_k |0\rangle \tag{2.4}$$

Multi-magnon states may also be generated, where an excitation deposits momenta but creates multiple magnons which share the momenta imparted by the excitation. These are not exact eigenstates but instead can arise when magnons are allowed to interact. We can write these states as [22]:

$$|multi - k\rangle \approx \prod_{k}^{n_k} S_k^n |0\rangle \tag{2.5}$$

Where n_k is the number of modes created with momentum k. It is important to note that even though multi-magnon excitations may be detected by the scattering and op-

tical probes at fixed momenta, the measured energy of these states depends on the full dispersion. This comes into play in our measurements in Chapter 4.

2.4.2 NEUTRON SCATTERING

Neutron scattering is the classic probe of magnetic order and excitations. Neutrons have both spin and magnetic moment, and as such a beam of neutrons will interact with both the atomic nuclei in the lattice and the magnetic moment of the electron spin via the magnetic dipole interaction.

In neutron scatting, quasi-elastic scattering provides a direct measure of the static spin-spin correlation functions, $S_{\alpha\beta}(\boldsymbol{Q})$. Long-range order appears as Bragg diffraction peaks, from which the form of the ordered magnetic ground state can be extracted. Inelastic neutron scattering measurements (INS), on the other hand, access the dynamic spin correlation functions, and thus provide spectroscopic information about spin excitations. [65]

The inelastic part of the neutron cross-section is related to the dynamic spin-spin correlation function, $S_{\alpha\beta}(\boldsymbol{Q},\omega)$, which measures the time-dependent correlation functions of both the atomic positions and the density of magnetic moments in response to a scattered neutron. Thus neutrons may excite both elastic modes (phonons) and magnons. The two may be separated by considerations of energy and angular momentum conservation in the scattering process. In particular we are interested in the interaction of the neutron magnetic moment with the spin moment of an electron in the lattice, where a neutron may excite a magnon by creating spin flip, a process which must conserve angular momentum. With the right combination of experiment geometry and data analysis (we will leave this up to the neutron experts), one can extract the part of the dynamic correlation function $S_{\alpha\beta}(\boldsymbol{Q},\omega)$ related to spin excitations, which gives the spectrum of single-magnon excited states. [65, 66]. In neutron scattering we expect magnons, the characteristic excitations of the ordered phase, to appear as well defined energy bands in $S_{\alpha\beta}(\boldsymbol{Q},\omega)$

In typical magnetic materials magnon excitations correspond to energies of order of a few meV – Neutrons have energies around 5 meV and de Broglie wavelengths around 4 The expected dispersion relation at for magnons low-Q in the both the FM (quadratic) and AFM (linear) Heisenberg Hamiltonian (Chapter 1) is worked out in detail in Refs. [17], [11], [22], [18] and many other texts.

2.4.2.1 NEUTRON SCATTERING ON α-$RUCL_3$

Neutron diffraction measurements on α-$RuCl_3$ show that the magnetic ground state below 7 K and in zero applied magnetic field is a zigzag AFM [52, 54, 56]. The zigzag state con-

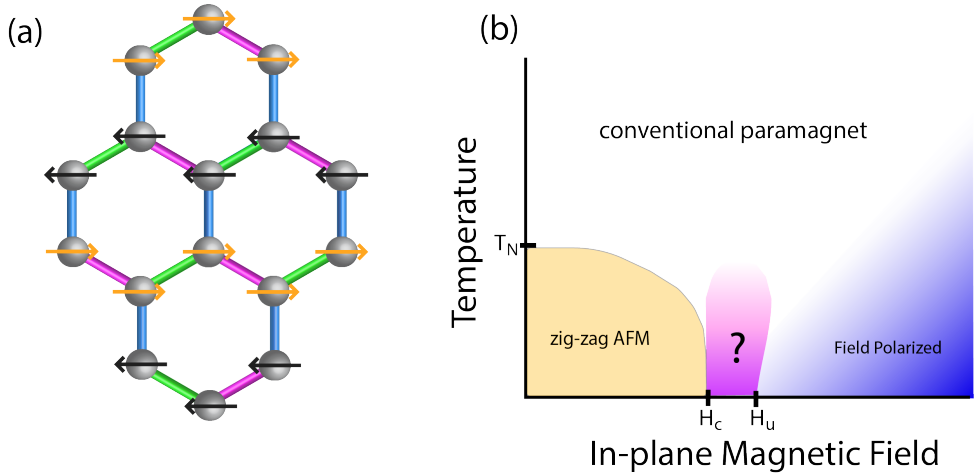

Figure 2.4: (a) Illustration of the zig-zag magnetic order in α-$RuCl_3$, consisting of two ferromagnetic chains of spins along the edges of the honeycomb lattice (gold arrows and black arrows) which are antiferromagnetically coupled to one another. (b) Schematic of the magnetic phase diagram of α-$RuCl_3$ based on a summary of data presented in Ref. [5]. T_N denotes the Neel temperature of 7 K. H_c denotes the phase transition to a disordered state (purple shaded region) at around 7.5 T, and H_u denotes a proposed topological phase transition from the disordered state to the partially field-polarized region. [6]

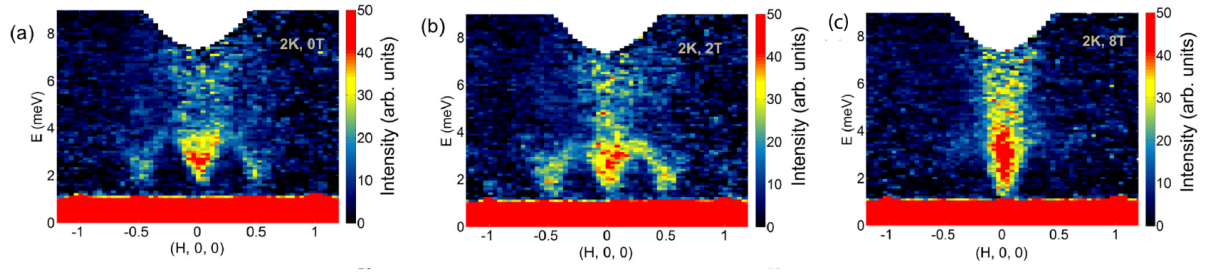

Figure 2.5: Inelastic neutron scattering data at three different applied fields, showing scattering intensity related to magnons at the M-points (0.5,0,0) and (-0.5,0,0) and a continuum of scattering at Γ for three fields (a) H=0 T (b) H= 2 T (c) H= 8 T, where above the critical field, the intensity related to magnons at the M-point has vanished. Figure originally appeared in Ref. [7] in NPJ Quantum Materials, 2018. Reprinted under the Created Commons Attribution 4.0 International license at http://creativecommons.org/licenses/by/4.0/. Modified to include only panels (a), (b), and (f) of the original figure.

sists of ferromagnetic chains of spins which are ferromagnetically coupled to one another, as illustrated in Fig. 2.4. While the zigzag state is robust to out-of-plane magnetic fields up to 14 T, it was discovered that magnetic order disappears in a relatively low in-plane critical magnetic field of around $H_c \sim 7.5$ T [7, 54, 57, 61, 64, 67, 68].

Interest in the nature of the disordered phase both above the Néel temperature and at zero field and a low temperature for fields $H > H_c$ was piqued by inelastic neutron scattering (INS) measurements reported by Banerjee et al. in Ref. [52]. The INS results on α-$RuCl_3$ at zero field in [52] and also in [7] showed both sharp peaks consistent with magnon excitations, characteristic of the zigzag ordered phase, together with an unusual continuum of scattering centered at $\mathbf{Q} = 0$ (Γ-point). The INS data from Ref. [7] is reproduced in Fig. 2.5 to illustrate this behavior. As the sample was warmed above T_N, it was found that while the sharp resonances associated with magnons disappeared with the loss of long-range order, the continuum feature persisted. This continuum was seen as well by Raman spectroscopy. [69].

The reason result was so intriguing is because the excitations with fractional quantum numbers, which solve the Kitaev model, in principle would in principle give rise to a broad continuum feature. As opposed to the bosonic magnon excitations in the ordered phase, these fractional excitations are non-local (or "deconfined"), which means that single spin operators acting on the ground state may only create them in pairs. Spectroscopically this manifests as a continuum of scattering where at each momentum transfer $\boldsymbol{k}$, the intensity is distributed over a range of frequencies, only constrained by conservation of momentum [31]. Exact analytical results for dynamical spin correlations can be derived [70], leading

to predictions for the such signatures of Majorana quasiparticles in INS [71–73], Raman [74], and resonant X-ray [75] scattering. Hence the continuum feature observed in INS was interpreted as a possible signature of Majorana fermions and Z_2 vortices in the KSL state. It is a somewhat unfortunate trick of nature that the defining spectroscopic feature of the phase we are searching for is, by definition, featureless.

It was furthermore found that this continuum persisted in the disordered phase, at fields above H_c [7], this data is reproduced in Fig. 2.5. This begs the question of if a phase KSL exist when magnetic order is suppressed by in-plane fields. If so, magnetic field may be used as a tuning knob for parameters related to the KSL phase.

2.4.3 MOTIVATION FOR OPTICAL MEASUREMENTS

Like neutrons, photons couple to spin excitations through the magnetic dipole interaction. In principle THz spectroscopy measurements are sensitive to the same excitations accessible in INS, the key difference being that one-photon processes can couple only to $\boldsymbol{Q} = 0$ excitations.

Do we expect to see magnon absorption at $\boldsymbol{Q} = 0$? THz photons are in the correct energy range (1 THz = 4.16 meV) we expect to probe spin excitations– that is, if the magnon states are gapped $\boldsymbol{Q} = 0$. If we consider just the FM Heisenberg model, by Goldstone's theorem, the spontaneous breaking of the continuous rotational symmetry of the ordered ground state (with wavevector $\boldsymbol{q}$) implies that the lowest energy mode will approach zero energy as $\boldsymbol{Q} \to \boldsymbol{q}$ [18]. In for the simple FM, $\boldsymbol{q} = 0$ and thus the magnon states are zero-energy (Goldstone) modes at $\boldsymbol{Q} = 0$ and will not absorb a photon.

In α-$RuCl_3$, the zigzag AFM ground state has a nonzero wavevector, along the $\Gamma - M$ direction of the hexagonal Brillouin zone $\boldsymbol{q} = (1/2, 0, 0)$. What's more, continuous rotational symmetry in α-$RuCl_3$ is already broken by the presence of spin-orbit coupling. $\boldsymbol{Q}$=0 magnons are gapped and in turn may be accessed by optical excitation, this can actually be seen directly in the INS spectra in Ref [7], and reproduced in Fig. 2.5. In fact even the M-point magnons are gapped. As we will see in Chapter 4, the Hamiltonian for α-$RuCl_3$ of contains several additional interactions which further lower the symmetry.

So, we can excite magnon excitations in α-$RuCl_3$ with light. It's quite fortunate then that in α-$RuCl_3$ the broad continuum of interest in the INS data discussed above also occurs at the Γ - point, and signatures of fractionalization may also be accessible by THz absorption. As such would like to be able to compare THz absorption spectra to the neutron measurements. In fact, there is a simple relation between the THz absorption and the two-spin correlation function probed by INS– this is a general result for all systems in the linear response regime. In linear response theory, the response of a system to a time-dependent perturbing field is quantified by a complex response function

$\chi = \chi'(\omega) + \chi''(\omega)$. By the fluctuation dissipation theorem, there must be a frequency-dependent correlation function which is proportional to the imaginary (dissipative) part of the response function. [65, 66]

$$\frac{1}{2\pi\hbar} S_{\alpha\beta}(\boldsymbol{Q},\omega) = \frac{1}{\pi}\frac{1}{1-e^{-\beta\hbar\omega}}\chi''_{\alpha\beta}(\boldsymbol{Q},\omega) \tag{2.6}$$

In general THz photons may be absorbed via magnetic dipole or electric dipole interactions. In the case of absorption of light by magnetic dipole absorption, the relevant response function is the complex magnetic susceptibility, $\chi(\omega)$. We can see this in a straightforward way by considering that the propagation of THz through media is described by Maxwell's equations in matter, together with the standard constitutive relations,

$$\begin{aligned} \boldsymbol{D}(\omega) &= \epsilon(\omega)\boldsymbol{E}(\omega) \\ \boldsymbol{B}(\omega) &= \mu(\omega)\boldsymbol{H}(\omega) \end{aligned} \tag{2.7}$$

Where $\epsilon(\omega)$ is the dielectric function and $\mu(\omega)$ is the magnetic permeability, related to the magnetic susceptibility, $\chi(\omega)$ by $\mu(\omega) = \mu_0[1+\chi(\omega)]$. Together these relations yield,

$$\tilde{n}(\omega) = \sqrt{\frac{\epsilon(\omega)\mu(\omega)}{\epsilon_0\mu_0}}. \tag{2.8}$$

In the THz region of the α-$RuCl_3$ spectrum, we have the strong inequalities, $\mu_2/\mu_0, \epsilon_2/\epsilon_0 \ll \epsilon_1/\epsilon_0$, where the subscripts 1, and 2 denote real and imaginary parts, respectively. To a very good approximation, we can express the imaginary part of the index of refraction, $\kappa(\omega)$, as the sum of contributions from the dielectric and magnetic response functions,

$$\kappa(\omega) \cong \frac{n}{2}\left(\frac{\epsilon_2(\omega)}{\epsilon_1} + \chi''(\omega)\right). \tag{2.9}$$

The absorption coefficient, $\alpha(\omega) = \omega\kappa(\omega)/c$, can then be written

$$\alpha(\omega) \cong \frac{n\omega\chi''(\omega)}{2c} + \frac{\sigma_1(\omega)Z_0}{2n}, \tag{2.10}$$

where the real part of the optical conductivity $\sigma_1(\omega) = \omega\epsilon_2(\omega)$, and $Z_0 \equiv \sqrt{\mu_0/\epsilon_0}$ is the impedance of free space. (Aside: For some reason, it is tradition to use subscripts on σ to denote real and imaginary parts, as opposed to primes.) We will revisit this conversion in Chapter 3.

So now, we can say that if we consider only magnetic fluctuations (essentially set $\sigma_1(\omega) = 0$) the THz absorption is proportional to the dissipative part of the response function, $\chi''(\omega)$, which is in turn related to the two-spin correlation function as probed

by INS by the fluctuation dissipation theorem by Eq. 2.6. Our THz absorption spectra may be compared directly with INS spectra at $\boldsymbol{Q} = 0$

With this in mind, we ask the question: how can optical measurements complement the INS spectra for α-$RuCl_3$ described in the previous section?

Just as optics cannot probe non-zero momenta, INS measurements cannot directly probe $\boldsymbol{Q} = 0$. Excitations at near- zero momentum may be extracted from INS measurements by integrating over a small region in k-space from negative to positive out-of-plane wavevector. As such the linewidth of spectral features at $\boldsymbol{Q} = 0$ as measured by INS are necessarily broadened by this integration.

Additionally, as will be described in the following Chapter 3 and 4, from the THz absorption spectra we can actually extract the exact values of χ''. INS spectra are necessarily always reported as scattering intensities, with arbitrary units. The exact quantification of the response function allows us to employ a Kramers-Kronig analysis to relate $\chi''(\omega)$ to the static susceptibility $\chi(0)$ enabling direct comparison with transport measurements.

Thus the motivation for our THz measurements in clear– this technique offers excellent energy resolution at $\boldsymbol{Q} = 0$, high modularity in terms of exploring the phase space of polarization, and temperature, and finally the capability to exact precise values for response functions. In following Chapters, we will discuss polarized THz spectroscopy measurements on α-$RuCl_3$, performed in the Orenstein lab in 2017 and 2018 as the literature on this material was developing. We note that are now several complementary optical studies on α-$RuCl_3$, apart from those presented in this thesis, some of which extend measurements out to fields above H_c including FTIR/THz measurements [76] and electron spin resonance [77]. The work presented here was the first high-resolution optical observation of the magnons in α-$RuCl_3$, allowing for comparison with the resonances observed by INS.

2.4.4 PHASE DIAGRAM, OTHER PROBES AND THERMAL HALL

In the past five years, the phase diagram of α-$RuCl_3$ has been explored extensively by many probes, including optics, specific heat, [57, 61, 78] nuclear magnetic resonance, [67] and thermal transport, [68, 79–81]. A cartoon of general phase diagram, drawn from a survey of many of the measurements mentioned above is shown in Fig. 2.4 (b). In general, measurements indicate a transition to a gapped magnetically disordered state above H_c, before entering a partially field-polarized ferromagnetic state around 10-13 T.

More recent field-dependent INS data tracked magnetic excitations with higher energy resolution by using a massive (2 g!) single crystal to report a magnetic continuum in the range of 7.5 -8 T. In combination with magneto-caloric data this work also detected anomalies on the edges of the intermediate phase at 6T and 9 T [5]. The higher field

anomaly and the intermediate field phase which is interesting in the context of Kitaev physics.

The most intriguing experimental evidence to date, is the report of a quantized half-integer thermal Hall (κ_{xy}) plateau for off-axis applied fields in the range of approximately 7 to 9 T. The quantized thermal Hall probes directly heat transport by neutral excitations – in this case Majoranas– where the observation of half-integer quantization matches the theoretical prediction for chiral edge modes [6] In effect, these these measurements suggest that a topological phase may exist in the vicinity of H_c. In short the application of magnetic field gaps the Majorana dispersion spectrum (which is a Dirac cone at zero field). The resulting bands have Berry curvature and hence a non-zero Chern number with opposite sign for each band. This gives rise to the topologically protected edge currents that may be probed by thermal Hall. An additional phase transition out of the disordered phase at a higher field, H_u around 9 T, corresponds to the disappearance of the quantization plateau in these measurements.

Understanding of these results is still developing– for example theoretical studies found that thermal hall could result from Berry curvature of magnon bands, but it would not be half-integer quantized [82]. What's more, within the same month of the publication of this dissertation, the same group that reported the original thermal hall measurements [6], reported a half-integer quantized anomalous κ_{xy}, that is for fields completely in the Ru-Ru plane [83]. Strikingly this work contains a study of quantized κ_{xy} as a function of field tilt angle– and in combination with theoretical results sign of the κ_{xy} plateau tracks the calculated sign of Chern number as a function of applied field tilt angle.

As of the writing of this dissertation, to our knowledge, the quantized thermal Hall results have not been successfully repeated by other groups. Thermal hall measurements are notoriously difficult from a technical standpoint. Thus, while these results are very intriguing, the nature of the disordered state in α-$RuCl_3$ above H_c and its low-energy excitations remains a topic of discussion and exploration in the field.

3

TIME DOMAIN TERAHERTZ SPECTROSCOPY

3.1 PHENOMENA IN THE FAR INFRARED

Terahertz (THz) refers to the region of the electromagnetic spectrum in between infrared and microwave, at with wavelengths of about 300 μm, or photon energies of 4.16 meV. This energy range is typically inaccessible by RF circuits, which top out at around 100 GHz, or 0.1 THz. The THz region is likewise outside the accessible range of conventional photonics, or free-space optical techniques. The standard 800 nm Ti:Sapphire ultrafast laser pulses found many optics may be converted to lower energies via nonlinear optical parametric amplification and difference frequency generation, producing pulses with wavelengths up to around 20 μm. Fourier transform infrared (FTIR) spectroscopy techniques which utilize broadband light sources, typically filament lamps, can access energies as low at a few THz. As such, with less-developed technology, this intermediate energy range around 1 THz is often termed the "THz gap". However, there are many interesting phenomena in condensed matter physics which emerge in this far-infrared energy range. For example, the binding energy of Cooper pair in a BCS superconductor is typically on the order of hundred of GHz. In general, quasiparticle excitations in strongly correlated materials with lifetimes on the order of a hundreds of femtoseconds to a few picoseconds may be accessed by THz frequencies. Such phenomena include collective excitations of charge (plasmons) in a 2D electron gas or, of particular interest to this work, excitations of ordered spins (magnons) in magnetic materials.

Time-domain Terahertz Spectroscopy (TDTS), is a self-calibrated technique which allow us to explore how these collective modes interact with electromagnetic radiation by measuring complex material response functions in this intermediate spectroscopic range. Frequency-domain spectroscopies probe only the amplitude of the transmitted (or reflected) electric field – in this case complex response functions can only be extracted by Kramers-Kronig transformations and cannot be converted to calibrated numbers. TDTS, on the other hand directly measures the full complex material response functions through the coherent generation and detection of THz radiation in the time domain [84]. This

property enables useful, direct comparison of THz measurements with DC measurements of the conductivity or susceptibility as measured by other probes.

In the early days of the Orenstein lab during the 1990 and early 2000s, a primary research focus the group was centered on THz studies of thermal fluctuations superconducting thin films. For this work, the photoconductive antennas were designed and were fabricated in-house by graduate students, and even the focusing mirrors for the generated THz radiation were custom-fabricated at LBL [85]. In the intervening years, while the group's research focus shifted towards time-resolved and symmetry sensitive techniques, THz technology advanced and became far more readily commercially available. In 2015, the group decided to revisit THz techniques and since then there two TDTS systems have been built and used in the lab, which we will refer to as the "Small THz" system and the "Magnet THz" system for descriptive purposes in this thesis.

The first part of this chapter consists of an overview the general operating principle of TDTS, including THz generation, collection, and data analysis. We will then discuss the technical details and applications of the two home-built TDTS systems used to perform the measurements presented in this thesis.

3.2 INTRODUCTION TO TDTS

In general there are two common methods for generation of THz light in table-top optical experiments. The first method involves ultrafast excitation of biased photoconductive antennas (Auston switches) which can generate THz in the range of 0.1 to 2 THz depending on the semiconductor substrate material and antenna design. The second method makes use of nonlinear optics, wherein THz light is produced via sum-frequency generation by shining an ultrafast laser pulse on an inversion breaking crystal (typically ZnTe or LiNbO), and is detected by an electro-optic sampling technique. This second method typically requires higher power laser pulses and can produce radiation out to higher energies (order of 3-4 THz) [86].

In both of the existing spectrometers in our lab, THz pulses are generated by commercially produced photoconductive antennas. The photoconductive antennas consist of dipolar electrodes patterned onto a semiconductor substrate. The electrodes are separated by a small gap, typically on the order of 5 - 10 μm. Commonly used semiconductor materials include Si, GaAs, and In-GaAs. Of course the choice of antenna substrate depends on wavelength of the ultrafast laser and desired THz bandwidth. A schematic of a TDTS system, in particular the Small THz system is shown in Fig. 3.1.

The first step in TDTS is an ultrafast laser pulse, typically in the IR (λ= 800 nm or 1550 nm, depending on antenna substrate) and around 100 femtosecond (fs 10^{-15} s) in length with an repetition rate of typically 80 - 100 MHz. The pulse is split into two

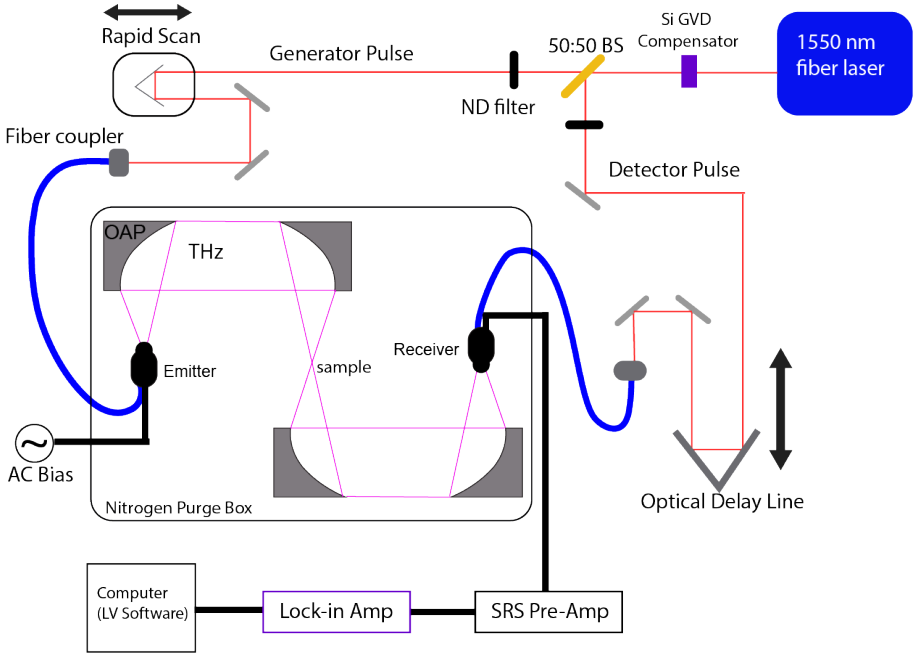

Figure 3.1: Schematic of fiber-coupled TDTS system.

synchronous pulses by a beam splitter resulting in a "generator pulse" and a "detector pulse". The generator pulse is manipulated by standard silver mirrors along one arm of the spectrometer and eventually focused onto the dipole of the emitter antenna either through free space optics or an optical fiber as shown in Fig. 3.1. Photoexcited carriers are generated in the semiconducting substrate and accelerated across the antenna electrodes gap by an applied AC bias voltage.

This results in a transient photocurrent, $\boldsymbol{j}(\mathrm{t})$, and therefore an oscillating dipole moment $\boldsymbol{P}(\mathrm{t})$ which will radiate time-dependent electric field $\boldsymbol{E_{THz}}(\mathrm{t})$. In the far-field limit, $\boldsymbol{E_{THz}}(\mathrm{t})$ depends on the second derivative of this dipole moment [87] :

$$\boldsymbol{E_{THz}}(t) = \frac{1}{4\pi\epsilon_0 c^2 r}\hat{r} \times (\hat{r} \times \frac{d^2\boldsymbol{P}(t)}{dt^2}) \tag{3.1}$$

Where $d\boldsymbol{j}(t)/dt = d^2\boldsymbol{P}(t)/dt^2$. For each incident laser pulse, a single-cycle of $\boldsymbol{E_{THz}}(\mathrm{t})$ or a "THz Pulse" is emitted. The THz pulse is broadband, in our case containing frequencies in the range of 0.1 to 2 THz with reasonable signal to noise.

The generated THz is coupled from the antenna to free space by a hyper-hemispherical Silicon lens, and is diverging as it exits the lens. The radiation is collimated and then focused onto the sample (or simply an empty aperture) by two gold-coated off-axis parabolic mirrors (OAPs) as illustrated in Fig. 3.1. The transmitted light is then re-collimated and

then focused onto a receiver antenna by two additional OAPs. All THz optics are enclosed in a box which is continuously purged with dry nitrogen, as water found in the ambient environment is strongly absorbing in the range 0f 1- 2 THz.

To detect the the amplitude of the transmitted THz electric field, the synchronous detector laser pulse split off initially at the beamsplitter is sent through an optical delay line consisting of a retroreflector mounted onto a motorized stage before being focused onto the receiver antenna. The detector laser pulse generates photocarriers in the receiver substrate. However, on the receiver end, there is no external bias voltage applied to the antenna. Instead, carriers are accelerated across the antenna gap by the incident THz electric field itself when the arrival of $\boldsymbol{E_{THz}}(\mathrm{t})$ at the receiver overlaps in time with the detector pulse.

The time variation of $\boldsymbol{E_{THz}}(\mathrm{t})$ is measured by scanning the time-delay of the detector pulse with respect to the generator pulse by scanning the position of a retroreflector mounted to an optical delay line where 0.02 mm delay line step corresponds to 0.067 ps of time delay. The receiver photocurrent at each value of time delay is amplified by a current pre-amp and then demodulated using a lock-in amplifier at the modulation frequency of the bias voltage applied to the emitter, typically in the kHz range, and in our set up, this is precisely 32 kHz for historical reasons [85]. In this way we sample the amplitude of $\boldsymbol{E_{THz}}(\mathrm{t})$ as a function of time on the sub-picosecond time scale; essentially we coherently detect the THz pulse in the time domain. THz transmission spectra are then extracted time-domain pulses via a Fourier transform analysis and normalized to a reference scan, as will be described in the following section.

3.3 MEASUREMENT AND ANALYSIS OF THZ SPECTRA

3.3.1 THZ ANTENNA BANDWIDTH

There are several important factors to consider when setting up a new antenna-based TDTS system which depend on what space is available, what the wavelength of the available ultrafast laser, and what size of THz focus is required, and what is the relevant frequency range for the materials to be studied.

The spectral range achievable by the system is determined by the timescale of the generation and detection process. A simple model of photocurrent generation and THz emission is presented in Refs. [85, 87, 88] and is useful for understanding the relevant timescales in the generation of $\boldsymbol{E_{THz}}(\mathrm{t})$. Recalling Eq. 3.1, the radiated $\boldsymbol{E_{THz}}(\mathrm{t})$ is related to the transient photocurrent generated in the antenna, $d\boldsymbol{j}(t)/dt \propto \boldsymbol{E_{THz}}(\mathrm{t})$. The first relevant time scale is determined by the generator ultrafast laser pulse, which finite duration (around 100 fs) and temporal pulse shape which we will denote by L(t).

The generated photocarrier current density may be described by the convolution of the L(t) with the carrier response in the semiconductor substrate:

$$\boldsymbol{j}(t) = L(t) \otimes (n_e(t) q v_e(t)) \tag{3.2}$$

Where $n_e(t)$ and $v_e(t)$ are the transient carrier density and velocity in the emitter antenna. These quantities are dependent on the scattering and recombination times of the carriers, which are materials properties of the semiconductor. The average carrier acceleration in response to a bias voltage (E_b) applied across the antenna is given by Drude model:

$$\frac{dv_e(t)}{dt} = -\frac{v_e(t)}{\delta}\tau_s + \frac{q}{m^*}E_b \tag{3.3}$$

Where τ_s is the characteristic carrier scattering time in the semiconductor, q is the charge and m^* is the carrier effective mass. The transient carrier density, $n_e(t)$, can be approximated by:

$$n_e(t) \propto e^{-t/\tau_r} \tag{3.4}$$

Where τ_r is the photocarrier recombination time. As a result we can see that there are three relevant time scales in $\boldsymbol{j}(t)$ and thus three relevant time scales in generating the THz electric field, as $\boldsymbol{E}_{THz}(t) \propto d\boldsymbol{j}(t)/dt$. These are determined by τ_s, τ_r and the pulse length. The time constants τ_s, τ_r are material properties of the semiconductor substrate, were τ_s is typically on the order of a hundred to a few hundred fs and τ_r may range from 200 fs for GaAs to 1 ps for Si. The bandwidth of the THz pulse is determined by the fastest of these timescales. These are important elements to consider when designing a THz spectrometer with optimal bandwidth, and a more detailed discussion of optimizing antenna properties can be found in Refs. [85, 88]. In those works antennas were designed and fabricated by graduate students in-house– size and design of the antennas also plays a role in the achievable THz bandwidth.

For the measurements reported in this work, we use two different sets of commercially produced antennas. In the case of the Small THz system, we use fiber-coupled InGaAs antennas produced by Fraunhofer. Here, we find that our working bandwidth in fact limited by dispersive optical elements in the the path of the generating laser pulse which induce temporal broadening (discussed in the following section). In the Magnet THz system we use free-space coupled GaAs antennas produced by Te-TechS. The bandwidth specifications of each set of antennas are shown in Fig. **??**. It is useful for comparison purposes to express the THz emission in decibels (dB) as a power spectrum referenced to the peak emission, that is,

$$FFT(\omega) = 10 \log \frac{P(\omega)}{P_0} \text{dB} \tag{3.5}$$

The -20 dB point is often quoted as a measure of the effective THz bandwidth where high signal to noise is achievable.

Specifications for the bandwidth of each set of THz antennas may be found in the respective data sheets. The two sets of antennas have somewhat similar bandwidth range, reaching the noise floor at around 5 THz in either case. For the fiber coupled InGaAs antennas, the power spectrum plotted in Fraunhofer HHI data sheet for antenna receiver serial no. RP150502 shows the -20 dB point is at 1.90 THz. The power spectrum for the GaAs antennas, printed in the TeTechS Inc. User Guide, shows the -20 dB point is at 2.24 THz. In practice, the THz bandwidth achieved by the system is also limited by other factors, such as the size THz focus with respect to the aperture the sample is mounted on as well as limitations imposed by data acquisition and analysis. For instance, our Magnet THz system using the free-space GaAs antennas is stable up to around 2 THz. The capabilities of each system will be discussed further in Section **??**.

3.3.2 DATA ACQUISITION AND ANALYSIS

As mentioned previously, the detection technique with the receiver antenna is essentially the reverse process to THz generation except in this case the THz electric field provides the bias voltage and the photocurrent created across the receiver by the the detection laser pulse is what we measure. This resulting photocurrent, $\boldsymbol{j_r}$(t) is proportional to THz electric field incident on the receiver. Recalling Eq. 3.1, $\boldsymbol{j_r}$(t) may be expressed as a convolution with biasing THz electric field an the material properties of the receiver, in the absence of intermediate absorbing media:

$$bmj_r(t) = L^r(t) \otimes (n_r(t) q v_r(t)) \otimes \boldsymbol{E^e_{THz}}(t) \tag{3.6}$$

Where $\boldsymbol{E^e_{THz}}$(t) is the THz field incident on the receiver and L^r(t) represents the the detector laser pulse. The electric field radiated by the emitter is proportional to $\boldsymbol{dj(t)/dt}$ (Eq. 3.1). On the receiver end the current $\boldsymbol{j_r(t)}$ is measured directly with the preamplifier, and is this directly proportional to the detected THz electric field $\boldsymbol{E^r_{THz}}$. We want to analyze the detected electric in the frequency domain. A convolution in the time domain is a multiplication in the frequency domain,

$$\boldsymbol{E^{r,0}_{THz}}(\omega) \propto \boldsymbol{j_r(\omega)} = L^d(\omega)(n_r(\omega) q v_r(\omega))\boldsymbol{E^e_{THz}}(\omega) \tag{3.7}$$

Where $\boldsymbol{E^{r,0}_{THz}}(\omega)$ is the measurement of the electric field of in the absence an absorbing sample.

$$\boldsymbol{E^{r,S}_{THz}}(\omega) \propto T_s(\omega) L^d(\omega)(n_r(\omega) q v_r(\omega))\boldsymbol{E^e_{THz}}(\omega) \tag{3.8}$$

We note that these are in fact complex quantities, and the complex THz transmission spectra of the sample can be obtained by referencing $\boldsymbol{E}_{\boldsymbol{THz}}^{\boldsymbol{r,s}}(\omega)$ to $\boldsymbol{E}_{\boldsymbol{THz}}^{\boldsymbol{r,0}}(\omega)$:

$$T_s(\omega) = \frac{\boldsymbol{E}_{\boldsymbol{THz}}^{\boldsymbol{r,S}}(\omega)}{\boldsymbol{E}_{\boldsymbol{THz}}^{\boldsymbol{r,0}}(\omega)} \tag{3.9}$$

In this way, we can effectively divide out the response of the receiver antenna and detector laser pulse, as well as absorption from additional elements in the THz path (for example cryostat windows) to obtain a calibrated measure of $T_s(\omega)$

In practice, to obtain THz spectra from time domain pulses, we employ a data analysis scheme where the transmitted THz pulses are converted to the frequency domain by Fast Fourier Transform (FFT). The general data acquisition and analysis scheme for the TDTS measurements presented in this work is illustrated in Fig. 3.2. The detector photocurrent is read out via a SRS current preamplifier and a lock-in amplifier (we have used both older SRS lock-ins as well as newer Zurich Instruments lock-ins). The time trace data (Fig. 3.2 (a)) is recorded in a LabView program written to files. Further data processing and analysis is performed offline, typically in python.

For the work presented in this thesis, samples of single crystal α-$RuCl_3$ are affixed to a sample mount which consists of a cooper plate with an precision machined aperture, typically 3 - 5 mm in diameter. The red trace in Fig. 3.2 (a) shows an example THz time trace as transmitted through a sample glued on top of an aperture. To obtain $T_s(\omega)$ by the referencing procedure described above, we measure the electric field transmitted through an identical, blank aperture (green trace in Fig. 3.2 (a)). The sample and the blank aperture are both mounted in the cryostat at a fixed vertical distance from one another on the sample stick. While taking data, the sample and reference scan on the aperture are taken in sequence for the same conditions by vertical translating the sample stick between scans.

The sample pulse plotted in Fig. 3.2 (a) shows multiple pulses separated by 13 ps. In α-$RuCl_3$, weak absorption leads to a sequence of transmitted pulses in which the first traverses the sample once and subsequent echo pulses undergo multiple reflections and traversals through the sample. Assuming THz radiation is plane waves with linear polarization we can analytically express $T_s(\omega)$ in the linear response regime [89]. Consider a flat sample of thickness d and complex index of refraction $\tilde{n}_2$ sitting in a medium of index $\tilde{n}_1$ (in our cryostat, this is typically dilute helium gas, with $\tilde{n}_1 \approx 1$). The transmission through the sample can be written:

$$T_s(\omega) = T_{12}(\omega)S(\omega)T_{21}(\omega)\sum_{i=0}^{\infty}\{R_{21}(\omega)S(\omega)R_{21}(\omega)\}^i \boldsymbol{E}_{\boldsymbol{THz}}(\omega) \tag{3.10}$$

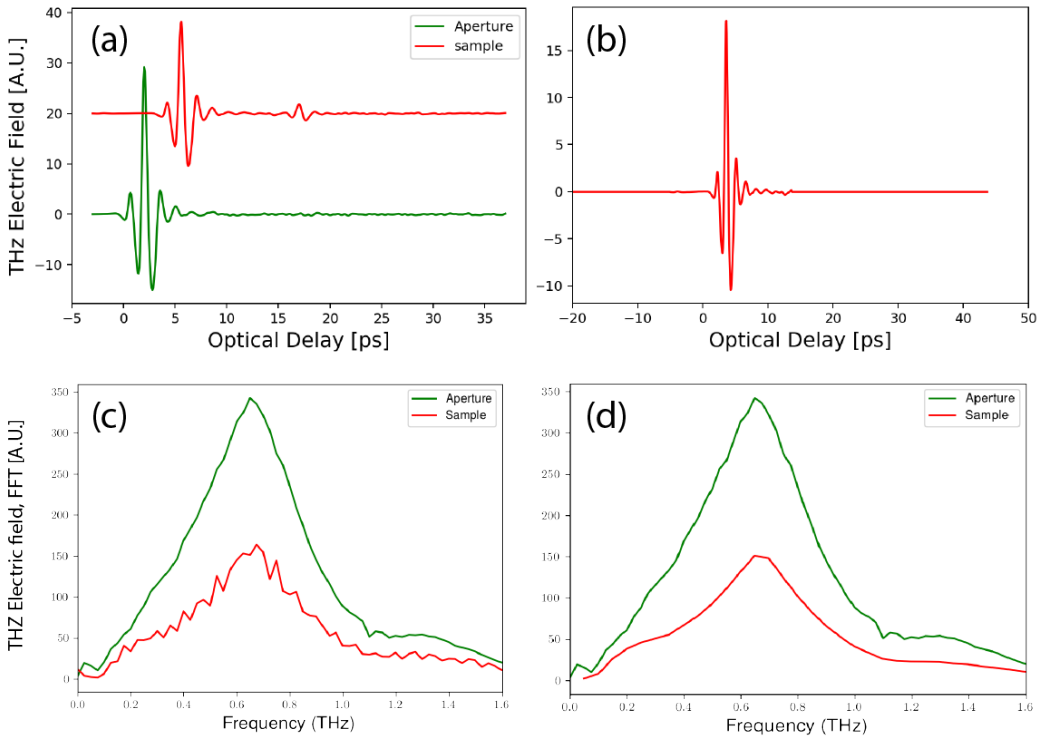

Figure 3.2: (a) THz pulses in the time domain for transmission through an empty 3 mm aperture (green) and a through a α-$RuCl_3$ sample mounted on an identical 3 mm aperture. (b) THz pulse transmitted through the sample with windowing procedure applied. (c) THz spectrum (FFT of panel (a)) for aperture and sample. Fabry-Perot oscillations in sample spectrum arise from inclusion of echo pulse in the FFT. (d) FFT of processed sample pulse in panel (b) reduces Fabry-Perot oscillations.

Where $T_{12}(\omega)$, $T_{12}(\omega)$, and $R_{21}(\omega)$ represent the transmission and reflection coefficient at the interface between the sample and the surrounding gas from the Fresnel equations, where in general:

$$T_{ab} = \frac{2\tilde{n}_a}{\tilde{n}_a + \tilde{n}_b}, \; R_{ab} = \frac{\tilde{n}_a - \tilde{n}_b}{\tilde{n}_a + \tilde{n}_b} \tag{3.11}$$

And $S(\omega) = e^{-i\omega\tilde{n}_2 sd/c}$ is the exponential attenuation of the THz light as it propagates through the sample. The contribution from echo pulses of decreasing amplitude per number of total round trips i is contained in the sum in Eq. 7.1, resulting in a Fabry-Perot modulation of $T_s(\omega)$. Fig. 3.2 (c) shows the FFT of the red trace in panel (a), clearly demonstrating the Fabry-Perot modulation of the spectrum. This modulation can make it challenging to decipher spectral features.

For the α-$RuCl_3$ samples studied in this work, crystals are sufficiently thick (around 0.8 to 1 mm) such that the echo pulse is well-separated in time from the main pulse, as showing in Fig. 3.2 (a). We can removed Fabry-Perot oscillations in the data analysis procedure by restricting the time delay window over which we the the FFT include only the first pulse.

In practice, restricting the time domain window is done by truncating the time trace to exclude the echo pulse. However we must consider that alteration of the time trace data effects the resolution of the FFT. This is simply because parameters of the time trace scan, when transformed into the frequency domain set the resolution, $\delta\omega$ and maximum frequency ω_c of the FFT. The resolution is related to the scan length, L by $\delta f = c/(2L)$, that is, the longer the scan, the higher the resolution. In the same way, the step size of the optical delay line, δL, sets the maximum frequency attainable by the FFT, a result of the Nyquist condition $\omega_c = c/4\delta L$. To analyze the data we truncate time domain data just before the echo pulse, append zero-padding on either side of T_0 to extend the time trace, and apply a Hanning window function to the data to minimize the contribution of points at the edge of the zero pad. Zero-padding is also applied to the aperture pulse such that the two scans match in length. Fig 3.2 (b) shows the processed time-domain data, and Fig. 3.2 (d) shows the resulting FFTs, without Fabry-Perot oscillations.

It is important to note that while zero padding does not increase the fundamental resolution of the frequency-domain data, it simply increases the density of points in the FFT. This smoothing effect is helpful for fitting absorption peaks in the spectra [88, 90]. We also found that too much zero padding broaden absorption peaks in the processed data, which can be problematic when trying to extract precise fit parameters. So zero-pad with care. In our measurements, the step size of the raw time trace is set to 0.02 mm, corresponding to 0.125 THz or 0.05 meV.

Dividing the sample FFT (red) by the aperture FFT (green) in Fig. 3.2 (d) yields the complex transmission for a single pass through the sample. We can write the transmission analytically using Eqs. 7.1 and 3.11:

$$T(\omega) = \frac{4\tilde{n}}{(\tilde{n}+1)^2)} e^{[ik_0 nd]} e^{[-k_0 \kappa d]} \tag{3.12}$$

Where we have now we written $S(\omega)$ from Eq. 7.1 in terms of the frequency-dependent real and imaginary parts of the sample index ($\tilde{n} = n + i\kappa$) and the free space wave vector the light ($k_0 = \omega/c$).

To covert $T(\omega)$ to the complex absorption spectrum, we consider that the absorption $\alpha(\omega)$, relates the intensity of incident and transmitted light, which is proportional to the square of the optical fields [17] and take the magnitude of Eq. 3.12. For the measurements on α-$RuCl_3$presented in this thesis, we consider that because α-$RuCl_3$is an insulator, and therefore weakly absorbing at THz frequencies, $n \gg \kappa$. With this approximation the coefficient in Eq. 3.12 simplifies and we may write:

$$|T(\omega)| = \frac{4n}{(n+1)^2)} e^{-\alpha(\omega)d} \tag{3.13}$$

Where the absorption coefficient is given by $\alpha(\omega) = \omega\kappa(\omega)/c$

3.3.3 CONVERSION TO OPTICAL RESPONSE FUNCTIONS

As discussed in Chapter 1, THz photons may be absorbed via magnetic or electric dipole interactions. We are interested in quantifying these interactions by measuring complex optical response functions, optical conductivity $\sigma(\omega)$ and the magnetic susceptibility, $\chi(\omega)$. Recalling Eq. 2.10, in the THz regime for α-$RuCl_3$, we can write $\alpha(\omega)$ as the sum of contributions from the magnetic and dielectric response functions.

$$\alpha(\omega) \cong \frac{n\omega\chi''(\omega)}{2c} + \frac{\sigma_1(\omega)Z_0}{2n}, \tag{3.14}$$

The factor, nd/c, is evaluated directly from the time delay between the arrival of the first and second pulses at the detector. This time interval is the roundtrip time, T_{rt}, which is equal to $2nd/c$. As described in Chapter 4, determination of $\chi''(\omega)$ from the magnetic-dipole component of the absorption is self-calibrated, as it is extracted using only observables obtained from our measurement, that is,

$$\chi''(\omega) = \frac{4\alpha(\omega)d}{\omega T_{rt}}. \tag{3.15}$$

In Chapter 4, we will discuss how for α-$RuCl_3$, this analysis allows us to convert $T(\omega)$ to an calibrated measurement $\chi''(\omega)$, enabling direct comparison with other probes.

3.4 EXPERIMENTAL APPARATUS

Here we will discuss the specific details of the two custom-built THz spectrometers currently installed in the Orenstein lab, both of which use photoconductive switches to generate light. The first spectrometer constructed in 2015, dubbed the Small THz, is located room 358 and operates with a continuous-flow Janis Instruments cryostat which can reach temperatures as low as 2 K. The Magnet THz system is located in room 360 and operates in conjunction with a 7-Tesla split-coil superconducting magnet cryostat.

3.4.1 SMALL THZ SYSTEM

The Small THz system is located in room 358. A schematic of this system is showing in Fig. 3.1 and 3.4 (a). The antennas used in this system are fiber-coupled InGaAs antennas manufactured by Fraunhofer. The generating ultrafast laser pulse is produced by a Toptica Photonics FemtoFiber Pro 1550 nm laser pulse from a Toptica Er-doped fiber laser. The nominal pulse length is 80 fs with an 80 MHz repetition rate. A 50:50 beam splitter and sent into the generation and detection arms of the spectrometer via free-space optics. The generating and detecting pulses are directed onto the emitter and receiver antennas respectively by coupling to optical fibers which are coupled to with the antennas from the manufacturer.

3.4.1.1 FIBER COUPLED ANTENNAS

The modularity of the fiber-coupled antennas offers some advantages, the biggest one being that should the alignment of the laser change before reaching the antennas, one can simply re-couple the laser to the fibers and recover the THz pulse without major realignment the THz optics.

Coupling the fibers can be tedious at first, but once a user has gone through the process a couple of times it becomes relatively straightforward. Here we offer a brief description of the fiber coupling procedure.

The generator (or detector) laser pulse is directed into a ThorLabs FiberPort coupler, which consists of a coupling lens on one side and and a fiber plug in port on the other. The fibers connected to the antennas are about 1 m long and are single mode. It is worth noting that one should take care when handling the antenna fiber: in particular take care

when plugging it into the FiberPort and when routing the fiber to ensure that it bends smoothly.

To optimize the optical power on the antennas, we employ a process of peaking up the coupling using a series of auxiliary fibers, which we will describe briefly here. The process is the same for coupling both the emitter and receiver.

First, un-plug the antenna fiber from the FiberPort and install the (blue) multi-mode auxiliary fiber. The other end of the fiber can be directly connected to a ThorLabs power meter, which will almost certainly show no coupled light at first. To start off the alignment, direct the laser into the FiberPort using the two steering mirrors and a fluorescent iris – there should be two aligned post holders installed on the table in front of the FiberPort. After this, check where the beam hits the lens of the coupler and adjust by hand the position of the FiberPort until you see some power (typically in the μW range). After this, at first just make small tweaks the knobs of the steering mirrors to see if you can get any maximization. Proceed to maximize the power on by "walking" beam into the coupler, that is changing the position of the beam without changing the angle of the beam. First, center the beam on the lens of the FiberPort–in either the horizontal or vertical axis, do one at a time– using one of the knobs on the mirror closest to the FiberPort. This will reduce the power. Use the opposing knob on the other (further) mirror to move the beam back, which should correspond to an increase in optical power. Once a maximum is reached, try the other axis.

The FiberPort coupler does have set screw adjusters labeled x and y, which set the position of the lens, as well as three tilt adjusters (labeled z) which may be with a small hex wrench. It may be necessary to adjust the tilt adjusters at the beginning of coupling. Once there is some power detected, in general it is better to use the steering mirrors to do most of the coupling as described above. On occasion you may hit a point where no further optimization can be achieved using the mirrors in which case it may be necessary to try adjusting the set screws. Tread carefully, however, as they appear to suffer from severe mechanical hysteresis.

Once the coupling on the multi-mode auxiliary fiber is optimized (typically 50 percent coupling efficiency is enough), move on to the (orange) single-mode auxiliary fiber and repeat the same procedure. Once the maximum is reached, limit the power by adjusting a continuously tune-able neutral density filters (should be placed in both the generator and receiver arms). The receiver antenna in particular should not have more than 20 mW of optical power on it– typically we operate around 10 mW.

Plug the antenna fiber into the FiberPort and optimize. It is not possible to directly read out the power on the antenna using the power meter, so coupling to the antenna is done using a simple voltage divider circuit and a digital multimeter. The antenna resistance is included in a voltage divider circuit with a shunt resistor of comparable value to the

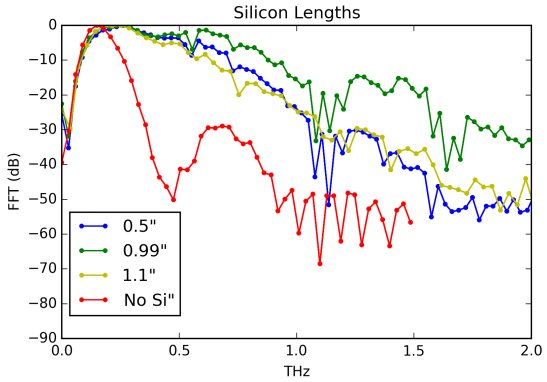

Figure 3.3: Bandwidth optimization with dispersion compensation. Red trace is the bandwidth using no dispersion compensation. Green, blue, and yellow traces correspond to different path lengths through Silicon placed in the beam path of the ultrafast laser pulse. The 0.99" Si path length (green) provided optimal bandwidth. Absorption lines around 0.5 and 1.0, and 1.5 correspond to absorption from water vapor in the air.

antenna resistance. A small (3 V) voltage is supplied by a battery, and the voltage drop across the shut is measuring. When the coupling to the antenna is optimized, the antenna resistance will decrease, hence increasing the voltage dropped across the shunt.

After the coupling is optimized, plug in the BNC cable for each antenna. The antennas should never be reverse biased, and for safety the BNCs first plug directly into a small home-built Zener diode (break down voltage 3.3 V) protection circuit (same on each antenna). After that, the emitter antenna is connected to the bias voltage source, and the receiver is plugged into the preamp for photocurrent readout.

Finally, we note that for future iterations of this spectrometer, it may be worthwhile to install a telescope before the FiberPort to collimate the beam to make the coupling procedure easier. Note that this will require some additional modifications, as adding a telescope will change and path length and add group velocity dispersion to the pulse.

3.4.1.2 DISPERSION COMPENSATION

Fiber coupled antennas are an convenient choice because they decouple the alignment of the optical elements before the antennas (the beam splitter, mirrors, and delay lines) from the the THz optics (antennas and OAPs). Even if the optical elements outside of the THz box change, either intentionally or on accident, the laser can simply be coupled into the fibers and the THz pulse may be recovered without realignment of the OAPs. In this way,

the THz optics are effectively decoupled from the laser optics, and the entire system can be brought up relatively painlessly to full functionality after a period of down time.

However, the propagation of the pulse through the optical fibers presents an additional challenge. An ultrafast laser pulse consists of a broad range of frequencies; mode-locked pulses are generated when the discrete longitudinal optical modes of the laser's cavity are superimposed with a fixed phase difference, $\psi(\omega_o)$, between adjacent modes. When a pulse travels through a dispersive optical element, for instance a SiO_2 optical fiber, each frequency mode contained in the pulse gains an additional phase which changes the relative phase between the modes.

$$E_{out}(\omega) = E_{in}(\omega)e^{-i\psi(\omega-\omega_o)} \tag{3.16}$$

Where frequency-dependent phase factor is $\psi(\omega-\omega_o)$. The exponential in this expression maybe Taylor expanded, $\psi(\omega-\omega_o) = \psi + \psi'(\omega-\omega_o) + \psi''(\omega-\omega_o)^2/2 + \mathcal{O}((\omega-\omega_o)^3$ The lowest order term in this expansion which will affect the pulse shape is the second order term which is related to the second derivative of the index of refraction with wavelength is is usually referred to as the group delay dispersion (GDD) or group velocity dispersion (GVD). While all the higher orders of $\delta(\omega)$ contribute to the dispersion of the pulse and change the pulse shape, the GVD corresponds to temporal broadening. [91]

For the antennas used in this system, the optical fibers are about 1.02 m long and introduce GVD and therefore temporal broadening of the generating laser pulse. This broadening will greatly decrease the THz bandwidth of the THz system, as illustrated by the red curve in Fig. 3.3. Thus to optimize the THz bandwidth, it is necessary to counteract this dispersion by adding additional GVD of the opposite sign into the laser beam path. This is a problem not unfamiliar to the the time-resolved experiments in our lab. For instance the sub-picosecond resolution pump-probe experiments at 800 nm in our lab [92], dispersion may be compensated for by use of standard prism-pair compressor. The prism compressor works by adding negative, or "anomalous" GVD to compensate for positive GVD at 800 nm associated with optical elements in the set up such as lenses and beamsplitters.

However, to compensate for the dispersion of the 1550 nm laser pulse in SiO_2, the prism compressor method will not work. This is because 1550 nm is above the zero-dispersion point for SiO_2, that is the GVD at 1550 nm for SiO_2 is -32.692 fs^2/mm. In fact, the zero-dispersion point at 1273 nm is a commonly exploited property in optical fiber communications. However in this case it means that it is necessary to come up with an alternative method of adding positive GVD. One option involves purchasing dispersion-compensating fibers, but this involves multiple couplings from free space to fibers, which can be lossy.

Another method is to simply introduce chunks of material with the correct GVD and length into the beam path. The two materials investigated were rods of N-SF6 glass and elemental Silicon. While N-SF6 rods need to be custom produced, optical quality Silicon windows are commercially available (up to 5 mm thick from ThorLabs), so this may be a good option for future projects. For this application, we obtained several blocks of elemental silicon of varying thicknesses. The GVD for Si at 1560 nm is 1108.8fs^2/mm (via refractiveindex.info), so in order to compensate for 1.02 mm of SiO_2 the beam will need to traverse about 30 mm of bulk Silicon. Of course placing bulk material in the beam path does not have the same continuous dispersion tune-ability afforded by a prism pair, and optimizing the path length through the Si involves some trial and error. Ideally, our aim is to obtain the optimal path length through the Si block for dispersion compensation while minimizing the power lost from reflection at the Si to air interface. To achieve this, a Si block was cut to length for the laser to enter at Brewster's angle which is about 74 degrees for the Si (n = 3.477) to air (n = 1) interface and traverse 30 mm before emerging again into air. At Brewster's angle, p-polarized light is transmitted and -polarized light is reflected. As the Toptica laser is already horizontal (p-polarized already with respect to the Si plane of incidence) this configuration will offer the maximum power transmitted.

The Si we received had a rough polish which was insufficient for optimal power transmission. It was polished to near-optical quality by hand using a series of fine-grained polishing pads, in the order of decreasing grain size. The polishing pads were lubricated with acetone, and the Si was polished using a figure-8 motion. Unfortunately, this can take several hours.

Once cut and polished Si was placed in the beam, before the beam splitter on a linear translation stage. The amount of path length traversed was adjusted by tweaking the Si angle with respect to the beam and scanning the linear translation stage. A THz spectrum was taken in several configurations until an optimal bandwidth was found using a block about 1 inch in width. In practice, the angle of incidence that gave us optimal path length using the block we had was far off from Brewster's angle, but as the Toptica laser has a much higher average power (around 400 mW) than is required for THz generation, some reflection loss is acceptable. In the best bandwidth configuration found, the transmitted power through the block is around 160 mW, which is plenty. THz spectra for various configurations are shown in Fig. 3.3. We also tried a much shorter path length through a second 0.5 inch block (blue). Fig. 3.3 demonstrates the high sensitivity of the THz bandwidth on the Si path length.

The best achieved bandwidth for this system in practice, under nitrogen purge and with OAPs aligned, yielded a -20 dB point at 1.5 THz and a -30 dB point around 2.0 THz. We found we were able to take stable, reproducible TDTS data out to 1.8 THz (with at

least a hour of continuous Nitrogen purge). This was sufficient for measuring magnon absorption in α-$RuCl_3$.

3.4.1.3 THZ POLARIZATION

The linear THz polarization is determined by the orientation of the antenna dipole– the orientation is denoted by markings on the antenna modules themselves. Generally the emitter and receiver antennas are installed with polarizations aligned. Reflections off of the OAPs will introduce some ellipticity. Hence for for polarized measurements (in both THz systems), grid-patterned polyethylene THz polarizers (purchased from Tydex) are placed just before the cryostat window to clean up the linear polarization before the light hits the sample. To change the angle of the THz linear polarization with respect to the sample, one can either rotate the antennas (and realign) or rotate the sample.

3.4.1.4 OAP CONFIGURATIONS

Before discussing the details of OAP alignment in the Small THz system, we note that we use two different arrangements of 90^o OAPs for the two different spectrometers in our lab. Schematics of the OAP configurations used in both THz systems are shown in Fig. 3.4. The standard arrangement of OAPs used in TDTS is the "$8f$ confocal geometry". This is depicted in in Fig. 3.4, for $f_1 = f_2$. This geometry is useful because the THz beam generated in the emitter antenna contains broad range of frequencies, and these frequencies behave differently as they emerge from the Si-lens which couples them to free space [88]. Low frequency light diverges rapidly as it exits the lens, is collimated between the first two OAPs, and is focused by the third OAP. In the high frequency limit, light is much more collimated as it exits the lens, and is actually focused between the first two OAPs, and is collimated by the third OAP. These counteractive properties of the OAPS at the high and low frequency limit conveniently give rise to a frequency-independent spot at the center of the arrangement. Of course, longer wavelength light cannot be focused as tightly (diffraction limit) 2w= $(4\lambda/\pi)(F/D)$, where w is the beam waist, F is the focal length, and D is the diameter of the focusing optic. The collimated high-frequency light overlaps with the focused low frequency light, giving rise to a beam spot with containing a wide range of wavelengths. This property is illustrated nicely in Ref. [88].

This configuration generally works well, and is widely used, including in our own lab. However for the Small THz spectrometer, we employ a modified OAP configuration, illustrated in Fig. 3.4 (a). This differs from the standard $8f$ OAP configuration in that OAP 1 and OAP 2 (as well as OAP 3 and OAP 4) are mirror images of one another. Ray tracing analysis [93] shows that this modified geometry helps to compensate for aberrations that arise from the asymmetry of reflections off of multiple parabaloids and thereby achieve

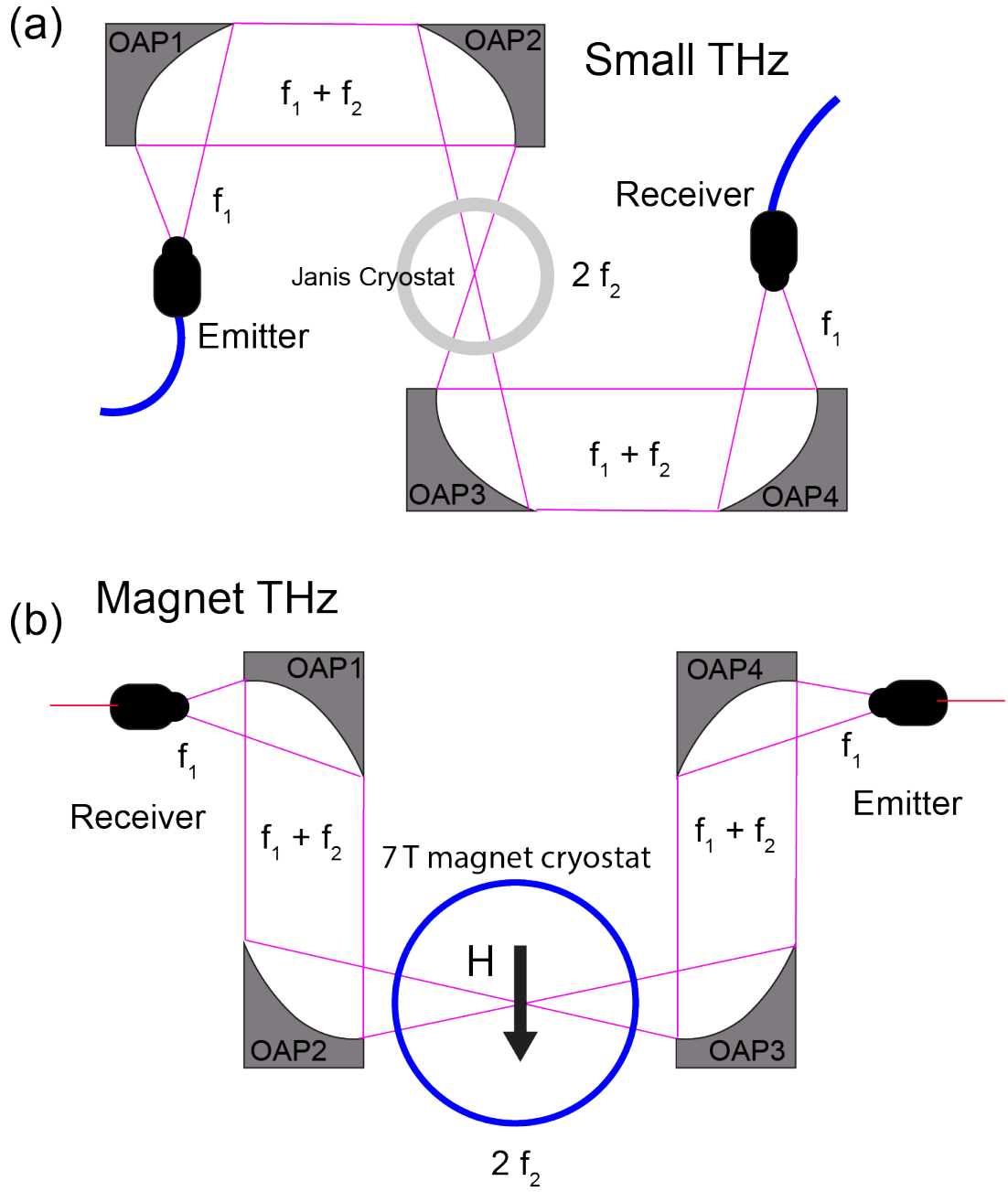

Figure 3.4: Comparison of OAP geometries for two TDTS systems a) Modified OAP geometry used in Small THz system, where OAP 1 and 2 (3 and 4) are mirror images of each other. Reflective focal lengths f_1 is 4 in, f_2 is 6 in. (b) Standard OAP geometry used in Magnet THz system with free space-coupled antennas and in-plane magnetic field an custom long f OAPs. f_1 is 6 in and f_2 is 12 in.

a tighter focal spot. The idea to use this geometry was originally shared with us by the Steve Dodge group at Simon Fraser University, and was later described in quantitative detail by Laurita et al. [93].

In our implementation, we used OAPs of two different focal lengths, $f_1 = 4$ inches and $f_2 = 6$ inches for the focusing mirrors. Typical knife edge tests used to determine spot size at optical wavelengths are not straightforward at these wavelengths due to diffraction effects that arise when aperture size is more comparable to the wavelength. Nonetheless our estimated spot size is around 4 mm.

3.4.1.5 OAP ALIGNMENT

The OAPs are mounted on sliding carriages which are attached and may slide on aluminum optical rails. All of this is commercially available Thorlabs. The optical rails are necessary to anchor the system and keep the OAPs mounts precisely 90 degrees from one another throughout the alignment. The optical rails are painstakingly aligned with each other and with the optical table. We opted of this system for ease of set-up and flexibility with alignment. OAPs are originally installed in the set-up based on measurements, and are later only slightly optimized during alignment. The OAP mounts have either two or three alignment knobs which adjust their angle; these knobs should never be too far from the neutral position. Ideally, with the fiber-coupled antennas you should only have to align the OAPs once.

As THz is invisible, the initial OAP alignment is done using with a pinhole, a green alignment laser, and a CCD camera. The general idea for this alignment procedure was shared with us by graduate student Michael Bartram of the Steve Dodge Lab at SFU. To implement this setup, the emitter antenna is removed from its mount, first noting the position of the Si lens along the optical rail. In place of the antenna we mount a 20 μm pinhole at the same position as the Si lens. Typically the pinhole is a 1-inch optic which will fit into the same mount used to hold the antenna. An alignment laser is mounted and aligned by a pair of planar silver mirrors straight into an adjustable neutral density (ND) filter and subsequently a focusing lens and the pinhole. The emerging beam will be diffracted through the pinhole and will diverge approaching OAP1, and be subsequently collimated and focused between OAPs 3 and 4, mimicking the path of the low-frequency THz light. The ND filter is in place to adjust the brightness of the beam in order to avoid over saturating the CCD camera. Depending on how tightly the beam is focused entering the pinhole, light may also be diffusely scattered around the entire pinhole/ mount set up, in which case it is useful to block this extraneous light using either cardboard or aluminum foil taped around the outer edges of the mount.

A Thorlabs CCD camera is mounted on a sliding carriage at the same height as the center of the OAPs, so that the camera may be translated back and forth along the rail

connecting the OAPs. During the alignment process the image of alignment beam can be monitored using the Thorlabs software on a near by computer.

It is best to perform this procedure with the lights off, as it will make it easier to see the diffraction rings in the THz focus. First check the light directly out of the pinhole– with the lights off it should be possible to see the diffraction rings with just a card and your eyes. The beam should exhibit symmetric concentric diffraction– if something is off you may need to realign the laser with respect to the lens and pinhole.

Next, check that the beam is collimated coming out of OAP1. Usually it is sufficient to use a card to view how the diffuse spot changes between OAP1 and OAP2. Adjust the distance between the pinhole and OAP1 until the spot does not change between the first two mirrors. This can be done by sliding the rail connecting OAP1 and OAP2 with respect to the pinhole position. Ensure that the spot hits the center of OAP2, and make slight adjustments to the OAP1 knobs if needed.

Now turn on the CCD which is mounted between OAPs 3 and 4. The laser focus can be found by sliding the camera slowly back and forth and watching the evolution of the beam spot which will appear to deform into and out of the central focus. Place the camera at the center of the focus and observe the diffraction rings– It may be useful to filter down the beam more at this point using the ND filter in order to see the fainter outer diffraction rings. The optimal, tightest focus can be found when the diffraction rings are symmetric.

The tightest focal spot can be achieved by optimizing the symmetry of the diffraction rings at the focus by adjusting OAP 2. This can be done by iterating between the coarse adjustment the OAP angle by rotating the whole mirror on its pedestal and the fine adjustment of the OAP tilt by adjusting the two knobs on the optical mount. Again, the two knobs on the optical mount should never have to be adjusted very far from neutral, if they do the there is something else wrong (a mismatch in the pinhole/antenna height with the center of the OAPs).

Once you start to see symmetry rings, use the measurement tool in the Thorlabs camera software to check the size of the central focus spot on the CCD. The focus should be around the same size as the pinhole aperture. A picture of an aligned focus on the Thorlabs camera software is shown in Fig. 3.5

To optimized the final focus on at the receiver antenna position remove the receiver and place the CCD camera in its place. As before, check the collimation between OAPs 3 and 4 with a card. Then adjust OAP 4 to symmetrize the diffraction rings on the CCD camera.

This alignment procedure offers a good starting point for getting a THz pulse on the receiver, but further optimizing with the antennas in place is usually required. Do this first without the cryostat in the beam path. Reinstall the antennas (the fiber coupling procedure is described in the previous section) and plug them into the relevant amplifiers

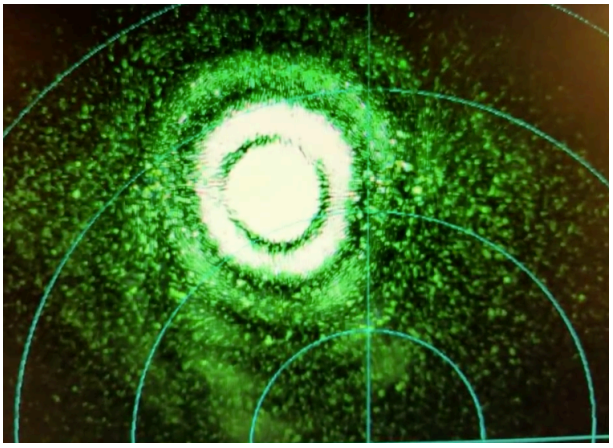

Figure 3.5: Focus of the alignment laser with OAPs adjusted as imaged on a Thorlabs CCD camera. Note the diffraction rings are roughly symmetrical.

and AC bias voltage. We the same techniques, and even the exact Clark rapid scan delay, described in [85]. First, use the stepper delay line find location of the THz pulse, which corresponds the temporal overlap of the generating laser pulse and the arrival of $\boldsymbol{E_{THz}}$ at the receiver, T_0. Once the delay line is set to T_0, the Clark rapid scan can be driven by a function generator oscillate at a few Hz. This will continuously scan the generator pulse arrival time back and forth across T_0. The time-dependent photocurrent is demodulated at the bias voltage frequency by the lock-in amplifier– for this diagnostic the lock-in time constant must be turned down to order of μs. The demodulated output of the lock-in is then plugged into an oscilloscope triggered at the frequency of the Clark rapid scan. The THz pulse should be visible for each half period of the rapid scan. This diagnostic is useful for tweaking the position of the emitter and receiver along the rail while optimizing the THz trace on the scope. Normally it may also help to tweak the tilt adjustment knobs on the mount for OAP 4 to center the THz pulse on the receiver antenna.

The final alignment for data taking involves installing the Janis instruments cryostat where the sample will nominally sit. The Janis cryostat is described in further detail in a following section. Install the cryostat into the system by lifting in and lowering it into the spectrometer– it rests snugly in the custom-machined aluminum plate which doubles as the top of the nitrogen box. For lifting the cryostat, it is helpful to have two people present, as it is somewhat heavy. It should be oriented such that the Kapton THz windows are in-line with the beam. The aluminum plate is affixed to the posts of the purge box by four bolts. These bolts can be loosened, giving the plate about half an inch of play. This alignment is admittedly crude but functional; to find the best cryostat position, maximize the THz photocurrent by pushing around the aluminum plate. The optimization can be

done based off of the rapid scan technique, but it is normally sufficient (and easier) to maximize the photocurrent value at the peak delay line position with the rapid scan off.

3.4.1.6 JANIS INSTRUMENTS CONTINUOUS-FLOW CRYOSTAT

Samples are mounted and cooled in a Janis Instruments continuous flow cryostat. While use of this cryostat is more labor-intensive and resource-intensive than other cryo-free systems in our lab, it does still work. The operating temperature range is room temperature down to 2 K. These 2 K measurements are achieved by filling the sample chamber with liquid Helium and pumping the chamber with a roughing pump to induce the superfluid transition. A brief, but more complete, description of how to bring the Janis cryostat down to low temperature is included in Appendix A.

The relevant upgrade made to this cryostat for the completion of this work is the installation of Kapton windows along one axis of the cryostat. Window material is an all-important consideration in THz measurements, as typically windows used for optical wavelengths (in this case quartz) will not work. Kapton windows are convenient because the transmission through them is around 70 percent. The cryostat has two sets of Kapton windows. The windows are laser cut from sheets purchased from McMaster-Carr. The outer windows are of a slightly thicker material and are simply epoxied to to aluminum flanges, which are then installed on the cryostat via a rubber o-ring seal. When the outer vacuum chamber of the cryostat is pumped down, these windows will curve inward– but rest assured they can withstand the pressures achieved by the turbo pumping station. The inner cold windows separate the outer vacuum chamber with the sample Helium space, and are made of thinner Kapton. These windows are sealed with an Indium seal: a aluminum flange compresses the Kapton window directly onto an Indium wire gasket on the cryostat. Should these windows need to be changed out, it will be necessary to replace both the Kapton and the Indium wire.

3.4.2 MAGNET THZ SYSTEM

The Magnet THz spectrometer is located in room 360. Alignment in this system follows the same basic principles used for the Small THz system, however it is more challenging due to the long focal length between OAPs 2 and 3, the small inner aperture of the magnet cryostat, and the additional degree of freedom afforded by the free-space coupled TeTechS antennas.

3.4.2.1 TETECHS ANTENNAS

The TeTechS antennas are GaAs and are excited by a 780 nm pulse from the second harmonic output of two-color Toptica fiber laser. The antenna is mounted in an optical cage module which includes XY micrometer stage and a focusing lens. The entire antenna module is installed on a magnetic optical mount which can be removed and replaced in a consistent position.

To begin, the laser should be directed straight onto the antenna substrate. To achieve this typically the antenna is removed and alignment tool consisting of two irises is mounted in place of the antenna. Once the laser is aligned to the two irises, remove the alignment tool and replace the antenna and check that the laser spot is focused by the lens and centered on the antenna substrate. The antenna photocurrent can be directly measured by applying a small DC bias voltage and reading out the current with a pre-amp and digital multimeter.

The antenna is a 100 x 100 μm region containing a central dipole with a 5 μm active area. This central dipole flanked by an patterned periodic structure meant to enhance the local electric field [94]. To optimize the photocurrent, adjust the position of the antenna with respect to the THz will only be generated when the laser spot hits the central dipole, but photocurrent can also be generated by the laser overlapping with the periodic structure or the bias contacts. As a result peaking up the photocurrent it is possible get trapped optimizing on a local maximum, rather than on the central dipole. One way to start off with this is to the antenna position first horizontally, then vertically to get a feel for the geometry of the antenna and where the local maxima are. The true maximum on the central dipole should feel very sharp. Optimize the photocurrent on both the emitter and receive antennas.

The OAP geometry for this system is illustrated in Fig. 3.4, largely because the distance from the outer window of the Magnet cryostat and the sample position is around 7 inches. Thus the distance between OAP2 and OAP3 must be greater than 14 inches, to accommodate additional space between the mirrors and the cryostat to mount polarizers. As there are no standard OAPs at this focal length, 12 inch focal length OAPs were custom manufactured by Thorlabs for this application. Due to the need for this long focal length, the diameter of OAPs 2 and 3 is only 2 inches.

OAPs are mounted on an optical rail system constructed around the magnet, all of which may be enclosed in a nitrogen box. The magnet cryostat itself is mounted to an aluminum plate which sits on a Teflon-lined tray so that it's position may be adjusted (i.e. pushed around). A photograph of the system in an operational state is included in Fig. 3.6.

For OAPs alignment, begin with the magnet out of the way. May be useful to start off with the alignment laser technique described in the previous section, but be aware that

Figure 3.6: The 7 T Magneto-THz spectrometer in our lab.

removing the antennas to. We found it necessary to peak-up THz pulse by optimizing the demodulated photocurrent read out from receiver antenna on the Zurich Instruments lock-in amplifier. Adjustments may be made by making small tweaks to the OAPs.

After the photocurrent in optimized, push the magnet back into place and adjust its position such that the transmission through the entire system is optimized. Adjustments to the magnet position are made using a system of four threaded rods which may be turned using ratchet wench, pushing against aluminum stand-offs mounted to the magnet plate. Once the optimal position is found, the magnet position may be fixed into place by tightening the threaded rods.

3.4.2.2 CRYO-FREE 7 T MAGNET

The magnet cryostat was custom-ordered for our lab and installed in 2017. It the coil is cooled by pulse tube cooler (PCT) and does not require any liquid cryogen. As superconducting magnet systems go, this one is relatively straightforward to use, and detailed instructions as well as log books are stored in the lab. The sample is mounted to a sample stick which is inserted from the top of the can into field. The additional cooling (below 2 K) to the sample is achieved by admitting Helium gas into the sample chamber and allowing it to condense.

Two sets of outer windows, fused silica for visible or infrared wavelengths, and Teflon windows for THz wavelengths– these outer windows are easily interchangeable. The center of the coil is accessed re-entrant tubes which are 1.5 inches in diameter, leading to the

sample chamber cold windows are 0.38 inch clear-view CVD diamond, 1 mm thick. These windows were chosen because they are transparent over a wide energy range, and are thick enough such that echo pulses from the windows are well-separated in time.

The maximum field attainable is 7 Tesla, the magnet is a split-coil solenoid, so there is optical access from along two orthogonal axes. The orientation of the field can be either parallel (Faraday geometry) or perpendicular (Voigt geometry) to the direction propagation of the THz beam. The field orientation is changed simply by rotating the entire cryostat. The measurements presented in this dissertation are all performed in the Voigt geometry.

Further information on the Magnet system can be found in Appendix B.

4

LOW ENERGY EXCITATIONS IN α-$RuCl_3$

Precise measurement of the magnetic fluctuation spectrum in α-$RuCl_3$, can shed light on the nature of the transition at H_c and the existence of, or proximity to, a KSL phase. In particular, it is important to understand which aspects of the Γ-point spectrum can be understood as conventional magnon or multi-magnon scattering as opposed to scattering resulting from exotic fractional excitations. As the relevant energy range for magnetic interactions in α-$RuCl_3$ is 0.4 to 7.0 meV, TDTS is uniquely suited for this problem. As an direct, internally-reference probe of the imaginary part of the AC magnetic susceptibility, $\chi''(\omega)$, TDTS spectra allow us to extract precise contributions of various spectral features to the total value of $\chi(0)$ and quantitatively evaluate how these features change approaching the disordered phase. In α-$RuCl_3$, below H_c we observe both well-defined, narrow magnon resonances and a continuum of absorption which we attribute largely to electric (as opposed to magnetic) dipole absorption.

Understanding the magnetic ground state and its excitations in the ordered phase is necessary for the understanding of the the sign and amplitude of the parameters in the magnetic Hamiltonian. The high energy resolution achieved by TDTS, as well as our ability to study the field-and polarization dependence of the spectra, enables precise comparison of the experimental magnon dispersion to linear spin wave theory (LSWT) calculations. Though careful fitting of the spectra, we can extract information about the relative strength of the various magnetic interactions as well as the multi-domain character of the crystals studied.

4.1 THZ SPECTROSCOPY OF MAGNETIC EXCITATIONS IN α-$RuCl_3$

4.1.1 SAMPLES AND X-RAY CHARACTERIZATION

The samples studied in this work were grown and provided by the groups of David Mandrus and Stephen Nagler at Oak Ridge National Laboratory (ORNL). Commercial $RuCl_3$ powder was purified to a mixture of the two polytypes of α-$RuCl_3$ and β-$RuCl_3$ and converted to a 99.9% phase-pure α-$RuCl_3$ by annealing at 500 C. Single crystals of α-

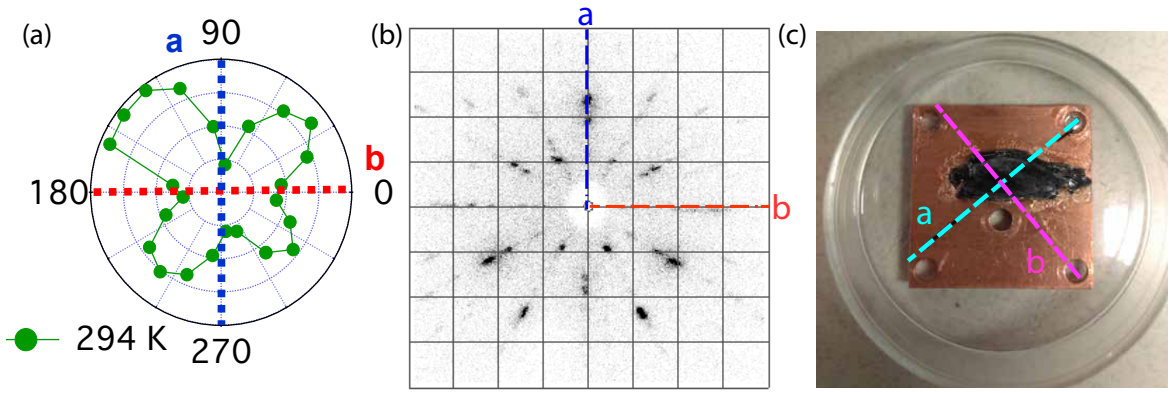

Figure 4.1: (a) Amplitude of the THz electric field transmitted through a α-RuCl$_3$ sample mounted between crossed polarizers, as a function of sample rotation angle at room temperature. The minima in transmission (nodes) denote the orientation of the principle optic axes a and b. (b) X-ray (Laue) diffraction pattern showing the reciprocal of the hexagonal lattice. The symmetry directions corresponding to the optic axes a and b are denoted by dashed lines. (c) The orientation of a and b on the sample studied in this work.

RuCl$_3$were grown using vapor transport at high temperature. The particular sample used for most of the THz data presented in this thesis (unless otherwise indicated) is roughly 5 mm x 8 mm in surface area and about 1.15 mm thick. The sample, which was colloquially dubbed the "Hope Diamond" Sample, is shown in Fig 4.1 (c) and exhibits a single magnetic phase transition at T$_N$ =7 K. For THz measurements, the Hope Diamond sample is mounted on a copper plate with a 5 mm aperture for transmission. This corresponds to roughly the size of the THz focus.

To guide the polarized TDTS measurements, the optical anisotropy of α-RuCl$_3$ samples was first characterized by measuring the amplitude of the transmitted THz electric field as a function of sample angle crossed linear polarizers. This measurement was achieved by mounting the sample on a motorized rotation stage positioned at THz focus. Two grid-patterned polyethylene polarizers were installed directly before and after the sample– the first polarizer is aligned with the polarization of THz light and the second polarizer is set at precisely 90 degrees. A typical room temperature scan of the amplitude of the transmitted THz electric field as a function of angle of sample rotation about the optic axis is shown in Fig. 4.1 (a). The relative size of electric field at each angle was determined by the integral of the absolute value of the transmitted THz pulse in the time domain. The nearly four-fold pattern, observed in all samples studied, indicates breaking of the C_3 symmetry of the perfect honeycomb lattice. Monoclinic symmetry allows different transmission coefficients for three mutually orthogonal principal axes, two of which lie in

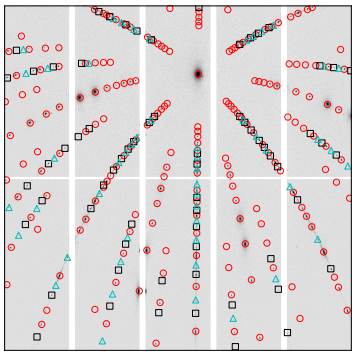

Figure 4.2: Example Laue diffraction patterned obtained from micro-diffraction imaging. This is a typical diffraction pattern obtained from the same sample studied by THz, illustrating the multi-domain character of this particular crystal. Red circles mark diffraction peaks successfully indexed with the dominant monoclinic domain, while black squares and cyan triangles mark peak that are unique to the monoclinic domains rotated by $2\pi/3$ and $4\pi/3$, respectively, about the sample normal with respect to the dominant domain.

the ab plane and would result in optical birefringence as measured in Fig. 4.1. In contrast, a C_3 symmetric sample would produce an isotropic polar pattern. This indicates that the samples samples studied in this work exhibit symmetry consistent with $\sim 0.2\%$ elongation of one of the Ru-Ru bonds and a monoclinic $C2/m$ space group [54, 56]. This elongation along the direction of one the bonds defines the $\boldsymbol{b}$ axis of the monoclinic structure.

The absence of true zero nodes in the polar pattern in Fig. 4.1 (a) along the optic axes indicates that the local $C2/m$ symmetry is broken globally by the presence domains of the three equivalent orientations of monoclinic distortion, which are rotated 120° from one another. For instance, single domain $C2/m$ crystal would exhibit zero transmission for THz fields polarized parallel to the $\boldsymbol{a}$ or $\boldsymbol{b}$ axes, which is not seen in any of the samples we have studied. On the other hand, in a sample containing equal populations of three domains the optical anisotropy of each would be effectively canceled and the THz transmission between crossed polarizers would vanish for all angles. What we observe instead is the intermediate case, where unequal domain population gives rise to weak residual anisotropy. Because of the low effective symmetry, the directions of minimum transmission in Fig. 1(a) do not coincide with the monoclinic axes of a single domain, although they will be close to those of a dominant domain.

To confirm the room temperature structure and the presence of multiple domains in this crystal, we performed scanning X-ray micro-Laue diffraction measurements [95]. Using the Advanced Light Source beamline 12.3.2, a full Laue (i.e. polychromatic) diffraction pattern was collected at spots of 2 μm across a 6 mm × 5 mm region of the sample. The

peaks were indexed using the lattice parameters in the $C2/m$ space group give in Ref. [54]. A representative Laue pattern from a single point is shown in Fig. 4.2. Three sets of diffraction peaks corresponding to the monoclinic structural twins, rotated at $2\pi/3$ from one another, are indexed. The diffraction peaks corresponding to the dominant domain are indicated by red circles, while the two sub-dominant twins, appearing at about 10% of the integrated intensity of the dominant domain, are black squares, and cyan triangles. Three monoclinic domains are indexed across a large region of the sample with spatially varying populations. The presence of all three domains in a single Laue point stacking orientation varies a a function of depth as well as across the ab-plane. A description of the fitting and indexing procedure for the Laue peaks for this particular α-$RuCl_3$ sample is presented in further detail in Ref. [92].

This multi-domain character, as we will show, is essential to understanding the THz absorption spectra in the zigzag state as a function of magnetic field. In this study, we reference our THz polarization and external magnetic field $\boldsymbol{H}$ to the two directions of minimum transmission, which we label as $\boldsymbol{a'}$ and $\boldsymbol{b'}$ to distinguish them from the monoclinic axes of a single domain. The polarization of the THz electric field, $\boldsymbol{E_{THz}}$ is by definition perpendicular to THz magnetic field $\boldsymbol{B_{THz}}$, which couples to magnetic dipole absorption in the material. We measure the absorption coefficient $\alpha(\omega)$ with the THz probe field in the honeycomb plane, $\boldsymbol{B_{THz}}$, oriented parallel to $\boldsymbol{a'}$ and $\boldsymbol{b'}$, and in both cases we compare measurements with in-plane $\boldsymbol{H}$ parallel and perpendicular to $\boldsymbol{B_{THz}}$.

Determination of the index of refraction, n, from THz transmission does (discussed in the following section) indicated a shift in n occurring at 150 K. Although we were not able to confirm if this corresponds to a structural phase transition, we do note that anisotropy TDTS spectra (Fig. 4.3) indicate that C_3 symmetry remains broken at low temperature.

4.1.2 AFM RESONANCE VS. THZ CONTINUUM

With the principle optic axes of the sample defined, we may carry out polarized TDTS measurements to extract the full complex transmission (and absorption) spectra along each principle axis.

As discussed in Chapter 2, our TDTS measurements were motivated by the observation by INS of a broad-band scattering continuum centered at the Γ-Point ($\boldsymbol{Q} = 0$) in momentum space. This was put forward as a possible signature of fractional excitations in the KSL state of this compound. For investigating this feature, TDTS is an ideal complementary probe to INS. TDTS precisely probes $\boldsymbol{Q} = 0$ and polarized, high-energy and -field resolution measurements are relatively straightforward (compared to INS) to perform.

TDTS is based on measuring the transmission coefficient, $T(\omega)$, of picosecond timescale electromagnetic pulses. In the weak absorption limit appropriate to a large gap Mott insulator such as α-$RuCl_3$, time-domain THz transmission will consist of a sequence of transmitted pulses in which the first traverses the sample once and subsequent "echo" pulses undergo multiple reflections and traversals. As described in detail in Chapter 2, the time-domain data is converted to the frequency domain by an FFT data processing scheme, and normalized by a spectrum taken of an empty sample mount aperture to obtain an exact transmission spectrum.

For the measurements reported in this work, the sample is sufficiently thick and the round trip time sufficiently long that the echoes are well-separated in time. In this regime, we can restrict our time delay window to the first pulse. The transmission coefficient for a single pass through the sample is given by

$$T(\omega) = [4\tilde{n}/(\tilde{n}+1)^2]\exp\{[ik_0(\tilde{n}-1)d]\}, \tag{4.1}$$

where $\tilde{n} = n + i\kappa$ is the complex index of refraction, k_0 is the free space wavevector, and d is the sample thickness. In α-$RuCl_3$ at THz frequencies we have $n \gg \kappa$, in which case,

$$|T(\omega)| \cong [4n/(n+1)^2]\exp\{[-\alpha(\omega)d]\}, \tag{4.2}$$

where the absorption coefficient $\alpha(\omega)$ is given by $\omega\kappa(\omega)/c$.

The TDTS spectra measured for α-$RuCl_3$ below T_N zero applied field are presented in Fig. 4.3 These spectra are characterized by two salient features: (1) a sharp resonance peak at 0.6 THz or 2.56 meV, and (2) This peak is superposed on a broad continuum of absorption with a low-energy cut-off. This is illustrated by three separate measurements in Fig 4.3. In Fig. 4.3 (a) we plot the transmission spectrum, $1 - |T(\omega)|$ for THz electric field polarized parallel to the **a** (blue) and **b** axes as measured on the 1.15 mm thick "Hope Diamond" sample in the Small THz system. In panel (b), we repeat the measurement on the same sample in the Magneto-THz spectrometer, and convert the transmission to the corresponding dimensionless absorption $\alpha(\omega)d$, where d is the sample thickness.

The spectra for the two orthogonal polarizations are distinctly different, showing that the breaking of C_3 observed at room temperature persists to low T. These two panels illustrate that while there are some some differences in the spectra from either system arising from differences in stability out to higher frequencies, THz spot size, data processing, and alignment, the essential features are robust in both measurements.

Panel (c) is a plot of the THz absorption spectra for a second thinner sample ("Sample 2") around 810 μm in thickness, measured in the Small THz system. The frequency-domain oscillations present in this data are the result of the inclusion of the secondary echo pulse in the FFT. This data is shown to first of all illustrate that while there are certainly

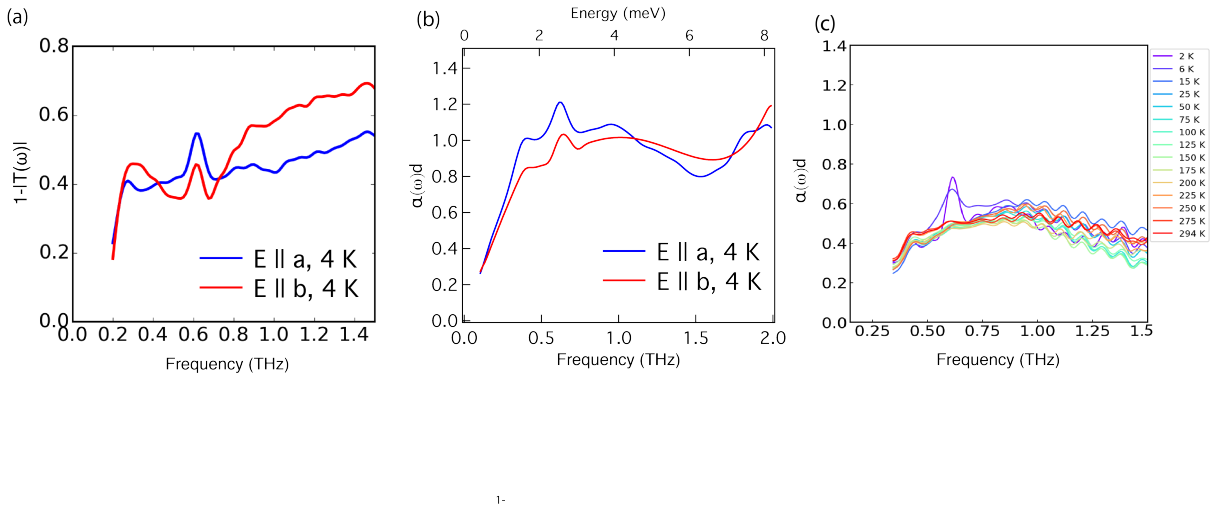

Figure 4.3: THz spectrum for a variety of different configurations in α-$RuCl_3$ (a) The raw spectrum, $|1 - T(\omega)|$ for THz electric field polarized parallel to the **a** (blue) and **b** axes taken in the small THz spectrometer system on the Hope Diamond sample (b) The THz absorption spectrum, converted from transmission by Eq. 4.2 taken at 4 K in the Magneto-THz system with closed cycle cryostat, on the Hope Diamond sample (c) THz absorption spectrum taken at an arbitrary polarization angle on a second, thinner sample, in the small THz spectrometer from 2 K to 294 K.

sample-to-sample variation in α-$RuCl_3$ crystals, the same basic features emerge. As will be discussed later, the broadband continuum is only weakly temperature dependent.

The conversion from transmission to absorption spectra shown in Fig. 4.3 requires knowledge of the real part of the index of refraction, n. The index is measured by considering measured the time delay between the initial transmitted THz pulse and a subsequent "echo" pulse. The initial pulse makes a single pass through the sample, while the echo pulse undergoes two internal reflections and makes three passes through the sample. The delay time between the initial pulse and the first echo is given by $t_{rt} = 2nd/c$, where n is the index of refraction, d is the sample thickness, and c is the speed of light. In determining the index, we used "Sample 2" which has a relatively uniform thickness of micrometer to be 0.810±0.015 mm (measured by digital micrometer) across the 3 mm region probed by THz.

Fig. 4.4 shows initial and echo THz pulses at 4 K and 295 K sampled at time delay intervals $\Delta t = 0.667$ picoseconds. At 4 K, the delay time between the peak of the initial and echo pulse is 13.40 ps, rounding to four significant digits, which corresponds to $n = 2.48$. The comparison of the two pulse sequences in Fig. 4.4 (a) shows that n depends weakly on T. As shown in Fig. 4.4 (b), n is T independent at low T but increases linearly with T starting at 150 K, reaching 2.53 at 294 K. The measurement was taken upon warming the sample, and the observed jump in the index around 150 K is consistent with the structural phase transition reported in Ref. [58]. For the analysis presented in this thesis, the rounded value $n = 2.5$ was used to evaluate optical response functions at at all temperatures.

We will discuss first the temperature and field dependence of resonance peak, and then continuum feature in the following sections.

4.1.3 MAGNON RESONANCE AT 0.62 THZ: THE Ω_1 MODE

The temperature dependence of resonance the sharp resonance peak in zero applied magnetic field is illustrated in Fig. 4.5. Panel (a) shows the the results of subtracting the THz transient measured at 15 K from those measured below the Néel temperature, for $\boldsymbol{B}_{Thz} \perp \boldsymbol{a'}$. The inset to panel (a) compares pulses transmitted through the sample at 2 K and 15 K. The time-domain oscillations which appear with decreasing temperature are well described by an exponentially damped sinusoid, $A\exp\{(-\Gamma t)\}\sin(\omega_R t)$ where A, Γ, and ω_R are fit parameters. One such fit (dashed line) is shown in comparison to the raw data (solid lines) for 6 K. From the fit parameters, we extract the temperature dependence of the amplitude and resonant frequency of the absorption peak as the sample is warmed through T_N as shown in Fig. 4.5 (b).

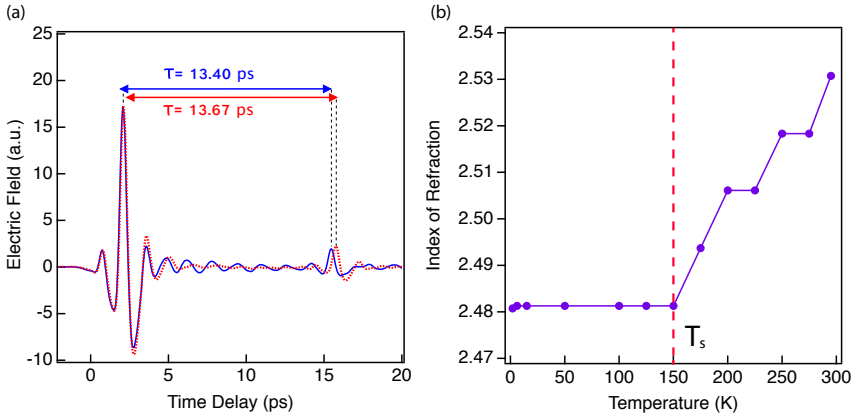

Figure 4.4: (a) Time-domain transmission of the THz electric field through a 1.15 mm thick sample of α-RuCl$_3$. The initial pulse corresponds to a single pass through the sample, the small around 13 ps is the first echo. The blue pulse is taken at 4 K and the red pulse is taken at room temperature. The oscillations in the 4 K correspond to the magnon frequency at 0.62 THz. (b) The index n calculated from the initial and echo pulse spacing, as a function of temperature.

Another way to extract the temperature dependence of this peak is to reference spectra taken below T$_N$ to spectra in the disordered phase. Such referenced frequency domain absorption data, $\Delta\alpha(\omega)d$, is shown in Fig. 4.5 (c), which shows the spectrum in the temperature range of 4 K to 8 K with the 10 K spectra subtracted out. Note that for the 8 K - 10 K spectrum the resonance peak is no longer visible. Fig (d) shows differential spectra with 60 K used as a reference frequency. These plots illustrate two key features. First that the resonance is completely gone at 10 K, and therefore 10 K is a suitable reference temperature for studying the ordered phase. Second, that the continuum feature is largely subtracted out, and does not exhibit a clear temperature dependence for this sample, as will be discussed further in the following section.

As the 0.62 THz mode appears at T_N, it is natural to associate it with resonant magnetic-dipole excitation of a $\mathbf{Q} = 0$ magnon [96, 97]. Approaching T_N, we observe a small redshift in the resonant frequency, as observed in classical collinear antiferromagnets CoCl$_2$ [98]. Magnons will appear at a nonzero energy whenever $SU(2)$ spin rotation symmetry is broken by spin-orbit interactions, as are clearly present in α-RuCl$_3$. However, as translational symmetry also changes at T_N, with the onset of zig-zag order, it is also conceivable that the resonance results from folding to zero wavevector of an acoustic phonon.

To test whether the resonance is indeed a magnon, we performed TDTS as function of in-plane magnetic field from 0 to 7 Tesla, obtaining the absorption spectra shown in Fig. 4.6. The resonant mode clearly shifts systematically to lower frequency with increasing

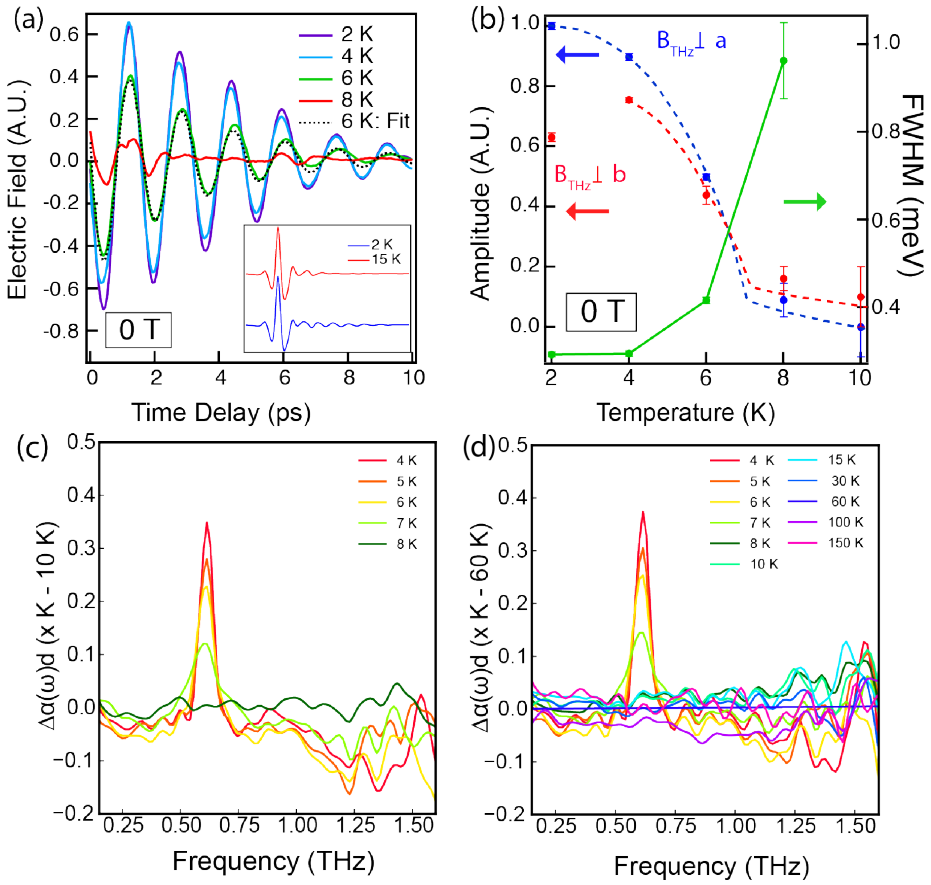

Figure 4.5: Temperature dependence of the magnon at 0.62 THz (a) Coherent magnon emission measured in the time domain at 2 K, 4 K, 6 K, and 8 K on an expanded vertical scale. Inset: Time trace of transmitted THz $\boldsymbol{E}$ field at 2 K (blue) and 15 K (red). The 2 K pulse shows coherent magnon radiation while the 15 K pulse does not. (b) Resonance amplitude (left-hand scale) with $\boldsymbol{B}_{THz} \perp \boldsymbol{a'}$ (blue) and $\boldsymbol{B}_{THz} \perp \boldsymbol{b'}$ (red) and full-width half maximum (FWHM) along $\boldsymbol{B}_{THz} \perp \boldsymbol{a'}$ (right-hand scale) as a function of temperature. Dashed lines are a guide to the eye. (c) Frequency-domain temperature evolution. Differential spectra showing the 0.6 THz mode in the $\boldsymbol{B}_{THz} \perp \boldsymbol{a'}$ configuration for 4 K to 8 K with the 10 K spectra subtracted out. Note that for the 8 K - 10 K spectrum the resonance peak is no longer visible. (d) Differential THz spectra in the same configuration referenced to the 60 K spectrum.

H. As the periodicity of the antiferromagnetic order does not change with field [61], this observation demonstrates that the mode is not a zone-folded phonon. For labeling purposes later in this chapter, we will denote this resonance as the "Ω_1" magnon.

Assuming that photons couple to the magnetic excitations through the magnetic dipole interaction, we can evaluate the imaginary part of the dynamic magnetic susceptibility at zero wavevector, $\chi''(\omega)$, associated with the peak. To extract this component we subtract the zero-field spectrum from those measured with $\mathbf{H} \neq 0$; the resulting difference spectra are shown in Fig. 4.6 (b). The strength of the absorption thereby is directly related to $\chi''(\omega)$ via the relation,

$$\alpha(\omega)d = \frac{\omega n d}{2c}\chi''(\omega) = \frac{\omega t_{rt}}{4}\chi''(\omega) \tag{4.3}$$

Note that the absolute, as opposed to relative, values of $\chi''(\omega)$ are obtained directly from fundamental observables: optical density, αd, and the pulse roundtrip time, t_{rt}.

To obtain the $\chi(0)$ from the difference spectra in Fig. 4.6 (b), we perform fits to a Lorentzian lineshape, that is,

$$\Delta\alpha(\omega, H)d = \frac{T_{rt}S(H)\omega^2\Gamma(H)}{4((\omega^2-\omega(H)^2)^2+\omega^2\Gamma(H)^2)} - \frac{T_{rt}S_0\omega^2\Gamma_0}{4((\omega^2-\omega_{R0}^2)^2+\omega^2\Gamma_0^2)} + c\omega, \tag{4.4}$$

where $\omega_R(H)$ and $\Gamma(H)$ are now field-dependent and $S(H)$ parameterizes the the overall amplitude. S_0, Γ_0, and ω_{R0} are the fit parameters for the 0 T spectrum, T_{rt} is the pulse round trip time, and c is the slope of a linear in ω background. The fits (dashed lines) and data (solid lines) are shown in 4.6 (b). Note that when we collect the absorption difference spectra, we can scan longer in the time domain to increase the frequency resolution, as Fabry-Perot oscillations that result from including the first echo are greatly reduced in the difference spectra. However, for the absorption curves plotted 4.6 (a), we used time-windowing to remove the echo pulse. As a result, the magnon resonance appears slightly broadened in 4.6 (a).

The evolution of the resonant frequency and inverse quality factor, Γ/ω_R with applied field $\boldsymbol{H}$, as obtained from the lineshape analysis are shown in Fig. 4.6 (c). The width of the resonance measured at zero applied field, $\approx$ 300 μeV, is at least 5 times smaller than the $\boldsymbol{q}_{ab} \approx 0$ peak observed by the original INS measurements [7, 99]. Relatively recent field-dependent INS studies achieved higher energy resolution (sub-meV) by using a enormous 2 g crystal [5].

A striking characteristic of this data is that although the center frequency of the magnon, $\omega_R(H)$, decreases with increasing $\boldsymbol{H}$, the resonance remains remains a well-defined, underdamped mode despite the loss of long-range magnetic order that occurs at a critical field, $H_c \approx 7.5$ Tesla.

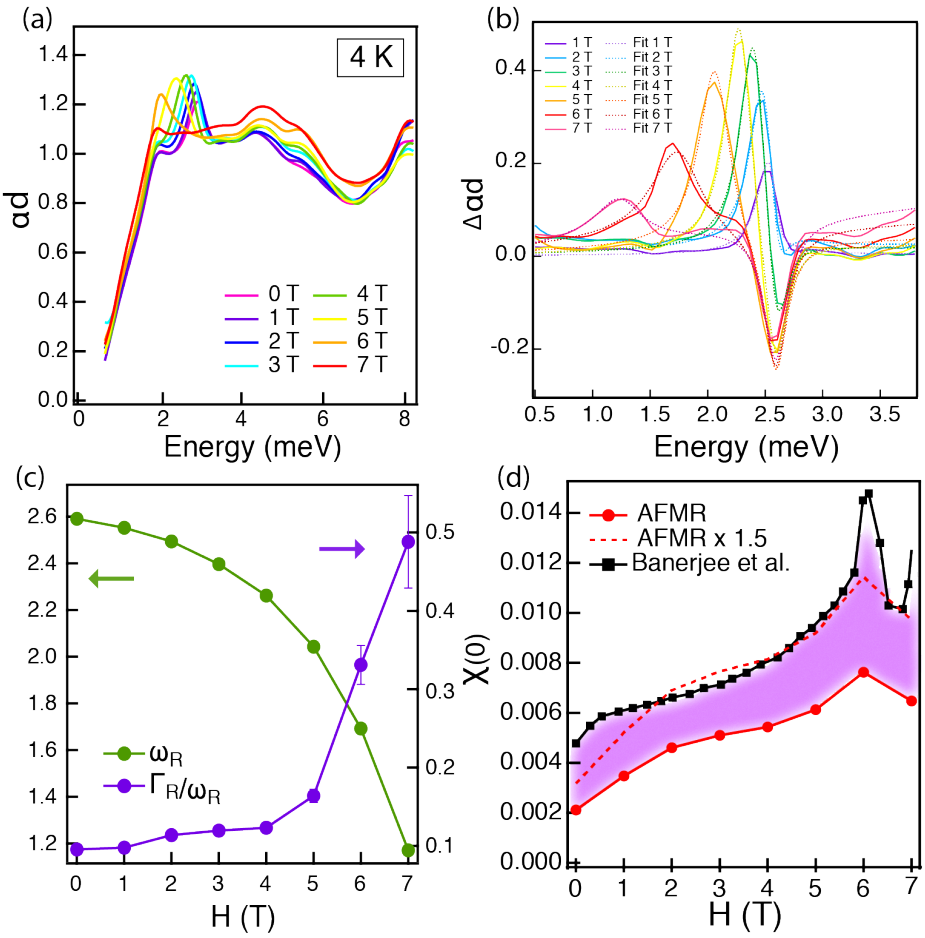

Figure 4.6: Field dependence of the 0.62 THz magnon, Ω_1 (a) THz absorption spectra as a function of field (b) Absorption spectra with the zero-field spectrum subtracted (solid lines) with Lorentzian fits (dashed lines). (c) dependence of the magnon energy (left-hand axis) and inverse quality factor, Γ_R/ω_R (right-hand axis). (d) Solid black squares and red circles show the static magnetic susceptibility, $\chi(0)$, and the contribution to $\chi(0)$ from the $\boldsymbol{Q} = 0$ magnon, respectively, as a function of magnetic field. The shaded region indicates the maximum contribution form a magnetic excitation continuum.

In the scenario where the system approaches at KSL at H_c, we expect that the spectral weight of the magnon, an excitation associated with the ordered state, will be transferred into the broadband magnetic continuum associated with the KSL.

THz spectroscopy allows us to quantify this behavior by providing an auto-calibrated measurement of $\chi''(\omega)$ at zero wavevector, from which we can extract the dc magnetic susceptibility contributed solely from the magnon. This is done using a thermodynamic sum rule, derived from the Kramers-Kronig relation, which relates $\chi''(\omega)$ to the dc magnetic susceptibility, $\chi(0)$,

$$\chi(0) = \frac{2}{\pi}\int_0^\infty \frac{\chi''(\omega')}{\omega'}d\omega'. \tag{4.5}$$

While Eq. 4.5 is valid in general, the contribution to the dc susceptibility of a mode described by the Lorentzian lineshape of Eq. 2 is simply given by $\chi(0) = S/\omega_R^2$.

This conversion of the magnon spectral weight to $\chi(0)$ at each value of $\boldsymbol{H}$ allows us to address the important question of the existence and strength of a continuum of magnetic excitations at $\mathbf{q} = 0$, in comparison to the well-defined magnon mode.

In Fig. 4.6 (d), we compare the extracted $\chi(0)$ associated with the magnon resonance, $S(H)/\omega_R^2(H)$, with low-frequency susceptometry measurements of $\chi(0, H)$ taken at Oak Ridge National Lab [7]. The measurements $\chi(0, H)$ were taken with the applied field parallel to $\boldsymbol{a'}$ and were reported in CGS units of emu/cm^3. The units of $\chi''(\omega)$ reported by THz spectroscopy are naturally dimensionless SI, as is plotted in 4.6 (d). To convert from CGS to SI for direct comparison, we use the molar volume of α-$RuCl_3$ 54.6 mol/cm^3 and a factor of 4π between the two systems of units.

Both the spin wave contribution and the total $\chi(0, H)$ grow with increasing field, maintaining a fixed proportionality for $H < 6$ Tesla; this is highlighted by the dashed line, which shows $S(H)/\omega_R^2(H)$ scaled by a factor of 1.5. Note that even as the amplitude of magnon peak decreases with H, the magnon contribution to $\chi(0)$ grows, as the peak also shifts to lower energy and the sum rule is weighted by $1/\omega$ 4.5.

The shaded region between the two curves corresponds the dc susceptibility not accounted for by the magnon absorption. This analysis shows that the allowed total allowed $\chi(0, H)$ has a large contribution from the Ω_1 mode. In turn, the contribution to the dc susceptibility from a magnetic continuum is comparable in size to the contribution of the $q = 0$ spin wave, even approaching the critical magnetic field.

4.1.4 THZ CONTINUUM

Finally, we discuss the broad-band component of the THz absorption that is evident in Fig. 4.6 (a). First, the thermodynamic sum rule argument described above rules out

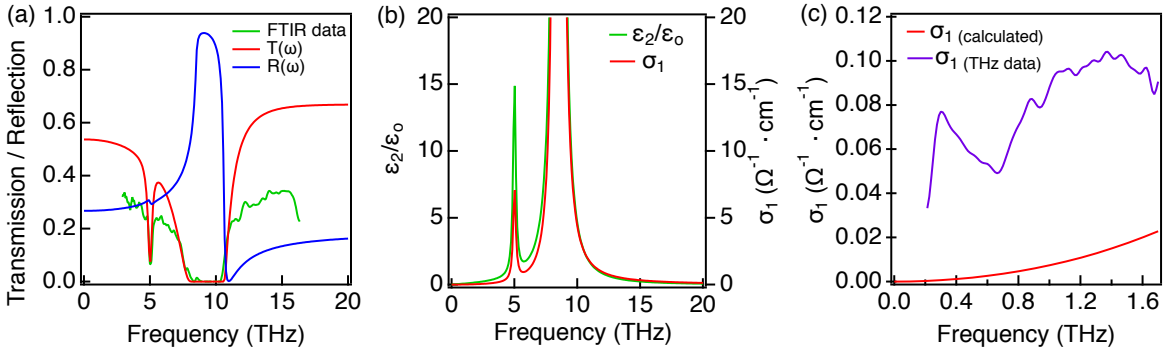

Figure 4.7: (a) FTIR transmission data (green) compared with theoretical transmission (red) and reflection (blue) as modeled by Eq. S1. (b) The dimensionless imaginary dielectric constant, ϵ_2/ϵ_0 (green) as extracted from our model and the associated optical conductivity, σ_1 (red). (c) Measured THz conductivity at 294 K (purple) compared with the calculated phonon contribution to the optical conductivity (red).

the possibility that the large observed continuum observed by THz spectroscopy arises entirely from magnetic-dipole absorption.

To show this, consider converting the entire $\alpha(\omega)$ to $\chi''(\omega)$ using Eq. 1, and then integrating $\chi''(\omega)/\omega$ with respect to ω to obtain a value for $\chi(0)$. As is already evident from comparison of the spectral weight of the resonant and broadband contributions to αd, the $\chi(0)$ that emerges from this calculation is far larger, by ≈ 30 times, than the measured value of 0.02 emu/mole (~ 0.005 in SI units) [47]. Therefore the dominant contribution to the broadband absorption must originate from electric, rather than magnetic-dipole coupling, as expressed for example in terms of an optical conductivity.

One possibility is that the THz continuum could arise from the low-frequency tail of an optically active phonon. To test this hypothesis, we performed Fourier transform infrared spectroscopy (FTIR) at the ALS Beamline 5.4, at room temperature on a sample with dimensions 6 mm $\times$ 1 cm and order of 100 μm thickness.

The sample was mounted on a 5 mm aperture and the transmission was measured at room temperature for unpolarized infrared (IR) radiation with energy range of $\sim$100 - 10,000 cm^{-1} or $\sim$ 3 - 330 THz. The FTIR data is shown in Fig. 4.6. The main features are an absorption resonance at 5 THz and a (Restrahl) band of zero transmission from 8-10 THz, which results from near unity reflectivity in this range. This spectrum is consistent with earlier studies of reflectivity of α-RuCl$_3$ [51], and with the more recent detailed optical studies presented in Refs.[100, 101].

To determine the contribution of the two low-energy phonons to the transmission spectrum in the THz regime, we fit the FTIR data to a Lorentzian fitting function of the form,

$$\epsilon(\nu) = \epsilon_\infty + \frac{\Omega_1^2 \epsilon_0}{\nu_1^2 - \nu^2 - i\nu\gamma_1} + \frac{\Omega_2^2 \epsilon_0}{\nu_2^2 - \nu^2 - i\nu\gamma_2}. \tag{4.6}$$

The factors Ω_i, ν_i, and γ_i, where $i = 1,2$ are the spectral weight, resonant frequency, and damping parameters, respectively for the two phonon modes. Fig. 4.7 (a) shows the transmission, $T(\omega)$, and reflectivity, $R(\omega)$ calculated using parameters $\Omega_1 = 16$ THz, $\nu_1 = 8.5$ THz, and $\gamma_1 = 12$ GHz to fit the Restrahl feature, and $\Omega_2 = 1.25$ THz, $\nu_1 = 5.0$ THz, and $\gamma_1 = 0.25$ THz to describe the absorption peak. The spectral weight of the phonon that produces the Restrahl feature is a factor of order 10^2 larger than that of the lower energy peak. The steepness, bandwidth and near null transmission of the Restrahl band constrain its spectral weight parameter within an error range of about 10%.

By fitting the phonon features in the transmission spectra, we can estimate the optical conductivity at the lower end of our spectral range, 0.2 THz, associated with the Lorentzian tail of the optical phonon absorption. Fig. 4.6 (b) shows the calculated ϵ_2/ϵ_0 on the left hand scale and the corresponding σ_1 on an expanded right hand scale. With the spectral weight and damping parameters quoted above, the imaginary part of the dimensionless dielectric function at 0.2 THz is $\epsilon_2/\epsilon_0 = 2 \times 10^{-3}$. This value for the imaginary part of the dielectric function corresponds to $\sigma_1 = 2 \times 10^{-4}\ \Omega^{-1} \cdot \text{cm}^{-1}$, which is approximately two orders of magnitude smaller than the optical conductivity in the THz regime, as illustrated in 4.6 (c).

Additionally, we note that fact that the THz absorption depends only weakly on T, as illustrated in Fig. 4.8 (a). This argues against effects such as multi-phonon absorption or defect-activated conductivity, which are typically highly dependent on T, as illustrated by references [102] and [103]. The THz spectra of the sample used in this study do not show clear hysteresis in the THz absorption coefficient related to a structural phase transition in the temperature range of 60 to 150 K, as was reported by optical measurements of samples grown by a different group in Ref. [76].

Thus, we conclude that the dominant contribution to the broadband absorption must originate from electric, rather than magnetic-dipole coupling, as expressed for example in terms of an optical conductivity.

To quantify this, we convert the THz absorption coefficient to optical conductivity, $\sigma_1(\omega)$, using the relation $\sigma_1(\omega) = 2nZ_0\alpha(\omega)$, where $Z_0 = 377\ \Omega^{-1}$ is the admittance of free space.

Fig. 4.8 (a) shows the resulting spectrum $\sigma_1(\omega)$ at temperatures from 2 K to room temperature. We note again the lack of temperature dependence– in particular the drop-off in $\sigma_1(\omega)$ below ≈ 1 meV remains well-defined even at high temperatures where $k_B T \gg$

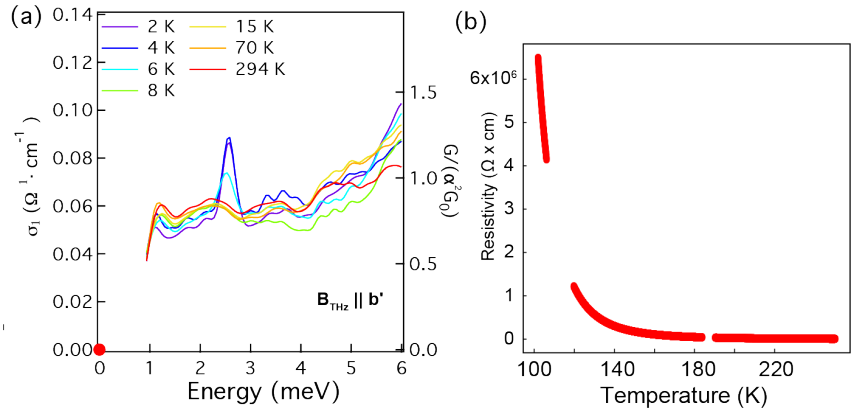

Figure 4.8: (a) Absorption spectra interpreted as optical conductivity, with $\boldsymbol{B_{THz}}$ parallel to $\boldsymbol{a'}$. (b) DC conductivity at a function of temperature measured by transport.

1 meV. The linear in ω cut-off below 1 meV is a reproducible feature seen in all spectra. Further evidence for the decrease in $\sigma_1(\omega)$ below 1 meV is that the DC conductivity, $\sigma(0)$, plotted as the red dot at zero frequency is indistinguishable from the origin, even at room temperature, where $\sigma(0) \sim 3 \times 10^{-4}\ \Omega^{-1}\ \mathrm{cm}^{-1}$. The DC conductivity, shown in 4.8 (b) was measured at Stanford University by a two-terminal measurement on an exfoliated flake. Due to the highly insulating nature of α-$RuCl_3$ measurement is only possible down to 100 K, where $\rho \sim 6.5 \times 10^6\ \Omega\cdot$ cm.

The large conductivity continuum is unexpected, as the 0.3-8.3 meV energy scale is well below the range of expected optical transitions. Excitations across the Mott gap onset at 200 meV ($\sim$ 50 THz) [43] and the dominant dipole-active optic phonon resonance is found at $\sim$ 35 meV ($\sim$ 8.5 THz). Lorentzian fits to this phonon mode yield $\sigma_1(\omega)$ that is well below the measured value near 1 meV. Although non-Lorentzian lineshapes are found in many wide-gap insulators, the signatures of these acoustic-phonon assisted processes are strong temperature and featureless power-law frequency dependences [102], both of which are inconsistent with the spectra.

Given the structure in the spectra on the meV energy scale, we suggested that the THz absorption is related in some way to the spin-degree of freedom. We note that features of the THz spectra, particularly the linear in ω low-energy cut-off, closely resemble the dynamical spin structure factor predicted for the Kitaev-Heisenberg Hamiltonian [73]. Intrinsic mechanisms by which spin fluctuations in frustrated magnets acquire electric-dipole activity were described in Refs. [104] and [105]. The predicted optical conductance per atomic layer is either $\sim (e^2/h)(t/U)^3$ if the lattice is fixed, and $\sim (e^2/h)(t/U)^2$ if magnetoelastic coupling is considered (t and U are hopping and Coulomb energies, respectively). Converting the spectra shown in Fig. 4.8 (a) to conductance per Ru layer

yields an optical conductance of $\sim 10^{-4}(e^2/h)$ and of the same order as found in the Kagome compound Herbertsmithite [106].

This observation a σ_1 continuum motivated theoretical works in Refs. [107, 108]. These authors considered a mechanism for sub-gap conductivity in the pure Kitaev model, whereby a finite polarization operator arises from nearest-neighbor virtual hopping. This results in an electric dipole moment which may couple the the THz field. This mechanism was further extended d^5 Mott insulators in [108], offering a theoretical framework for the description magneto-electric effects in Kitaev materials.

4.2 SELECTION RULES, Q-FLOP, AND LINEAR SPIN WAVE THEORY

In the preceding section, we discussed the discovery of the well-defined Ω_1 magnon absorption at 0.62 THz and studied the evolution of this mode with temperature and field. Through the application of the thermodynamic sum rule for magnetic susceptibility, we placed bounds on the strength of a magnetic approaching the phase transition to a quantum disordered state at 7.5 T. The broadband continuum of absorption, as measured by THz we find must largely result from electric dipole absorption, rather than magnetic dipole. However, in the all of the measurements discussed so far were taken in only one configuration, with the probe field $\boldsymbol{B_{THz}}||\boldsymbol{H}$.

In this section, we extend polarized TDTS measurements to a broader phase space of THz polarization and external field orientation. These measurements reveal two sharp magnon resonances, as well as two broader peaks at higher energy which may be associated with two-magnon excitations. We find the resulting spectra can be accurately modeled by a linear spin wave theory (LSWT), from which extract information about the relative strength of the magnetic interactions in the ordered phase can be extracted. Below T_N, we find that LSWT can account for all the essential features of the spectra when a C_3-breaking distortion of the honeycomb lattice and the presence of structural domains are taken into account.

4.2.1 POLARIZED TDTS IN FOUR CONFIGURATIONS

Polarized TDTS measurements were taken in four configurations in reference to the principle optic axes, as defined in Fig. 4.1. In total, we observe four resonances whose frequency and amplitude exhibit a complex dependence on applied field that depends strongly on the relative orientation of $\boldsymbol{H}$ and $\boldsymbol{B_{THz}}$.

We measure the THz absorption spectra in four configurations of the THz polarization and the external magnetic field $\boldsymbol{H}$ in reference the two principle optic axes, $\boldsymbol{a'}$ and $\boldsymbol{b'}$ as

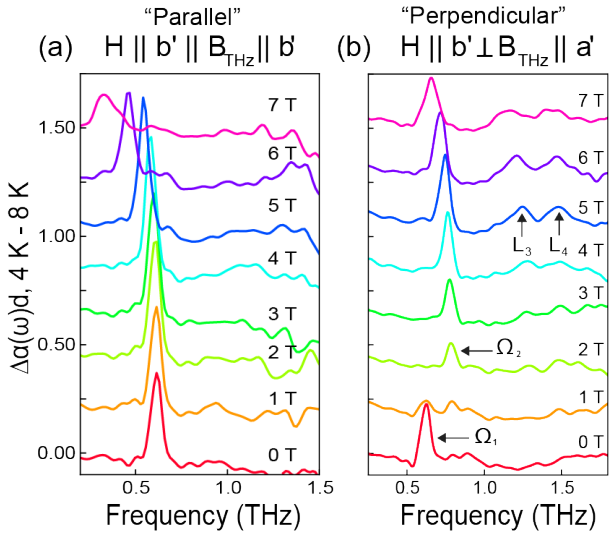

Figure 4.9: (a) THz absorption difference spectra (4 K - 8 K) as a function of frequency, for different values of $\boldsymbol{H}$ measured in the Parallel configuration $\boldsymbol{H}||\boldsymbol{b'}||\boldsymbol{B_{THz}}$. Only Ω_1 magnon absorbs. (b) Difference spectra for perpendicular configuration, $\boldsymbol{H}||\boldsymbol{b'}$, $\boldsymbol{B_{THz}}||a'$, showing all four magnon absorption peaks. Traces are offset for clarity.

defined in 5.1. Up until this point, we have only discussed the "parallel" configuration with $\boldsymbol{H}||\boldsymbol{b'}||\boldsymbol{B_{THz}}$ or $\boldsymbol{H}||\boldsymbol{a'}||\boldsymbol{B_{THz}}$. Spectra in the parallel configuration are plotted in 4.10, were the single Ω_1 magnon shifts to lower frequency and broadens with increasing field. The "perpendicular" configuration, where $\boldsymbol{H} \perp \boldsymbol{B_{THz}}$ is shown as measured along the $\boldsymbol{a'}$ in 4.10 (b). These spectra are more complex, in that there is and additional magnon $\Omega_2 = 3.3$ meV at zero field. The frequency and spectral weight of these modes appears to vary non-monotonically with field. Additionally, two broader features, which we denote by L_3 and L_4, appear in the energy range of 4 - 6 meV and become more strongly absorbing with increasing field.

The evolution of the magnon absorption with $\boldsymbol{H}$ is greatly clarified by the color plots in 4.10. Magnon absorption was extracted by subtracting the 8 K spectra from the 4 K spectra at each value of H. The magnitude of this absorption, $\Delta\alpha d$, is denoted by the color scale and plotted in the in the $\hbar\omega - H$ plane. Panels (a), and (b) (first column) show spectra with $\boldsymbol{H} \parallel \boldsymbol{a'}$, for $\boldsymbol{B_{THz}}$ parallel and perpendicular to $\boldsymbol{H}$, respectively. Panels (c), and (d) are the corresponding spectra for the $\boldsymbol{H} \parallel \boldsymbol{b'}$ configuration. Panels (e) and (f) show theoretical spectra obtained by LSWT calculations, which will be described in the next section.

There are several interesting features revealed by plotting the spectra in this way. First, we note that the anisotropy with respect to rotation of the crystal by 90° is weak, that is,

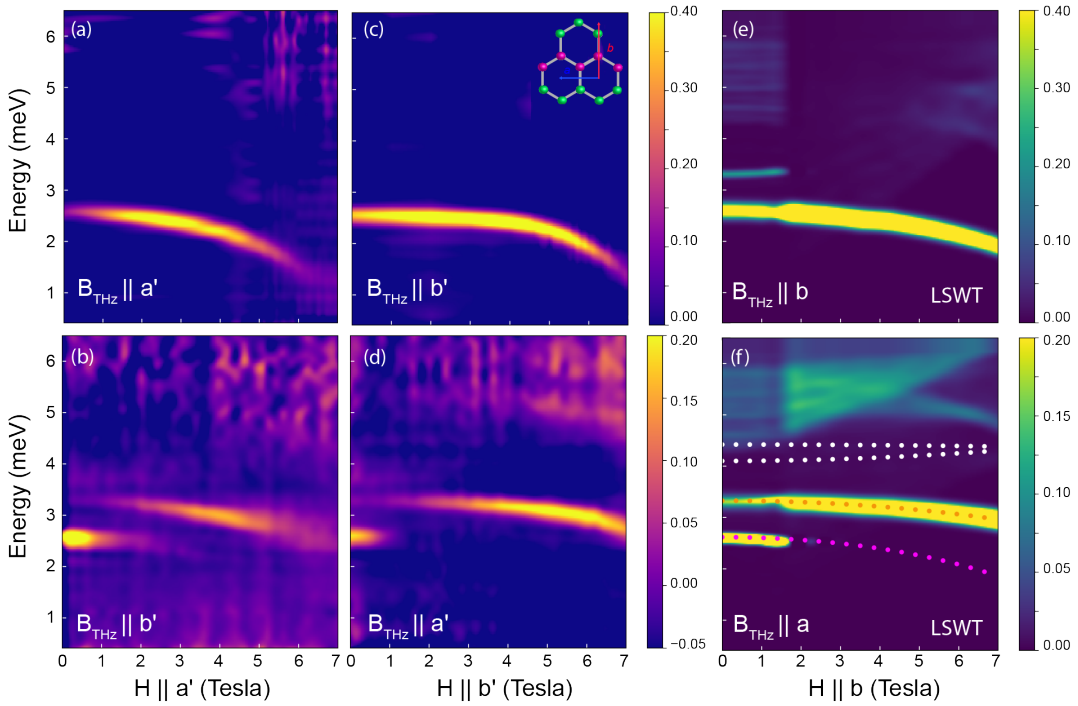

Figure 4.10: Magnon energies and absorption strengths at $\boldsymbol{q} = 0$ as a function of external in-plane magnetic field, H. Experimental data is in panels (a)-(d). Magnon absorption was extracted by subtracting the 8 K spectra from the 4 K spectra at each value of H. Spectra were taken in 0.2 T steps from 0 - 5 T and in 0.1 T steps from 5 - 7 T; intermediate field values are interpolated. The mode dispersion is Note the difference of color scales: absorption in the parallel configuration is roughly twice as strong. Panels (e) and (f) show LSWT calculations for absorption in $\boldsymbol{H} \parallel \boldsymbol{b}$ with the probe field parallel and perpendicular, respectively. Solid dots overlaid on (f) represent mode energies predicted by LSWT. The orange and pink dots coincide with observed Ω_1 and Ω_2. Two higher energy modes (white dots) are forbidden by selection rules and do not contribute to THz absorption. Intensity in the region 4 - 6 meV, consistent with observed L_3 and L_4, results from 2-magnon absorption.

the pair of panels (a) and (b) (where $\boldsymbol{H}||\boldsymbol{a'}$) share the same qualitative features as panels (c) and (d) (where $\boldsymbol{H}||\boldsymbol{b'}$), respectively, with overall amplitude difference of only ~ 2.

As we discuss below, LSWT predicts a much larger anisotropy in the dynamic susceptibility between the two principal ($\boldsymbol{a}$ and $\boldsymbol{b}$) axes of a single zigzag domain. We attribute the observed weak anisotropy to the presence of multiple structural domains.

Second, we note that in the parallel configuration, panels (a) and (c), the width of the peaks remains relatively constant until around H $\sim$ 5 T at which point they start to broaden [28]. The broadening occurs more rapidly for $\boldsymbol{H} \parallel \boldsymbol{a'}$ as is apparent in Fig. 2 (a), where the Ω_1 magnon becomes diffuse approaching 7 T. This is an indication that for $\boldsymbol{H} \parallel \boldsymbol{a'}$ the system is closer to the critical point– This is also the regime were corrections to LSWT becomes relevant.

A far stronger contrast is seen when comparing spectra in the parallel configuration, $\boldsymbol{B_{THz}} \parallel \boldsymbol{H}$ (panels (a) and (c)) to spectra in the perpendicular configuration, $\boldsymbol{B_{THz}} \perp \boldsymbol{H}$ (panels (b) and (d)).

For $\boldsymbol{B} \parallel \boldsymbol{H}$ we observe the Ω_1 magnon shifts to lower frequency with increasing H, with the field-induced mode softening slightly more pronounced with $\boldsymbol{H} \parallel \boldsymbol{a'}$. For $\boldsymbol{B_{THz}} \perp \boldsymbol{H}$ the color plots show clearly that there are in fact two distinct low energy modes. At $H = 0$ there is a strong mode, $\Omega_1 = 2.6$ meV, and a much weaker one, $\Omega_2 = 3.3$ meV. We note in particular the 0.7 meV splitting between these modes, which informs our LSWT calculations. As H increases the spectral weight of Ω_1 decreases rapidly and then shifts to Ω_2 for H $\sim$ 1.5 T. Surprisingly, the total spectral weight at this crossover field is close to zero.

The absorption features centered at $L_3 = 5.2$ meV and $L_4 = 6.2$ meV which appear at $\boldsymbol{H} = 4$ T, grow with increasing $\boldsymbol{H}$ and persist as $\boldsymbol{H}$ approaches $\boldsymbol{H_c}$. An exact diagonalization study of α-$RuCl_3$ associated eigenstates in this energy range with a two-magnon continuum [109]. Our results for $\chi''(\omega)$ using LSWT account for the field and polarization dependence of L_3 and L_4, and confirm their origin as two-magnon excitations in the longitudinal response, that is, $\boldsymbol{B_{THz}}$ parallel to the zigzag wavevector.

4.2.2 MAGNETIC SUSCEPTIBILITY ANALYSIS

We use the absolute determination of $\chi''(\omega, \boldsymbol{Q} = 0)$ provided by THz absorption, to track the the dependence of the spin wave spectral weight on H for $\boldsymbol{B_{THz}} \parallel \boldsymbol{H}$ and $\boldsymbol{B_{THz}} \perp \boldsymbol{H}$. These spectral weights are then compared with the static susceptibility, $\chi(\omega = 0, q = 0)$, measured by low frequency susceptometry in the parallel configuration, to determine the relative contributions of spin wave vs. continuum to the total weight of magnetic fluctuations at zero wave vector.

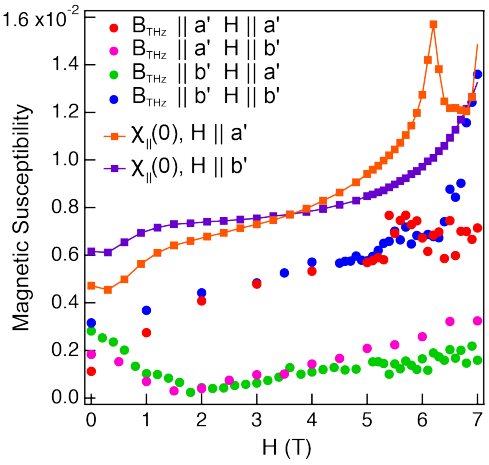

Figure 4.11: Colored dots: Contribution of $\boldsymbol{Q} = 0$ magnons to static magnetic susceptibility, $\chi(0)$ as measured by fits to THz spectra for all four configurations of $\boldsymbol{H}$ and $\boldsymbol{B_{THz}}$. Orange and purple squares: Total value of $\chi_{\parallel}(0)$ as measured by low- frequency susceptometry for two directions.

In the parallel configuration, we extract the magnon contribution to the static susceptibility from the raw absorption spectrum using the same procedure described in the previous section. We subtract the spectra at T = 4 K and H = 0T from the spectra at H=1-7 T, removing any field-independent features. We fit the residual spectra to the subtraction of two Lorentzian lineshapes, 4.4 and apply the thermodynamic sum rule. In the perpendicular orientations, the appearance of the additional peaks Ω_2 and L_3 and L_4 make the field subtraction process described above unfeasible. In this case, $\chi_{sw}(\omega = 0)$ instead was determined by fitting a single Lorentzian function to the the differential spectra across the Néel temperature.

There are a few interesting things to note about this data. First we consider the parallel configuration (red and blue dots). The data here agrees with the measurements presented in the previous section, but the increased resolution in field (0.2 T) reveals a small peak in $\chi(0)$ in the range of 5 -6 T. After the TDTS data described in this thesis was published in 2018, newer field-dependent INS measurements [5] indicated signatures of an additional transition between two related zigzag magnetic states at 6T, as a result of previously ignored inter-layer coupling. In retrospect it is possible that the modulation of the magnon spectral weight in this field range, as measured by TDTS, is related to this transition.

Second we consider the perpendicular configuration (green and pink dots). We find that the transfer of spectral weight between the Ω_1 and Ω_2 modes corresponds to a near-zero minimum in the magnon contribution to $\chi(0)$ at H = 1.5 T. As will be discussed in the

following sections, we find this minimum in magnon spectral weight corresponds to a low-field spin-flop-like crossover resulting from competition between the anisotropy of local distortions and the applied field.

4.2.3 LINEAR SPIN WAVE THEORY

Linear Spin Wave Theory calculations were implemented by our collaborator Erik Aldape in the group of Ehud Altman at UC Berkeley.

Motivated by the existence of sharp spin wave resonances with large spectral weight throughout the antiferromagnetic phase, we compare our experimental results with calculations based on linear spin wave theory (LSWT). Linear spin wave theory is a method for the calculating the dispersion of magnetic excitations wave in the dilute limit of magnon fluctuations above a classical spin configuration. We carry out LSWT theory calculations following the methods of Holstein and Primakoff [110], and Colpa et al. [111].

The result is that LSWT does quite well to predict the essential features of the THz spectra – the number of modes, their spectral weight and optical selection rules, the variation of resonant frequency with H, and a discontinuity in mode frequency and amplitude at a low field of $\sim$ 1.5 T. The fact that LSWT is able to so accurately model the data, even approaching the transition to the quantum disordered state at the critical field, is somewhat surprising because LSWT is a semi-classical approach. LSWT only reliable if the quantum (or thermal) fluctuations of the magnetic moment are small compared to the ordered moment, in which case the normal modes are non-interacting magnons.

The starting point for the LSWT calculations is the effective spin Hamiltonian,

$$\begin{aligned} H_S = &\sum_{<ij>} \left[J_1 \boldsymbol{S}_i \cdot \boldsymbol{S}_j + \Gamma (S_i^{\alpha_{ij}} S_j^{\beta_{ij}} + S_i^{\beta_{ij}} S_j^{\alpha_{ij}}) + K S_i^{\gamma_{ij}} S_j^{\gamma_{ij}} \right] \\ &+ \sum_{<ij>_3} J_3 \boldsymbol{S}_i \cdot \boldsymbol{S}_j - \mu_B g \sum_i \boldsymbol{H} \cdot \boldsymbol{S}_i \end{aligned} \tag{4.7}$$

where $\langle ij \rangle$ and $\langle ij \rangle_3$ denote summation over nearest neighbor and third neighbor bonds, respectively [26, 34, 50, 112, 113]. K is the Kitaev interaction, Γ is the symmetric off-diagonal term and J, J_3 are the nearest-neighbor and third neighbor Heisenberg couplings, respectively. The γ_{ij} are bond labels (x, y, or z) as shown in Fig. 1 (a) and α_{ij}, β_{ij} are the two remaining directions for each bond. Note that the magnetic field is expressed in spin-space components, for example, $\boldsymbol{H} \parallel \boldsymbol{a}$ is expressed as $\boldsymbol{H} = H\,(1, 1, -2)/\sqrt{6}$ and $\boldsymbol{H} \parallel \boldsymbol{b}$ is $\boldsymbol{H} = H\,(1, -1, 0)/\sqrt{2}$.

The LSWT theory proceeds in two stages. The first step is minimizing the energy of the classical spin parameters in the Hamiltonian; we must choose the correct of parameters which lead to a classical ground state with the observed zigzag antiferromagnetic order. Second, the collective modes are obtained by expanding the Hamiltonian to quadratic order in the fluctuations about the ordered magnetic moment [110, 111, 114]. The theoretical THz absorption is obtained by

computing the linear response of the magnons to an oscillating magnetic field. Further details on LSWT may be found in the Appendix to Ref. [29].

4.2.3.1 CHOICE OF HAMILTONIAN PARAMETERS

One motivation for our detailed THz study of the ordered phase is so that we may provide insight into set a parameters for the magnetic hamiltonian Eq. 4.2.3 which closely describe the data. Our starting point is the representative values found by Winter et al. [109, 113] to model INS data, and we adjust them to fit the energies of the modes seen by our TDTS. We note that an alternative set parameters suggested by Ran et al. [53], were obtained by fitting exclusively to INS spectra at the M point (rather than the Γ-point), yielding spin wave energies at $\boldsymbol{Q} = 0$ much larger than found experimentally.

Carrying out LSWT with the parameters of Winter et al. leads to an accidental degeneracy of modes Ω_1 and Ω_2. Refinement of these parameters is needed in order to account for our observation that these modes are split by 0.7 meV at $H = 0$. Reproducing the splitting between these modes may be achieved by increasing the relative strength of the Γ term, such that $\Gamma/K \sim -1$ instead of $\Gamma/K = -1/2$. A representative fit to the energies of modes Ω_1 and Ω_2 as a function of H using the parameter set (J, K, Γ, J_3) = (-0.35, -2.8, 2.4, 0.34) meV is shown as dots in 4.10 (e). We assume the same in-plane g-factor of 2.3 as used by Winter et al. [109, 113].

The calculated energies of the magnon modes are an excellent fit to the spectra measured by TDTS. Nevertheless the parameters we have chosen should not be viewed as a definitive set representing microscopic interactions. As we show below, there are sizable quantum corrections to spin wave theory, which should be viewed as based on renormalized parameters. Such renormalized interactions may be dependent on magnetic field and the wave vector of the mode. In this context the main role of the LSWT analysis is to explain the origin of defining features of the spectra, such as spectral weight ratios, zero-field splittings, polarization selection rules, and trends with increasing applied magnetic field.

4.2.3.2 SYMMETRY-RELATED SELECTION RULES

In the zigzag state, the unit cell of the honeycomb is enlarged to include four sites; as such there are four independent dispersing magnon modes. The classical energies of these modes are overlaid on 4.10 (f). However, of these four modes, as illustrated by the spectra in reffig12 (d), we do not observe THz absorption at these energies. In fact only two of four modes contribute contribute to THz absorption, corresponding to the lower energy Ω_1 and Ω_2 modes. This is dictated by selection rules arising from the symmetry of the zigzag AFM ground state.

In particular, the zigzag order has two residual Z_2 symmetries. First, we consider the sublattice symmetry, or the simultaneous exchanging spins within each ferromagnetic zigzag strip. The $(q) = 0$ magnons transform under representations of this symmetry. The lower energy modes, Ω_1 and Ω_2 are even under this transformation, while the two higher energy modes are odd. The uniform in-plane THz magnetic field is even under this transformation and thus cannot

excite these modes. In other words, the two higher energy modes do not have a net magnetic dipole moment in the unit cell– and thus cannot be excited by the uniform in-plane THz field. Thus we do not associate the observed peaks at L_3 and L_4 with these modes– these are instead identified to be contributions from 2-magnon absorption as described below.

The second Z_2 symmetry is a spin-space symmetry of the zigzag state which is only exact at zero external field. This symmetry involves the exchange of spin-interaction directions, x, y or z as defined in 2.1 and 2.4. This is best explained by example. Consider that if the bond that joins the ferromagnetic zigzag strips is z-type, then then exchange of the x and y spin coordinates is a symmetry of the system. One of the lower modes, Ω_1 is odd under this transformation, while Ω_2 is even. The in-plane probe field, $\boldsymbol{B_{THz}}$, if applied parallel or perpendicular to the ordering wavevector of the zigzag state will be respectively odd or even under this transformation and couple to a mode of the same parity.

In other words, this second selection rule constitutes that the optically active modes have a well-defined polarization. In particular, Ω_2 is polarized along the $\boldsymbol{b}$ direction of a single monoclinic domain, while Ω_2 is polarized along the $\boldsymbol{ac}$ direction. Thus, the contribution of each mode to the THz absorption will depend strongly on relative orientation of $\boldsymbol{B_{THz}}$ and the ordering wavevector of the zigzag magnetic order in the ab plane. Additionally, LSWT predicts that the THz absorption from Ω_2 will absorb more strongly than Ω_1, as Ω_1 is partially polarized in the out-of-plane direction. All of this comes into play when describing the crossover in spectral weight between the two optically active magnons at low field and corresponding minimum in magnetic susceptibility, discussed in the following section, 4.2.4.

4.2.4 LOW-FIELD CROSSOVER

We now discuss the intricate mode-switching behavior observed at low magnetic fields in the perpendicular configuration. The key to accurately modeling these spectra (Fig. 4.12) lies in considering the polarization selection rules for the two optically active magnon modes, and the presence of multiple C_3-symmetry breaking magneto-structural domains.

As mentioned in 4.2.3, the first step in LSWT is finding the spin configuration for the classical ground state . For isotropic coupling constants and no magnetic field, there are three degenerate zigzag ground states states with ordering wavevector $\boldsymbol{Q}$ = Y, M, or M′, as illustrated in 4.12 (a). These classical spin configurations, are depicted with the spins projected onto the ab plain. The application of an external magnetic field selects the ordering wavevector that is closest to being parallel to it. Thus H||b (along a Ru-Ru bond direction) selects the Y order, while H || a (perpendicular to a Ru - Ru bond direction) favors the M and M′ states, which remain degenerate.

The crossover at H =1.5 T, where spectral weight is transferred from Ω_2 to Ω_1 in (b) and (d) of 4.10, coincides with the disappearance of magnetic Bragg peaks corresponding to one of the three possible degenerate orientations of zigzag order on the honeycomb lattice [7, 61]. Previously, this effect was interpreted assuming that the three degenerate zigzag orientations

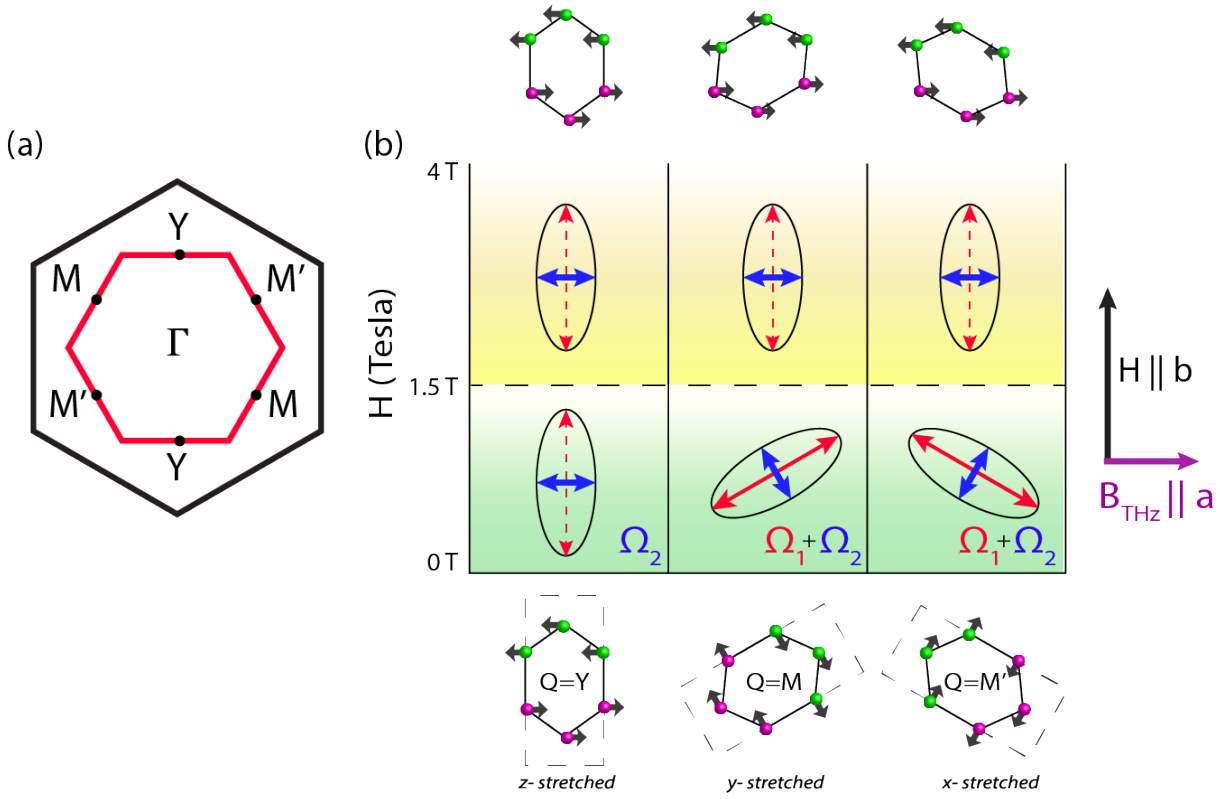

Figure 4.12: (a) Schematic of a hexagonal lattice (black), hexagonal Brillouin zone (red) with the orientation of the wavevectors of three degenerate zigzag AFM states labelled by Y, M, and M′. Illustration of the evolution of the three possible zigzag states and active modes for perpendicular case $\boldsymbol{H} \parallel \boldsymbol{b}$, $\boldsymbol{B}_{THz} \parallel \boldsymbol{a}$, where $\boldsymbol{a}$, $\boldsymbol{b}$ are axes of the z-stretched domain. Bottom row of honeycombs shows preferred spin orientations at H = 0 T, with ordering wave vectors defined with respect to the z-stretched domain. The ellipses show the projection of polarization of Ω_1 (red) and Ω_2 (blue) onto the *ac* plane for each domain above and below $H_X = 1.5$ T. Solid arrows indicate a mode that absorbs for $\boldsymbol{B_{THz}} \parallel \boldsymbol{a}$, dashed arrows indicate a mode that does not absorb. Upper row of honeycombs shows reorientated spins above H_X.

are present as domains [61], and that the application of a magnetic field lifts the degeneracy, driving energetically favored domains to grow at the expense of others. The possibility that the disappearance of magnetic Bragg peaks is related to a gradual reorientation of the ordered moments within domains was also discussed [7]. The picture of gradual domain growth [61] or spin reorientation [7] is incompatible with the abrupt changes in the THz spectra at 1.5 T.

Instead, we consider that a monoclinic distortion of the lattice will lift the three-fold degeneracy of the zigzag ground state– even in zero applied field– selecting the M, M′ or Y respectively zigzag order, respectively. Monoclinic distortions are incorporated into into the spin Hamiltonian in LSWT by reducing the coupling constants J, K and Γ for a certain"stretched" bond. The zigzag orientation with $\boldsymbol{Q}$ parallel to the direction of its stretched bond (local monoclinic $\boldsymbol{b}$ axis) is energetically favored, the two other orientations of $\boldsymbol{Q}$ are related by $\pm 120^{\circ}$ rotation are degenerate and higher in energy.

The dependence of the relative energy of these three orientations on $\boldsymbol{H}$ will lead to a field-induced level crossing. That is, the wavevector of the local zigzag order will abruptly switch at some crossover field value, $\boldsymbol{H_X}$, for which the external field strength overcomes the anisotropy of the lattice distortion. We refer to this phenomenon as a "$\boldsymbol{Q}$-flop" crossover to distinguish it from the conventional spin-flop transitions in AFMs, with the distinction that here the rotation involves both the direction of the moments and wave vector of the magnetic order. This scenario, applied to the evolution of the spectra with magnetic field is best explained graphically. This is illustrated in Fig. 4.12, which presents a cartoon phase diagram of the energetically preferred zigzag states and corresponding optically active modes for each of the three domains as a function of $\boldsymbol{H}$, for perpendicular field configuration where $\boldsymbol{H}||\boldsymbol{b}$ and $\boldsymbol{B_{THz}}||\boldsymbol{a}$.

The bottom row Fig. 4.12 shows the zigzag spin ordered states for each of the three domains at $H = 0$, where the spins are projected onto the ab plane. For $H < H_X$, a monoclinic distortion along the x, y, or z-stretched bonds selects an ordering wavevector in the M, M′, or Y direction. The ellipses and arrows demonstrate the polarization of Ω_1 and Ω_2 magnons in each domain. LSWT predicts that the absorption of the Ω_1 mode in response to the in-plane THz field is about 6 times greater than that of Ω_2; this is reflected in the eccentricity of the ellipses. Consider the lower row of polarization states (green shading) for $H < H_X$. For the $Q = Y$ domain, only the Ω_2 mode contributes to the absorption. For $Q = M, M'$ domains, the Ω_2 mode contributes weakly while the Ω_1 mode contributes strongly. As all three domains are present in the sample, the TDTS spectra will reflect an average of all these contributions. This is indeed the case– in Fig 4.10 (b) and (d), at fields below 1.5 T, we see primarily absorption from Ω_1 with only a weak contribution of spectral weight from Ω_2.

As the external field is increased, our LSWT calculations show that the application of $\boldsymbol{H}$ favors zigzag orientations for which $|\boldsymbol{Q} \cdot \boldsymbol{H}|$ is largest– $\boldsymbol{H}$ favors the domain where the zigzag wavevector aligns with $\boldsymbol{H}$. At some point, as $\boldsymbol{H}$ is increased, the $\boldsymbol{Q} \cdot \boldsymbol{H}$ energy gain becomes move favorable than the state selected by the zero-field lattice. That is, at the crossover field, H_X=1.5 T, the zigzag wavevector of all three domains zero-field domains suddenly flops to align with the direction selected by the magnetic field, while structural domains remain intact. The field-induced crossover is illustrated in Fig. 4.12. In this case $\boldsymbol{H}$ favors the domain shown in

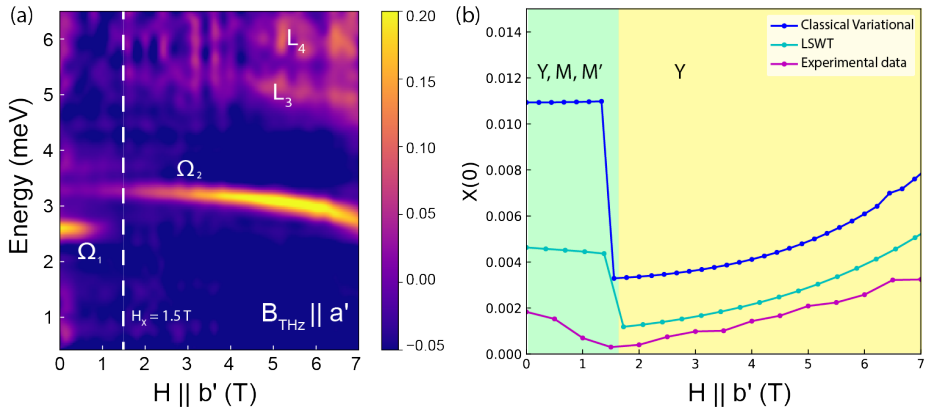

Figure 4.13: (a) THz absorption spectra for $\boldsymbol{H}||\boldsymbol{b'}$, $\boldsymbol{B_{THz}}||\boldsymbol{a'}$ with labels to indicate magnon absorption and the crossover field at 1.5 T. (b) Magnon contribution to the total static susceptibility $\chi(0)$ measured by TDTS (magenta), as well as calculated by a classical variation method (blue) and a LSWT including quantum corrections (cyan).

the left-hand column ($\boldsymbol{Q} = Y$), in which the z bonds are stretched. For $H > H_X$, the zigzag wave vector of the y and x domains will reorient to the $\boldsymbol{Q}$ of the z-stretched domain, and the resulting magnetic states are shown in the top row of the figure. The corresponding magnon polarization states are shown in the the yellow shaded region of Fig. 4.12, where all of of the ellipses are now aligned with the field and only Ω_2 contributes to the absorption. This is clear in the data (Fig. 4.11), where at 1.5 T the absorption from Ω_1 is greatly diminished and the absorption from Ω_2 becomes stronger as the field is increased.

4.2.4.1 CROSSOVER IN LSWT

To implement this scenario in LSWT, we must consider an average of LSWT results calculated separately for three individual honeycomb "patches". The discontinuous crossover observed at 1.5 T in the perpendicular configuration cannot be reproduced in LSWT if only a single zigzag domain is considered.

For each patch, a different bond type is effectively lengthened by reducing all interactions across this bond by 3%, and thereby selecting one of the three possible zigzag orders as the preferred ground state. The competition between $\boldsymbol{H}$ and the lattice anisotropy is implemented in the calculation by assuming the zigzag order with the minimum classical energy in each patch and calculating the resulting magnon absorption for each value of $\boldsymbol{H}$. The LSWT results for each patch are then averaged to reproduce the experimental spectra. The crossover is reproduced in

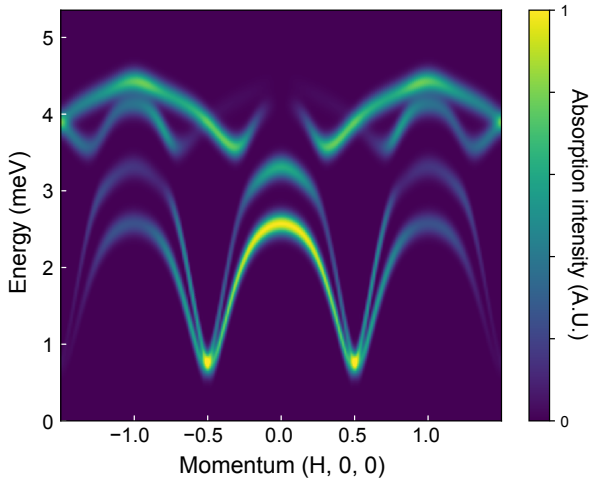

Figure 4.14: Theoretical absorption spectra across the Brillouin zone, as calculated in LSWT.

LSWT, as shown in Fig. 4.10 (e) and (f). The scale the crossover field, and the fact that it occurs for multiple directions of in-plane applied field sets constraints for future studies which will necessarily consider bond-dependent couplings.

In Fig. 4.13 we show that the multi-domain LSWT theory described above captures the curious deep minimum in spectral weight for $\boldsymbol{B_{THz}} \perp \boldsymbol{H}$ at 1.5 T (expressed as $\chi_{\perp}(0)$). The upper theoretical curve (blue) is the classical result, while the lower curve (cyan) includes zero-point fluctuations of the spin 1/2 moments. The sudden reduction in spectral weight for $\boldsymbol{B_{THz}} \perp \boldsymbol{H}$ occurs when the applied field aligns the $\mathbf{Q}$ of each domain, such that at $H = H_X$, $\boldsymbol{B_{THz}}$ couples only to the weaker Ω_2 mode. Although the crossover predicted by the theory is sharp when compared with experiment, broadening of the $\boldsymbol{Q}$-flop crossover is expected in the presence of structural disorder. We note that our scenario is consistent with the increase of the M point spin-wave intensity at 2 T observed in INS measurements [7].

4.2.5 TWO-MAGNON CONTRIBUTION

Finally, we discuss the features L_3 and L_4 that are observed in the $\boldsymbol{B_{THz}} \perp \boldsymbol{H}$ channel in the photon energy range $\sim 4 - 6$ meV, as shown in Fig. 4.10 and labeled in 4.13. These modes cannot be identified as single magnon excitations because of the exact Z_2 symmetry discussed above. However, LSWT predicts absorption by a continuum of two-magnon states in precisely this energy range. Furthermore, the two-magnon absorption is predicted by LSWT only to appear in the longitudinal response, that is for $\boldsymbol{B_{THz}}$ parallel to the ordered moment. As shown in 4.12, for $H > 1.5T$ the moments have flopped to an orientation parallel to the THz probe field (and perpendicular to $\boldsymbol{H}$). Thus the two-magnon interpretation of L_3 and L_4 is consistent with the data, where these features appear only $\boldsymbol{B_{THz}} \perp \boldsymbol{H}$ and at fields above 1.5 T.

Although the selection rules show unambiguously that L_3 and L_4 are two-magnon excitations, the details of the calculated field dependence (Fig. 2(f)) differ from the data. The most likely origin of this discrepancy is that while the single magnon modes are measured at $\boldsymbol{Q} = 0$ the two-magnon absorption depends on the spin wave dispersion over the entire Brillouin zone. While our THz data cannot access momenta other than $\boldsymbol{Q} = 0$, we can of course calculate the dispersion in LSWT throughout the Brillouin zone. The result is shown in Fig. 4.14. Our LSWT parameters reproduce the local minima at the M-points seen by INS, however they do not reproduce the local minimum observed also at the Γ-point [7].

Indeed, all the theoretical models of this system studied to date do not reproduce this feature of the INS data [109, 115] However we find that a Γ-point minimum appears within LSWT when further interactions are added, for example second nearest-neighbor ferromagnetic coupling. Finding a spin Hamiltonian that describes all aspects of the single-magnon, two-magnon, and INS spectra – as well as potential exotic states at fields above 7 T, is an on-going area of research.

4.3 CONCLUSIONS AND OUTLOOK

Our contributions to the understanding of the low energy spectra include the identification of a large continuum resulting from electric dipole absorption in relevant energy range for magnetic absorption (0.1-8 meV). Using the thermodynamic sum rule for $\chi(0)$, we can quantify the strength of a magnetic absorption continuum, relative to absorption from the well-defined magnon modes associated with the ordered state in the vicinity of the critical field. We observed that the size of the magnetic continuum is small compared to the absorption related to magnons, even approaching the critical field. If there is indeed a phase transition to a QSL is indeed near 7 T, one may expect a continuum contribution related to fractional excitations to strengthen approaching the disordered phase.

Furthermore, we studied the evolution the magnon excitations in α-$RuCl_3$ as a function of THz polarization and applied field. We resolved four distinctive absorption features associated with the ordered phase, clearly identifying the contribution from both single-magnon and two-magnon states and quantifying the selection rules for these excitations. A Linear Spin Wave Theory (LSWT) model was developed to closely fit the data, which required the consideration the C_3-breaking of the honeycomb lattice and the resulting multi-domain structure. This insight allowed us to elucidate a field Q-flop crossover at around 1.8 T. Tuning of parameters in LSWT even allowed us provide insight into the effective spin Hamiltonian. Apart from this, this work demonstrates the power of THz spectroscopy as a technique, especially with an ideal sample like α-$RuCl_3$.

By now, low energy excitations in α-$RuCl_3$ have been studied extensively by us and other groups, sometimes with slightly differing results, likely due to different levels of disorder in the various crystals studied. Nonetheless what is important to grasp in the search for a QSL, is that there are salient features that emerge as broader trends from the work across the community from which we can piece together the story of this fascinating material. Perhaps the most

pertinent question going forward, concerning the fate of α-$RuCl_3$ is if the quantized thermal hall results [6], as discussed in Chapter 2, may be reproduced.

PART II

THREE-STATE NEMATICITY IN INTERCALATED TMDS

5

FROM SPIN LIQUIDS TO SPINTRONICS

5.1 INTERLUDE

Before diving into our investigation of nematic order in $Fe_{1/3}NbS_2$, we spend a few sentences to tie together the two halves of this dissertation. The search for exotic spin liquid states in the Mott-insulating α-$RuCl_3$ and an investigation into properties of magnetic transition metal dicalchogenide (TMD) compound with recently discovered AFM spintronic properties may seem like disparate topics. Quite to the contrary, these topics are fundamentally connected.

The obvious connection is that both of these materials are AFMs. But beyond that, they are both layered materials where we treat the magnetism as essentially two-dimensional and the properties of interest emerge from frustration on lattices with 6-fold symmetry.

In α-$RuCl_3$, frustration results from bond-dependent coupling of neighboring spins– predicted to give rise to fractional excitations which we searched for signatures of in THz spectra. The high sensitivity to crystal symmetry afforded by our polarized spectra allowed us to tease out magnon selection rules in a crystal containing monoclinic distortions and multiple domains.

In our study of intercalated TMDs, we also employ an optical polarimetry technique to detect distortion of the lattice, however, in this case the distortion is the driver of the interesting physics in the material. As opposed to α-$RuCl_3$, here the frustration is geometric, arising from the interactions of Ising spins on a an equilateral triangle – a classic example [23, 116, 117]. In $Fe_{1/3}NbS_2$ AFM emerges on a triangular superlattice of Fe atoms intercalated between the TMD layers. We detect a sudden onset of optical birefringence at the Néel temperature, indicating the lowering of rotational symmetry in the magnetic phase. Qualitatively at T_N, a distortion along one direction of Fe-Fe bonds relieves the geometric frustration, allowing one of three degenerate ordered phases to condense.

The work presented here is the first demonstration of a Z_3 nematic-magnetic phase transition on the triangular lattice [30]. Our observations and the accompanying theory open the door to understanding a broader class of triangular and hexagonal materials systems which may exhibit nematic phases including twisted bilayer graphene [118]. While the work presented thus far certainly satisfies Louis Nèel's posit that antiferromagnetism is theoretically interesting, the following chapters deal in an emerging class of materials where it may also be found applicable.

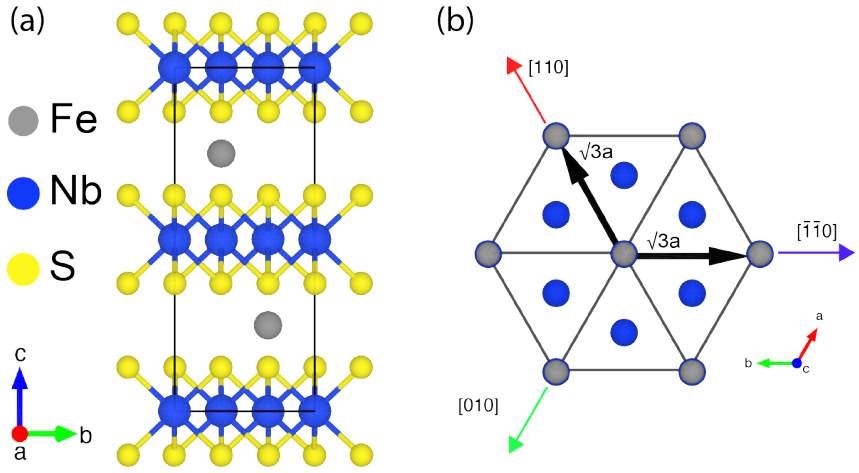

Figure 5.1: (a) Crystal structure of $Fe_{1/3}NbS_2$ where Fe-atoms are intercalated between TMD layers. For x=1/3 Fe-concentration, the crystal forms in the non-centrosymmetric space group P6322. (b) View along the *c*-axis shows the magnetic Fe-atoms form a triangular super-lattice with $\sqrt{3}a \times \sqrt{3}a$ unit cell.

5.2 MAGNETISM AND SWITCHING EFFECTS IN IRON-INTERCALATED TMDS

Transition metal dichalcogenides (TMDs) are a class of layered materials exhibiting a range of material properties spanning the space of semiconductors, metals, and superconductors. By definition TMDs are of the form MX_2 where M is a transition metal and X is a chalcogen atom (O, S, Se, Te). These materials have been widely studied in the last decade; as they may be exfoliated down to a monolayer, TMDs provide a platform for studying exotic physics in two dimensions as well as exhibit tunable electronic properties which may be useful in future device technology [119].

Typically TMDs are non-magnetic. However, intercalation of magnetic ions in between the TMD layers may stabilize magnetic order. The form of magnetism depends of course on the type of TMD layer as well as type and concentration of magnetic intercalant. Intercalated TMDs have been studied since the 1970s [120–123], and have been shown to host a range of interesting properties including helical magnetic states and chiral structural domains [124].

In the following we will investigate the magnetic phase transition to AFM and low temperature domain properties of Fe- intercalated 2H-NbS_2. This compound has been shown to form a *c*-axis antiferromagnet below a Néel of approximately 50 K [125]. However the nature of the magnetism depends strongly on the amount of intercalant– in particular the magnetic Fe atoms form a super-lattice structure with two stable structural motifs at x = 0.25 (centrosymmetric) and x=0.33 (non-centrosymmetric) [126]. The crystal structure and Fe-superlattice for x=0.33 is illustrated in Fig. 5.1. Samples of intermediate Fe-concentration have been shown to exhibit frustrated, spin-glassy states and up to 3.1 T exchange bias [127].

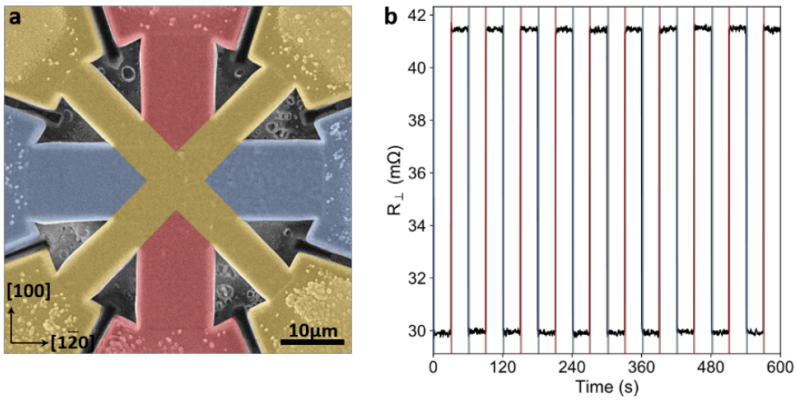

Figure 5.2: (a) False-color image of the $Fe_{1/3}NbS_2$ FIB device used in resistance switching measurements. Current pulses on the order of $\times 10^4$ A/cm^2 are applied along either the red or blue bar to switch the device. The transverse resistance is measured using a small probe current along the yellow bars. (b) Plot of stable resistance switching behavior, showing the transverse resistance measured in response to current pulses along the red and blue bars of the device in (a) applied every 30 seconds. This figure originally appeared in Ref. [8], and is reprinted with permission from Springer Nature.

Of particular interest are samples of Fe_xNbS_2 with Fe-concentration of approximately x=1/3, with the non-centrosymmetric space group and triangular $\sqrt{3}a \times \sqrt{3}a$ magnetic superlattice shown in Fig. 5.1. Recently both current-induced resistance switching and multi-stable memory effects were reported in samples of $Fe_{1/3}NbS_2$ when cooled below T_N [8]. This discovery comes at time when there is intense research interest in incorporating AFMs into spintronic applications. Resistive-switching AFMs offer promise of faster response, lower threshold current, and the possibility to scale to smaller dimensions than their ferromagnetic counterparts [16].

Stable switching of electric resistance by application of a spin-unpolarized current has been previously observed in AFM thin films CuMnAs, Mn2Au, and NiO [128–130]. In closely related work, multi-stable magnetic memory with electric read-out was demonstrated in the hexagonal AFM, MnTe [131, 132]. These systems are all easy-plane, collinear AFMs in which switching and memory are associated a spin-transfer torque (SST) mechanism [133, 134]. SST involves the rotation of the Nèel vector, $\boldsymbol{L}$, between stable states in the plane that contains a perturbing magnetic field or current, where $\boldsymbol{L} = M_1 - M_2$, and M_1, M_2 are the sub-lattice magnetizations.

In $Fe_{1/3}NbS_2$ it was found that current pulses applied parallel to the TMD atomic layers could reversibly switch a 10-micron scale device between stable resistance states. The measurements were performed on device milled out of a single-crystal of $Fe_{1/3}NbS_2$ by a focused ion beam (FIB); such a device is shown Fig. 5.2 (a). When the material is cooled into the magnetic phase, a current pulse applied along the red or blue bars will switch the value of

the transverse resistance (measured along the yellow bars) between two stable resistance states, as shown in Fig. 5.2 (b). The threshold current required to switch $Fe_{1/3}NbS_2$is significantly lower than the current required for CuMnAs, albeit at lower much temperatures. Moreover, anisotropic magneto-resistance measurements showed that cooling through the Néel temperature in an in-plane magnetic field, H, induces an in-plane resistivity anisotropy whose symmetry axes continuously follow the direction of H and remain stable after the field is turned off. [8].

In contrast to other AFM switching materials, in $Fe_{1/3}NbS_2$ the anisotropy of the static magnetic susceptibility, χ, suggests that the Néel vector $\boldsymbol{L}$ is oriented primarily perpendicular to the TMD planes and thus primarily perpendicular to the applied current [125, 135]. However it was also suggested that this compound may posses a small in-plane component of $\boldsymbol{L}$, the size of which may vary depending on the amount of Fe-intercalant– and the rotation of $\boldsymbol{L}$ by current pulses may give rise to the observed switching phenomena through the SST mechanism [8]

5.3 NEMATICITY AND OPTICAL MEASUREMENTS

The following chapters will present optical measurements that suggest an intrinsic coupling between structure and magnetism in $Fe_{1/3}NbS_2$ which may have implications for understanding resistive switching behavior. First, we show that the onset of AFM order in $Fe_{1/3}NbS_2$ occurs simultaneously with a first order transition that breaks the 6-fold (screw) rotational symmetry of the paramagnetic phase. Below T_N we observe three birefringent domains whose optic axes are rotated by an angle of $2\pi/3$ with respect to each other, and present a theoretical description in the terms of a qualitatively distinct 3-fold nematic phase.

Nematicity is a term borrowed from soft condensed matter research on liquid crystals, which are macroscopically arranged rod-shaped molecules (Fig. 6.5(a)) that may orient along a preferred direction in response to an applied field. The order parameter describing such a phase is termed a "nematic director", which indicates a preferred orientation in space but does not distinguish between the axes of that orientation. [65]

The concept of nematic order may be extended to the context of condensed matter, where in crystalline materials, where the discrete symmetry of the underlying lattice also plays a role. Extending further from the classical example of liquid crystals, strongly-correlated systems carry charge and spin, leading to the emergence of coupled ordered states in which liquid crystal-like nematicity is intertwined with other degrees of freedom such as electronic, orbital, or magnetic order. [136–138]

Here we are interested in the breaking of rotational symmetry while translational symmetry is preserved. This is analogous to the nematic phase observed in the Fe-based pnictide superconductors [137, 139, 140]. For pnictide superconductors in the $BeFe_2As_2$ family, at a nematic transition temperature T_{nem}, which is in general above the superconducting phase transition but depends on doping, the four-fold (C_4) symmetry of the lattice is lowered. In experimental probes, this manifests as resistive anisotropy [139] and optical birefringence [141] in the Fe-Fe

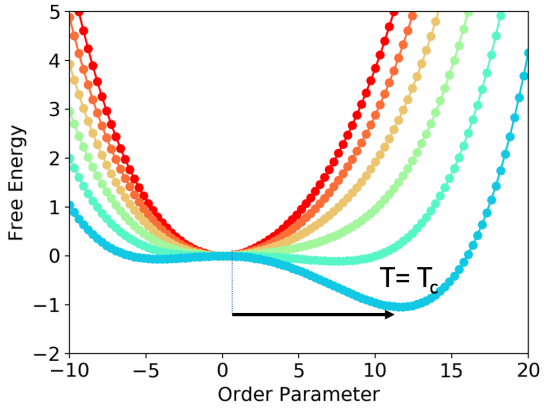

Figure 5.3: Graphical illustration of first-order phase transition in an Landau free energy, which contains a cubic term: $F = r\phi^2 - w\phi^3 + v\phi^4$, were r, w, and, v are temperature dependent. The different colors show F as a function of ϕ for decreasing temperatures. At the critical temperature T_c, a new, lower energy minima appears, corresponding to discontinuous jump in the order parameter and a first-order phase transition.

plane. This topic was widely investigated, as it was suggested that nematic fluctuations could be related to pairing interactions near the superconducting transition [142].

Similarly in $Fe_{1/3}NbS_2$, we observe the onset of birefringence, but in this case it is coincident with the magnetic phase transition (T_{nem}=T_N). As in this material magnetism lives on the triangular Fe-superlattice, we characterize ordered phase in the terms of a 3-State Potts nematic order parameter, which we discuss below.

5.3.1 LANDAU THEORY AND THREE-STATE POTTS NEMATICITY

To describe the transition to the nematic phase, we evoke the Ginzberg-Landau theory of phase transitions. Generally phase transitions are described by some order parameter, ϕ which is zero in the disordered phase and non-zero in the ordered phase. If ϕ jumps abruptly at the critical temperature, the transition is said to be first-order. On the other hand if ϕ changes smoothly, the transition is second-order. Landau theory operates under the assumption that close to the phase transition, ϕ is small and thus the the free energy can be expanded in powers of ϕ. The terms which are non-zero in this expansion are determined by symmetry alone– only terms which have the at most the same symmetry as the symmetry is which is broken by the phase transition are allowed in the free energy [65]. Terms which are even powers of ϕ are often allowed whereas terms which are odd in ϕ are often excluded. Cubic terms in the free energy may generate first-order phase transitions, as illustrated graphically for a general free energy in Fig. 7.2

With this phenomenology in mind, start our discussion of nematicity from the example of two-dimensional liquid crystals– rod like molecules with quadrupolar charge. In this case nematic

order may be described by considering distortions in the average charge density. We may describe this by a nematic order parameter, $\boldsymbol{\eta}$, which can be written as a tensor with two independent components, η_1 and η_1

$$\boldsymbol{\eta} = \begin{pmatrix} \rho_{x^2-y^2} \\ \rho_{xy} \end{pmatrix} \equiv \begin{pmatrix} \eta_1 \\ \eta_2 \end{pmatrix} \tag{5.1}$$

Where $\rho_{x^2-y^2}$ and ρ_{xy} represent quadrupolar charge densities with $d_{x^2-y^2}$ and d_{xy} symmetry. This order parameter is analogous to an XY-pseudospin– η_1 and η_2 can be thought of as the components along the x and y axes which define a total nematic director, which has a continuous rotational symmetry in 2D space.

We can extend this nematic description to crystalline materials. First we consider the widely-studied case of the Fe-pnictide superconductors, where the parent state is a tetragonal crystal with four-fold symmetry. In this case the η_1 and η_2 each transform as separate irreducible representations of the D_{4h} space group, B_{1g} and B_{2g}. As such, η_1 and η_2 are two distinct order parameters as opposed to components of the same order parameter as in the 2D liquid crystal example. This allows for additional terms in the free energy which reduce the symmetry of $\boldsymbol{\eta}$ from continuous to discrete– with two possible minima corresponding to orders η_1 and η_2. Thus we say nematic director in this case has Z_2 symmetry, it can only choose one of two possible orientations. The nematic order parameter $\boldsymbol{\eta}$ in such "Ising-nematic" systems is a scalar. [137] [138]

The crucial difference from the Ising-nematic case, is that in $Fe_{1/3}NbS_2$ the nematic order that accompanies the onset of AFM order (T_{nem}=T_N) is on the triangular Fe-superlattice. This has two important, related implications. First, because of the 6-fold symmetry, terms cubic in the order parameter are allowed in the free energy, where we may write:

$$F = \frac{a_n}{2}\left(\nu_1^2 + \phi_2^2\right) + \frac{\lambda_n}{3}\nu_1\left(\nu_1^2 - 3\nu_2^2\right) + \frac{u_n}{4}\left(\nu_1^2 + \nu_2^2\right)^2 \tag{5.2}$$

Second, the triangular Fe-superlattice has space group D_6. In this case, as opposed to Ising-nematic, η_1 and η_2 transform under the same irreducible representation E_2 of D_6 [143, 144] So order parameter may be parameterized:

$$\boldsymbol{\eta} = \eta \begin{pmatrix} \cos 2\theta \\ \sin 2\theta \end{pmatrix} \tag{5.3}$$

Where θ represents the angle of the nematic director. What distinguishes this from the case of 2D liquid crystals is the symmetry of the triangular lattice, which also constrains the symmetry of $\boldsymbol{\nu}$. Writing the free energy expansion in terms of the the parameterized $\boldsymbol{\nu}$:

$$F = \frac{a_\eta}{2}\eta^2 + \frac{\lambda_\eta}{3}\eta^3\cos 6\theta + \frac{u_\eta}{4}\eta^4 \tag{5.4}$$

We can see that this minimized by a discrete set of values for θ, in particular either by $\cos 6\theta = 1$ for $\lambda_\eta < 0$ (implying $\theta = 0,\ \pi/3$, or $2\pi/3$) or by $\cos 6\theta = -1$ for $\lambda_\eta > 0$

($\theta = \pi/6$, $\pi/2$, or $5\pi/2$). [144]. That is, there is a set of three orientations of nematic director, which minimize the free energy and these orientations locked to the high symmetry directions of triangular lattice (see Fig. 6.5 (c)). In other words $\boldsymbol{\eta}$ parameter has a discrete Z_3 symmetry.

The free energy in 5.4 is the same free energy for the three-state Potts model [145] (also discussed to some degree in [65]). The Potts Model is simply an extension of the Ising Model. Up until now, we in our discussions involving magnetic Hamiltonians, we have considered localized magnetic moments which may be in one of two spin states. In general, when we want to describe microscopic interactions in magnetic materials we are dealing with localized electron spins, so two spin states is sufficient. The Potts model, on the other hand, considers interactions between spin moments s with q possible states, we can consider a model [146]:

$$H_p = -J_p \sum_{(i,j)} \delta\left(s_i, s_j\right) \tag{5.5}$$

Which reduces to the Ising model for $q = 2$. From a microscopic perspective, this may seem like more of a toy model than anything else. However, what we have just shown in Eq. 5.4 is that for $q = 3$, this model may be mapped onto configurations of spins in $Fe_{1/3}NbS_2$ to describe the three possible nematic states. When $q = 3$, odd powers are allowed in the Landau free energy expansion (Eq. 5.4), the zero-field phase transition is found to be be first order[146]. This tracks with our optical data. Thus we refer to $\boldsymbol{\eta}$ in this case as a three-state Potts-nematic.

In the following chapters, we present optical data and theoretical analysis which show that this description may be applied to the specific case of $Fe_{1/3}NbS_2$.

5.3.2 COUPLING OF NEMATIC ORDER TO STRAIN

In our optical measurements discussed in Chapter 7, we investigate the coupling of nematic order to applied uniaxial strain. Here we describe why such a measurement may be of interest. In general, strain is expressed as third rank tensor, $\boldsymbol{\epsilon}_{ij}$.

$$\epsilon_{ij} = \frac{1}{2}\left(\frac{\partial u_j}{\partial x_i} + \frac{\partial u_i}{\partial x_j}\right) \tag{5.6}$$

Where $\boldsymbol{u}$ is the displacement vector. We are interested in the response of the nematic order parameter to in-plane uniaxial strain, so will consider only the in-plane strain components:

$$\boldsymbol{\epsilon} = \begin{bmatrix} \epsilon_{xx} & \epsilon_{xy} \\ \epsilon_{yy} & \epsilon_{xy} \end{bmatrix} \tag{5.7}$$

Where ϵ_{xx} and ϵ_{yy} are pure tensile and compressive strain and ϵ_{xy} and ϵ_{yx} are pure shear.

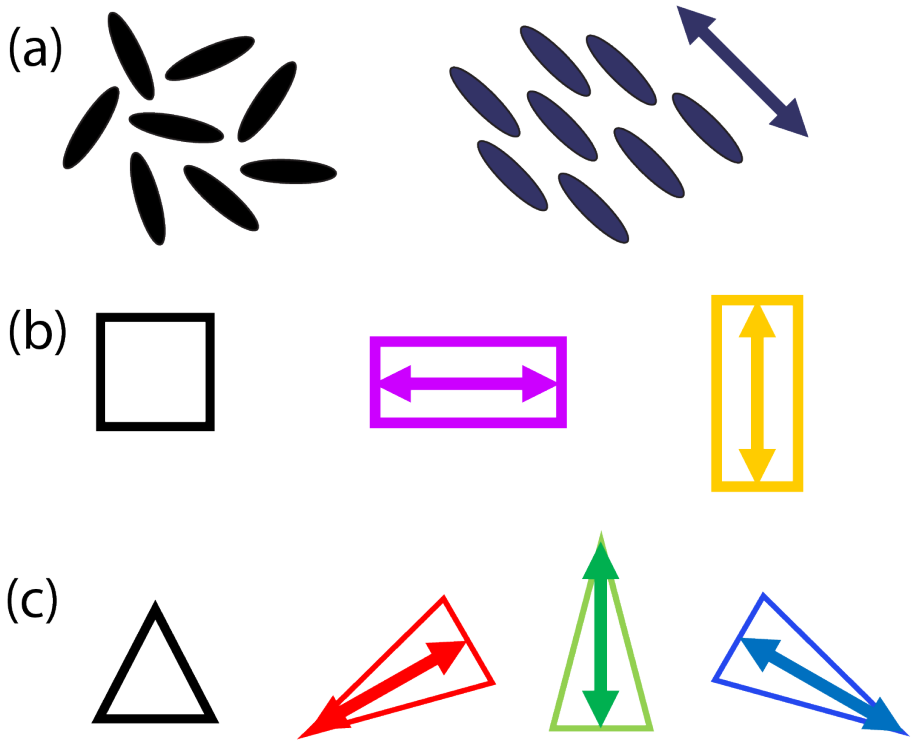

Figure 5.4: Cartoon depicting rotational symmetry breaking (a) Isotropic, disordered liquid crystals may be aligned at an arbitrary angle in the plane by an external perturbation. Nematic director is indicated by double headed arrow (b) Ising-Nematic: C_4 symmetric tetragonal crystal (black) undergoes a distortion which may result in two possible C_2 (purple and gold) structures. (c) Potts- or Z_3 Nematic: C_3 triangular crystal undergoes a distortion which may result in three possible C_2 (red, green, and blue) structures.

A neat group theory trick to understand how these elements behave in $Fe_{1/3}NbS_2$ is to group the components of the stain tensor into objects according to how they transform as the irreducible representations of the D_6 point group [144]:

$$\begin{aligned} v &= \epsilon_{xx} + \epsilon_{yy} \\ \boldsymbol{\mu} &= \begin{pmatrix} \epsilon_{xx} - \epsilon_{yy} \\ 2\epsilon_{xy} \end{pmatrix} \end{aligned} \tag{5.8}$$

Where v transforms as A_1 and $\boldsymbol{\mu}$ transforms as E_2. Recall that the nematic order parameter $\boldsymbol{\eta}$ also transforms as E_2, and hence $\boldsymbol{\eta}$ couples linearly to $\boldsymbol{\mu}$ in the Landau free energy expansion:

$$F = b[\boldsymbol{\eta} \cdot \boldsymbol{\mu}] = b[(\epsilon_{xx} - \epsilon_{yy})\eta_1 + 2\epsilon_{xy}\eta_2] \tag{5.9}$$

Where b is a coupling parameter between strain and nematic order. If a uniaxial strain of amplitude δ is applied along an angle α with respect to the x-axis, we can write the displacement vector:

$$\boldsymbol{u} = \delta(\delta x \cos\alpha + \delta \sin\alpha)(\cos\alpha\hat{x} + \sin\alpha\hat{y}) \tag{5.10}$$

and use 5.6 to extract the angular dependance of the strain tensor components:

$$\epsilon_{xx} = \delta\cos^2\alpha,\ \epsilon_{yy} = \delta\sin^2\alpha,\ \epsilon_{xy} = \delta\sin\alpha\cos\alpha \tag{5.11}$$

which substituting in to the free energy in Eq. 5.9 gives:

$$F = b\delta[(\cos^2 - \sin\alpha^2)\eta_1 + 2(\sin\alpha\cos\alpha)\eta_2] \tag{5.12}$$

Recalling the parameterization of the nematic order parameter $\boldsymbol{\eta}$ given in Eq. 5.3 and employing a handful of trigonometric identities, this simplifies to:

$$F = b\delta\cos(2(\theta - \alpha)) \tag{5.13}$$

Where $\theta - \alpha$ is the angle between the local nematic director and the applied strain. From this we can see that the linear coupling between nematic order and strain causes the nematic director to follow the direction of applied strain. In particular, whether the nematic director will tend to align with strain axes; whether it prefers to align to tensile or compressive strain depends on the sign of b. We will use this term again in Chapter 7, Section 4.

6

SCANNING BIREFRINGENCE MICROSCOPY

Optical polarimetry is a powerful probe of broken symmetries of crystalline materials. In ferromagnetic materials, the onset of magnetic order may be detected optically via the magneto-optical Kerr effect (MOKE), which is linear in magnetization, whereby a polarized beam of light will undergo a rotation of polarization upon reflection from the magnetic surface. MOKE has been measured for some AFMs which exhibit canting, and therefore are weakly ferromagnetic [147]. However, fully-compensated, collinear AFMs by definition have no net magnetization, and thus will not exhibit MOKE.

A weaker effect, quadratic in magnetization, which will result in rotation of polarization is the Voigt effect. Voigt rotation arises because there is a small birefringence, or difference in index of refraction n for light polarized parallel or perpendicular to the in-plane component of the Nèel vector. This effect was employed to image the Nèel vector orientation in CuMnAs in Ref. [148].

As $Fe_{1/3}NbS_2$ is a collinear c-axis AFM, we do not expect to observe rotation of polarization. Nonetheless, in this material we do observe a large, milli-radian scale rotation of polarization upon reflection which sets in abruptly at T_N and is independent of applied magnetic fields up to 400 G. In addition to the AFM order, structural distortion or local strain may lower the symmetry of the system, giving rise to an optical birefringence. In practice, optical methods used to study materials may be sensitive to a combination of these effects.

In the work presented in this thesis, we employ a spatially-resolved optical polarimetry technique (described below) to show that the onset of AFM order in $Fe_{1/3}NbS_2$ occurs simultaneously with the onset of optical birefringence via a first-order transition that breaks the 6-fold (screw) rotational symmetry of the paramagnetic phase.

In the following section, we will describe the experimental apparatus used in these measurements. Experimental results on $Fe_{1/3}NbS_2$ and accompanying theoretical advances will be discussed in detail in Chapter 7.

6.1 EXPERIMENTAL APPARATUS

Standard equilibrium (DC) birefringence measurements are typically done using a lock-in technique where single, linearly polarized laser beam is intensity-modulated by an optical chopper and is focused on to the sample surface. The reflected light is collected and the rotation of polar-

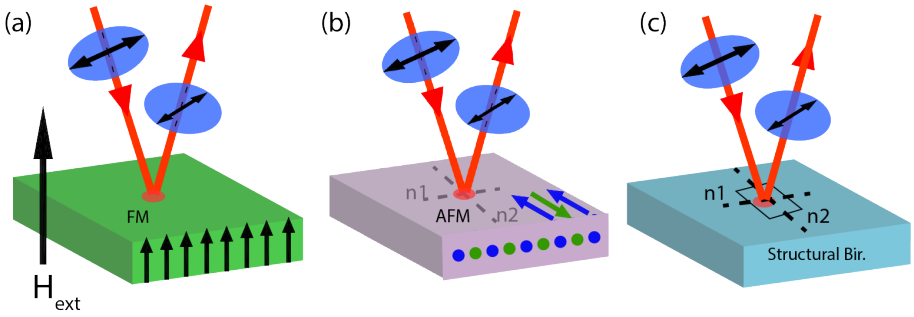

Figure 6.1: Cartoons of various optical effects which will result in rotation of linear polarization of a reflected laser beam (a) Polar Magneto-optical Kerr Effect in Ferromagnet (b) Birefringence resulting from in-plane component of Nèel order in an AFM (c) Birefringence resulting from a structure of C_2 symmetry

ization can be measured directly using a balanced optical bridge detector technique (described below).

The *DC* method is a straightforward and incredibly useful tool in detecting the onset of birefringence (or for ferromagnetic samples, MOKE). However this standard method single-beam is often subject to long period instabilities, as the polarization state may be affected by drifts resulting from birefringent optics in the set-up unrelated to the sample. This presents a challenge for the detection of weak optical birefringence effects and makes it challenging to perform polarization- spatially-resolved measurements which may take up to several hours.

To overcome these limitations, we employ a robust, thermally-modulated birefringence microscopy technique. To our knowledge this work was the first application of this thermally-modulated technique in conjunction with full polarization resolution and spatial imaging.

The significant difference from the *DC* technique is the introduction of a modulated 800 nm pump beam. The basic operating principle is that we exploit the magnetic phase transition to increase the measurement sensitivity. That is, in the vicinity of the T_N, the thermal modulation induced by the pump laser cycles the sample about the magnetic phase transition, therefore modulating the birefringence of the sample. A probe laser beam is overlapped with the pump and sent to an optical bridge detector. We lock-in to the modulation frequency of the pump. The resulting signal, which denote as $\Delta\phi$, is proportional to the temperature derivative of the sample birefringence in the region of pump and probe overlap, or $d\phi/dT$. This method minimizes the effects of long-term drift and is insensitive to birefringence in the setup not related to the magnetic transition, allowing us to measure rotations down to the sub-milliradian scale.

A schematic of our experiment is shown in Fig. 6.2. The pump light is provided by a 800 nm Titanium Sapphire oscillator (Coherent Vitara). Although this is a pulsed laser, note we do not measure ps-scale dynamics with this technique. Having the 800 nm pump is useful simply because it makes it possible to reject pump scatter in the detection of the the 632 nm probe by use of a color filter.

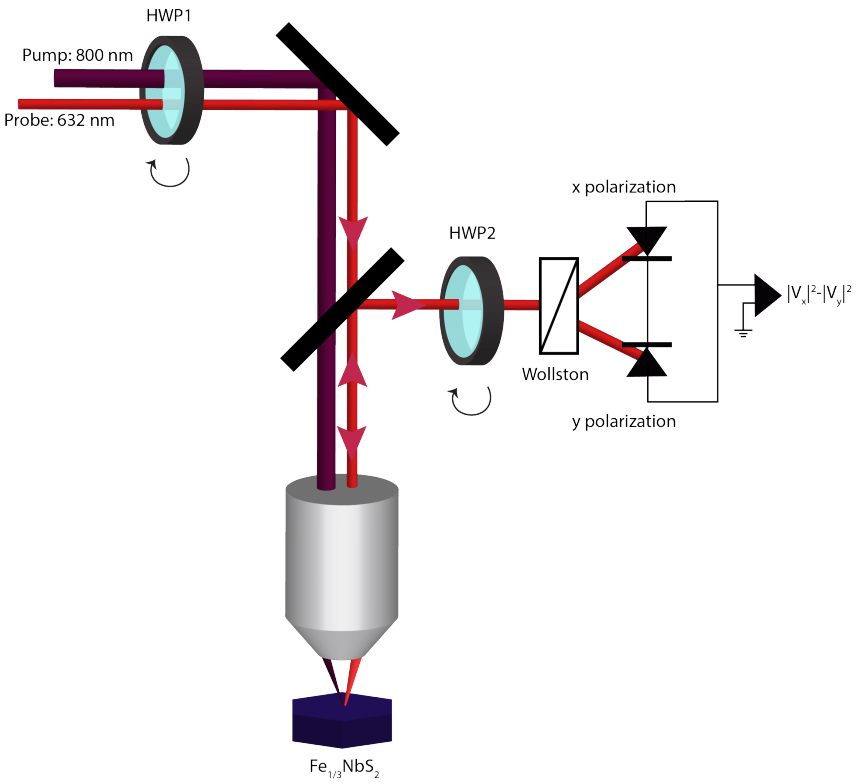

Figure 6.2: Schematic of Birefringence Microscopy set-up

The purpose of the pump, as mentioned, is instead to thermally modulate the sample. This is achieved by sending the pump through an optical chopper at 2 kHz and focused through a microscope objective onto the sample surface. When the pump beam is admitted, the sample temperature is raised by an incremental amount dependent on the pump power. When the pump is blocked by the chopper blade the sample temperature re-equilibrates to the lower temperature. In the vicinity of T_N, the pump heating cycles the sample about the magnetic phase transition, leading to a change in birefringence, $\delta\phi$.

Simultaneously, a linearly polarized 632 nm continuous wave HeNe probe laser beam is focused at normal incidence and spatially overlapped with pump. The polarization of the incident probe laser is set by a half-wave plate (HWP1) mounted in a stepper-motor rotation stage. Both pump and probe beams are focused by a 10x microscope objective and reflected off of the sample.

The pump reflection is rejected via a color filter while the reflected probe is sent through a Wollaston prism which spatially separates the horizontal (x) and vertical (y) polarization components of the beam. The two orthogonally polarized beams are sent to an optical bridge detector which simply consists of two unbiased commercial Si-photodiodes connected in parallel but with opposite polarity. The net photocurrent will be zero, or "balanced", when the x and y components have equal intensity. Balancing is achieved by warming the sample above the Nèel temperature and adjusting a second half-wave plate (HWP2), also mounted on a motorized rotation stage and controlled by a computer. The "balance angle" setting for HWP2 is found for a given input polarization angle as determined by HWP1.

When cooled below T_N, the sample enters the antiferromagnetic (AFM) phase and becomes birefringent, rotating the polarization of the reflected probe and unbalancing the detector. In general, the reflection amplitude of light from the sample surface is characterized by a 2×2 matrix, r_{ij}. For a material with C_3 or higher rotational symmetry, $r_{ij} = \delta_{ij} r$, and the polarization of the probe beam would remain unchanged upon reflection. For a birefringent sample with C_2 or lower rotational symmetry, the reflection matrix have different components along the diagonal, corresponding the different reflectivity along the principal optic axes a and b, and hence birefringence, $\Delta r = r_b - r_a$.

In our experiment, the intensity admitted to each of the two photodiodes upon reflection from a birefringent sample can be computed using Jones calculus,

$$\begin{bmatrix} V_x \\ V_y \end{bmatrix} = \begin{bmatrix} \cos\theta & -\sin\theta \\ \sin\theta & \cos\theta \end{bmatrix} \begin{bmatrix} r_a & 0 \\ 0 & r_b \end{bmatrix} \begin{bmatrix} \cos\theta & \sin\theta \\ -\sin\theta & \cos\theta \end{bmatrix} \begin{bmatrix} 1 \\ 1 \end{bmatrix} \tag{6.1}$$

where θ, set by the two half-wave plates, represents the angle between the incident probe beam polarization and the sample principal optic axes. The balanced diode detector measures the intensity difference between the two polarization components, $|V_1|^2 - |V_2|^2$, to first order in $\Delta r / \bar{r}$, where

$$\bar{r} = \frac{r_a + r_b}{2}, \quad \Delta r = r_a - r_b \tag{6.2}$$

we obtain the quantity we measure in optical bridge detection:

$$|V_1|^2 - |V_2|^2 = \mathrm{Re}\,(\bar{r}^* \Delta r)\cos 2\theta \tag{6.3}$$

This photocurrent signal is filtered and amplified by an SRS current to voltage pre-amp and subsequently demodulated by a Zurich Instruments lock-in amplifier. In a typical measurement the optical rotation stages containing the HWPs are controlled by custom LabView software. The HWPs co-rotate to maintain the correct balance angle as a function of probe input polarization angle. In principle, the offset between the two HWP angles should remain constant. However in practice due to different reflectivity for s-polarized vs. p-polarized light, and small ellipticity in the probe polarization induced by multiple mirror reflections, the correct offset to achieve balance varies as the HWPs are rotated. To account for this, we find the correct balance angles as a high temperature reference, as describe above, for HWP1 every angle from 0 to 90 (corresponding to 0 to 180 degrees linear probe polarization) in 15 degree steps.

With the correct balance angles, an angular scan at low temperature yields the modulated birefringence as a function of probe input polarization angle, $\delta\phi(\theta)$. By fitting an equation of the form of Eq. 6.3 to these scans, we can extract the orientation of the optic axes a and b at the locality of the beam spot.

To map the orientation of the birefringence across the sample area, we move the under the beam spot using piezo-actuated stages manufactured by Attocube. A full polarization scan of $\delta\phi(\theta)$ at each point on a grid shows how the optic axes change across the sample area, and in the case of $Fe_{1/3}NbS_2$, as discussed in the next chapter reveals three twin birefringent domains closely linked to the magnetic order.

We note that the measurements reported in this thesis, the limiting factor in spatial resolution is the spot size achieved by the objective, which is in the range of 5 to 10 μm. Note that because they are different colors, the pump and probe will have slightly different focal length and spot size with the same objective.

6.1.1 REDUCED-ELLIPTICITY MODIFICATIONS

A challenge specific to optical polarimetry measurements as described above is that a linearly polarized laser beam reflected from the mirrors and beam splitters will always become slightly elliptical. In general this can contribute to optical artifacts which modulate the data.

In the case of measurements on $Fe_{1/3}NbS_2$, the original set-up (Fig. 6.2) which did include some induced ellipticity in the probe beam was sufficient to make the observations reported here. This is because birefringence in these samples is large effect, and importantly, the observation is of three 120-degree birefringent domains which are oriented with respect to to the crystalline axes of the sample, rather than the axes of the lab. Such an observation cannot arise from artifacts related to the set-up.

Ellipticity in the probe beam may be reduced by modifying the set-up as show in Fig. 6.4 in which a pair of mirrors are placed in the incident and reflected beam paths of the experiment,

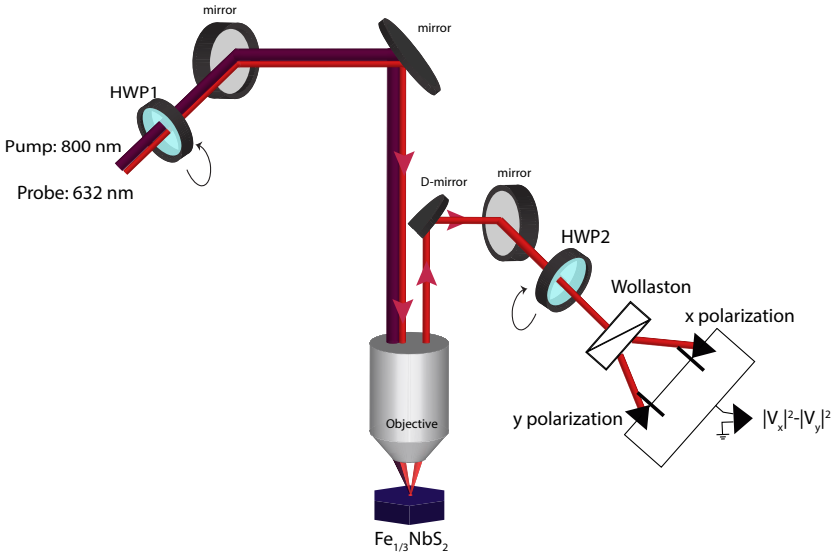

Figure 6.3: Schematic of photo-thermal modulation birefringence microscopy set-up with ellipticity-reducing modifications. In particular, additional mirrors are a D-mirror is used instead of a beam splitter

respectively. Here a horizontally polarized beam undergoes a p-like reflection followed by an s-like reflection, and vice versa for the vertically polarized beam. Similarly, a series of d-shaped and regular mirrors are mounted in the reflection path in order to cancel out ellipticities induced by the mirrors. We find that the polarization state is completely preserved after the reflections, regardless of the initial orientation of the polarization (s, p, or any intermediate polarization between the two).

Currently, the ellipticity reduced set-up, as depicted in 6.4 is installed in the lab and operated by Changmin Lee to study domain effects other magnetic materials.

6.1.2 MONTANA INSTRUMENTS 4 K CRYOSTATION

The high temperature- and spatial- resolution measurements reported in this thesis are enabled by our Montana Instruments Cryostation, which was installed in the lab in 2015. This is a cryo-free pulse-tube cooler based cryostat, were the sample chamber is vibrationally isolated from the cooler. Vibrations are specified to be around 50 nm, well below our spot size, enabling precise imaging capabilities [149].

Samples are typically mounted in N-grease to a thin copper plate. The sample plate is affixed to a temperature control stage (Agile Temperature Stage Mount, or "ATSM") which enables stable thermal cycling from the base temperature to 350 K with low position drift (specified 30 μm). The ATSM is controlled LakeShore PID controller and is thermally linked to the the cryostat through a copper flex link that is connected to the base plate. The ATSM mounted on

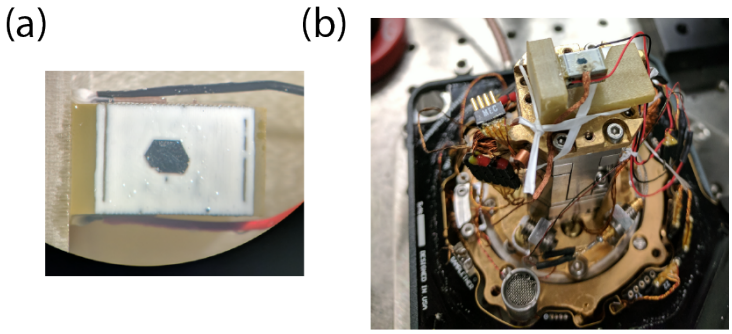

Figure 6.4: (a) Photo taken through microscope of $Fe_{1/3}NbS_2$ sample mounted to PZT stack. (b) PZT stack mount assembly installed in the Cryostation.

top of three piezo-actuated positioning stages (Attocubes) which control the x, y, and z positions of the sample.

A low working distance window assembly allows us to place an objective at a minimum working distance of around 4 mm. The objective used for the measurements presented here has a working distance of 10 mm.

6.2 STRAIN MEASUREMENTS

To apply strain (see Chapter 7, Section 4) the sample was glued using a thin layer of Stycast 1266 onto a piezoelectric (PZT) stack. Upon cooling, the PZT expands along its poling direction [150], which applies a small uniaxial strain of ≈ 0.1 percent [150, 151]. The orientation of the crystal axes relative to the poling direction of the PZT (direction of tensile strain upon cooling) is confirmed by Laue x-ray diffraction. The edge of the PZT stack is glued to a custom-machined L-shaped fiberglass part so that it may be free to move along the direction of expansion. Thermal linking of the sample and PZT to the temperature control stage is achieved by affixing copper wires with silver epoxy to the sample and clamping them in contact with the cryostat stage. This enables cooling of the sample well below T_N. However such a set up does not work for changing the temperature controllably in small steps. As a result the strain measurements presented here are recorded at a fixed sample base temperature, and at a fixed strain.

Because the sample is epoxied to the PZT for these measurements, the only way to access multiple strain orientations is to image the sample first before strain is applied, and then again after cleaving and remounting the top layers onto the PZT at 90 degrees. Location of the relevant imaging area after remounting of top layers is achieved by cross-referencing maps of the sample reflectivity taken in each configuration, shown in Fig. 6.5.

For future work, we plan to implement measurements which make use of a uniaxial strain device, similar to those described in [151]. The use of such a device will enable application of around an order of magnitude higher strains, and allow us to change the strain at a fixed tem-

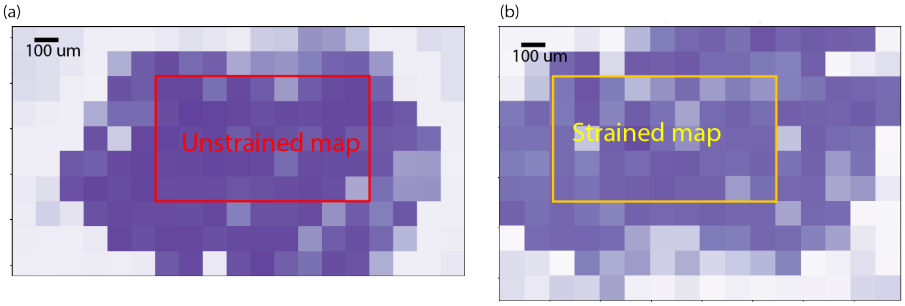

Figure 6.5: Reflectivity maps of the sample are used to cross-reference multiple measurements in different strain configuration. Colors cale: Purple indicates high reflectivity, white indicates low reflectivity (a) A roughly 2 mm × 1 mm image of the sample showing the sample (purple) and the surrounding area (white). Red box indicates the region imaged by birefringence microscopy. (b) Reflectivity image of the same sample now mounted to the PZT. Cross-referencing of this with (a) allows us to select region to image which overlaps with the birefringence map in (a).

perature. More information about the integration of a uniaxial strain device with the Montana Cryostation is presented in Appendix C.

6.3 SAMPLE GROWTH AND FE-INTERCALATION VALUES

For the measurements presented in this thesis, we studied single crystals that were grown by the James Analytis group at UC Berkeley using vapor transport techniques.

The samples for which the switching behavior were reported have a Fe-concentration close x=0.33 [8]. The samples studied with optics share the basic properties but have a slightly higher Fe-concentration; they were grown with a nominal Fe-concentration of x = 0.37. Energy-dispersive x-ray spectroscopy (EDX) and inductively coupled plasma (ICP) measurements were performed to verify the chemical composition, yielding an Fe-intercalation value of x = 0.34. The samples studied are hexagonal crystals 1-3 mm in size and 20 × 100 μm thick. X-ray diffraction and transmission electron microscopy measurements confirm the crystal structure is the nominal x =1/3 non-centrosymmetric space group $P6_322$. For brevity, we will refer to the samples simply as $Fe_{1/3}NbS_2$.

de

7

IMAGING OF POTTS-NEMATIC ORDER IN FE_XNBS_2

7.1 FIRST ORDER MAGNETIC-NEMATIC PHASE TRANSITION

First, we discuss the nature of the AFM transition phase transition in $Fe_{1/3}NbS_2$. Fig. 7.1 (a) shows transport and thermodynamic measurements on the same $Fe_{1/3}NbS_2$ sample used for optical studies. A singularity in heat capacity, C_p, coincides with abrupt jumps in the out-of-plane magnetic susceptibility, $\chi_\perp$ and the in-plane resistivity, ρ_{xx}, indicating a single, first-order transition to the AFM state at 43 K. We note that in the samples studied here, the in-plane susceptibility $\chi_{||}$ is negligible in comparison to $\chi_\perp$, indicating that the spins are primarily out-of-plane.[1]

Optical data is shown in Fig. 7.1 panels (b)-(e). Using the photo-thermal modulation technique (see Chapter 6) we probe rotation of polarization $\delta\phi$ as a function of temperature. The black trace in Fig. 7.1 (b) shows the sharp onset of birefringence at 49.5 K, indicative of rotational symmetry breaking. While both the optical and bulk probes show a single, sharp transition, optical probe detects the onset of order at a higher temperature than bulk probes do (around 43 K). These two transition temperatures are in fact consistent, and may be described by a model in which the ordered phase sets in at higher temperature at the sample surface than in the bulk, as will be discussed below.

As discussed in the previous chapter, the onset of optical birefringence results from the lowering rotational symmetry across the phase transition, leading to a reflection matrix with principal optic axes a and b. For $Fe_{1/3}NbS_2$ the space group is $P6_322$, which has a sixfold rotation C_{6z} (screw) symmetry. The onset of optical birefringence is consistent with the lowering of C_{6z} to C_{2z} across the phase transition.

In the symmetry-lowered state, the probe polarization is rotated through an angle $\phi \propto \cos 2(\theta - \theta_0)$, where $\theta - \theta_0$ is the difference between the input probe beam polarization and the principal axis direction. This is illustrated in Fig. 7.1 (c), which plots the measured $\delta\phi$ as a function of probe polarization angle in the vicinity of T_N. Fitting to these angular scans (see Section 7.2) allows us to us to determine the orientation of the optic axes in the magnetic (birefringent) phase.

1 As mentioned in Ch. 5, the sample studied here was found to have Fe-concentration x=0.34, while the sample studied in [8] was x= 0.33

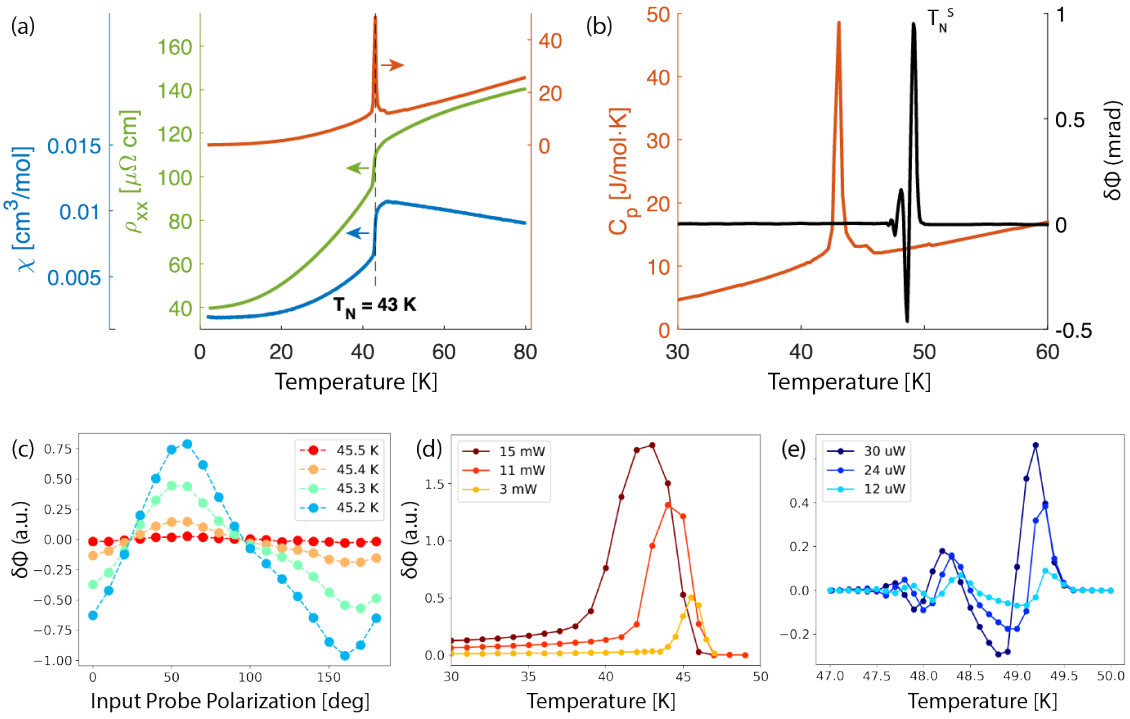

Figure 7.1: (a) Summary of bulk measurements on $Fe_{1/3}NbS_2$. Heat capacity (red) resistivity (green) and out-of-plane magnetic susceptibility (blue) all show a sharp first-order phase transition at $T_N = 43$ K (b) Optical data, $\delta\phi$ (black), for pump average power of 30 μW, shows a higher transition temperature $T_N^s = 49$K (c) $\delta\phi$ as a function of input probe polarization angle for temperatures in the range of the phase transition. The input polarization angle with the maximum $\delta\phi$ indicates the orientation of the fast optic axis. (d) $\delta\phi$ vs. T in the high pump power regime, where the transition is thermally broadened by the pump. (e) $\delta\phi$ vs. T in the low pump power regime, where oscillations resulting from surface nucleation of the nematic phase are evident.

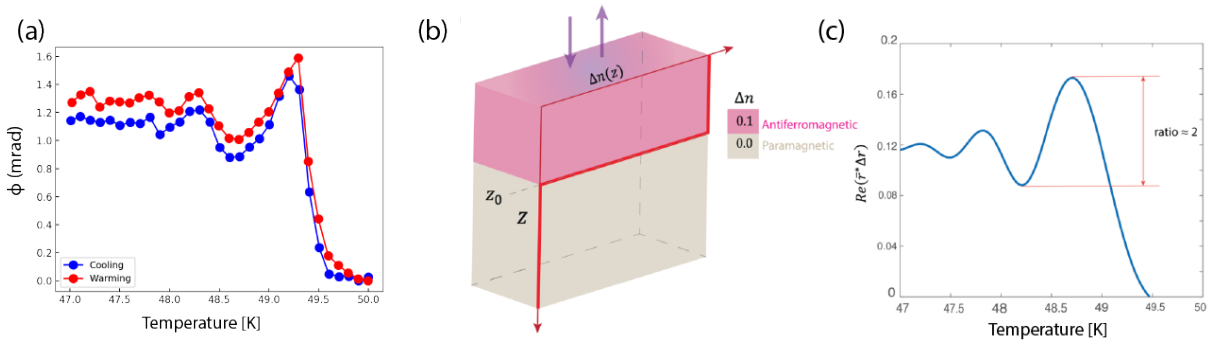

Figure 7.2: (a) *DC* birefringence data exhibits oscillations at temperatures slightly below the surface T_N. (b) Illustration of a sharp, shifting interface between the AFM phase (pink) where δn=0.1 and the paramagnetic phase (beige) where δn =0. (c) Result of calculation of measured optical birefringence for a sharp interface. Panels (b) and (c) were made by Wenqin Chen.

We now address the apparent discrepancy in transition temperatures as measured by bulk and optical probes may be resolved by considering the the decaying oscillations in $\delta\phi$ which appear in the optical data when the pump power is lowered by roughly two orders of magnitude.

The photo-thermal modulation technique necessarily involves some heating from the pump laser pulse, which artificially shifts T_N to lower temperature and thermally broadens the peak in $\delta\phi$. Fig. 7.1 shows $\delta\phi$ for three pump powers in the high pump regime. For example, an average pump power of 15 mW artificially broadens the transition to appear to have a width of nearly 10 K. Fig. 7.1 (e) $\delta\phi$ when the pump power is lowered to 30 μW. In this low pump-power regime, the the onset of birefringence is shifted up to 49.5 K, and damped oscillations in $\delta\phi$ on a sub-Kelvin scale are resolved. Note the expanded temperature scale in Fig. 7.1 (e); the transition is saturated within 2 K of the onset of birefringence.

We can confirm that these oscillations are not the result of an artifact of the photo-thermal modulation technique by measuring the $\phi(T)$ directly– that is, reproducing the effect in a *DC* (no pump laser) birefringence measurement. As shown in Fig. 7.2 (a), the oscillations and higher transition temperature are reproduced in the static measurement, where the high signal-to-noise of this data is achieved by averaging six consecutive scans. Fig. 7.2 (a) also demonstrates the lack of hysteresis in the transition.

The oscillations in $\delta\phi$ may be described by a model in which the the symmetry-broken AFM phase sets in on the sample surface at a higher temperature (T_N^s) than in the bulk, and propagates in to the sample bulk as the temperature is decreased. A simple cartoon illustrating this scenario is presented in Fig. 7.2 (b), where the a sharp interface between AFM (pink) and the paramagnetic bulk (beige).

For temperatures below the surface transition temperature $T_N^s = 49$ K, this buried interface separates the birefringent AFM surface layer from the isotropic bulk. As the depth, Z, of the interface increases with decreasing T, the phase difference between the reflections from the

surface and the buried interface produces the interference pattern seen in $\phi(T)$. These Fabry-Perot-like oscillations are cut off when the buried interface reaches beyond the penetration depth of the probe beam, which is approximately 150 nm [126]. At this depth, T_N (Z) has reached 47.5 K, which is still 4.5 K higher than the bulk T_N.

A calculation of $\phi(T)$ for this sharp-interface model is show in Fig. 7.2 (c), which qualitatively reproduces the oscillations observed in panel (a). For the purposes of the calculation, in the paramagnetic region we assume an isotropic index of refraction given by $n = 2.6 + 0.6i$, the value measured for the similar compound $Fe_{1/4}TaS_2$ in Ref. [126]. The AFM surface region has a birefringence characterized by the difference in index of refraction along the optic axes, where $\Delta n = n_a - n_b$. A better still fit to the data may be achieved by altering the calculation to include a smooth interface with a finite width between the AFM surface and the disordered bulk. The details of this calculation are included in the Supplementary Material for Ref. [30].

While this observation may seem surprising at first, we note that onset of nematic order on the surface at a higher temperature in the bulk has been observed in other materials systems [152]. In particular, time-resolved pump probe birefringence measurements on the Fe-pnictide superconductors performed in our lab [141] showed the onset of nematicity at a higher temperature than measured in bulk. An offset of several degrees in transition temperature between the surface and bulk in pnictides was confirmed by Ref. [153]. In that work, the bulk transition and surface transition are simultaneously through a combination of optical birefringence and a unique quantum gas microscope probe.

This observation of oscillations in our low-power optical measurements opens up interesting possibilities for studying such phenomena. In general, the mesoscopic scale of the probe wavelength enables a new method for profiling the depth of transition region as a function of temperature on a 10-nm scale.

7.2 IMAGING OF BIREFRINGENT DOMAINS

We now turn to the spatial mapping of the amplitude and principal axis directions of the nematic order. Mapping is achieved by cooling the sample below T_N and measuring $\delta\phi$ as a function of probe polarization angle (as in Fig. 7.1(c)) at each spatial point on a grid as the sample is rastered beneath the laser spot.

As mentioned previously (6.3), in the birefringent phase we expect angular scans of $\delta\phi$ to have a $\cos(2\theta)$ periodicity with input probe polarization. In practice, the data shown in Fig. XX (and in Fig. 7.1(c)) were fit to:

$$\delta\phi(\theta) = A\cos 2(\theta + \theta_0) + B\cos(4\theta) + C \tag{7.1}$$

Where θ_0 is the local orientation of the principal optic axes and A, B, and C are constant fit parameters. Weak residual birefringence in the optical set-up as well as a small modulation of the probe laser power as a function of polarization lead to an additional modulation of the data which appears as a small $B\cos(4\theta)$ term and a small offset, C. In general these effects are small

compared to $\cos(2\theta)$ component, and we can reliably extract the the domain orientation and birefringence amplitude from the parameters θ_0 and A in the fitting function in 7.1.

Across the sample area, we detect three distinct orientations of optic axes offset by $2\pi/3$ from each other, and hence three major domains, as illustrated by representative polar plots of $|\delta\phi(\theta)|$ taken at three locations on the sample in Fig. 7.3 (a).

By registration of the optical data with a x-ray Laue diffraction pattern taken on the same sample, we find that the three orientations of optic axes correspond to the three crystallographic symmetry directions of the triangular Fe-lattice Fig. 7.3 (b). For illustrative purposes, we assign a color to each of the orientations, such that [100] is red, [010] is green, and $[1\bar{1}0]$ is blue.

A map of a 900 μm $\times$ 500 μm region of the sample is shown in Fig. 7.3 (c) and (d), revealing the presence of all three domains, which can be as large as hundreds of microns or as small as our resolution of about 10 μm (the laser spot size is between 5 and 10 μm). Domains in this sample are large and as such for the region imaged here optical data are sampled 50 μm steps. All three domains are well-represented within the area imaged (Fig. 7.3 (c) inset). We find the domain distribution is deterministic upon warming and cooling, and does not change in magnetic fields up to 400 G.

This observation of three birefringent domains in which the orientation of the symmetry-breaking registers with the high symmetry directions of the Fe-Fe superlattice, in combination with the fact that birefringence sets in at T_N motivates our interpretation of these effects as resulting from a simultaneous magnetic-nematic first-order phase transition. Quantitatively, the observed rotational symmetry breaking results from an in-plane distortion which is coupled to the magnetism and selects the ordering wave-vector of the AFM ground state. A theoretical discussion of these results are presented in the following section.

7.3 THEORY

The nematic order that accompanies the onset of AFM order in $Fe_{1/3}NbS_2$ can be understood to result from the geometric frustration of Ising spins [116, 117] on the triangular ($\sqrt{3}a \times \sqrt{3}a$) superlattice of Fe atoms (Fig. 7.3 (b)). Qualitatively, a distortion along one of the three directions of Fe-Fe bonds breaks the 3-fold rotation symmetry of the equilateral triangle, thereby relieving the geometric frustration of the Ising spins allowing one of three degenerate magnetically ordered phases to condense. Across the entire crystal, in the absence of an external training field, this will result in three domains whose principal optic axes are aligned with the three Fe-Fe bond directions, as shown in Fig. 7.3.

First we will consider possible magnetic ground states and develop a phenomenological Landau model for $Fe_{1/3}NbS_2$ which shows that the simultaneous magnet-nematic phase transition may be described in the terms of a Z_3 Potts-nematic.

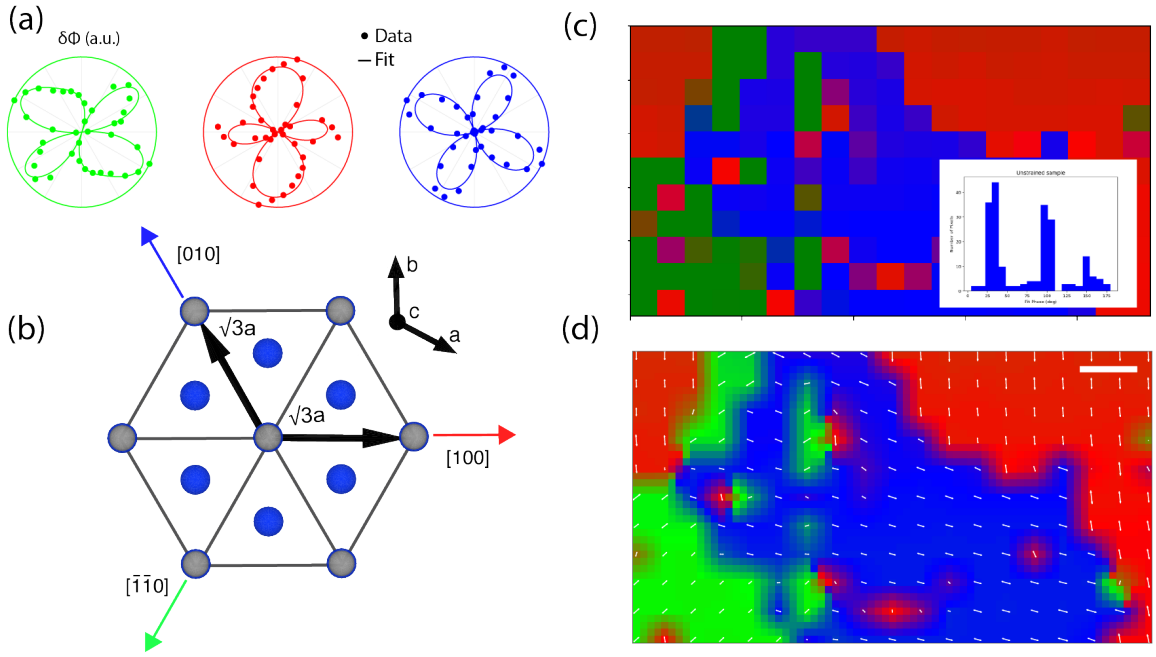

Figure 7.3: (a) Representative angular scans of $\delta\phi$ taken at three different spatial locations on the sample, showing three 120-degree orientations of principal optic axes. (b) View of crystal structure cut along the c-direction, illustrating the three domain orientations with respect to the Fe-Fe superlattice. (c) Birefringence map across a 900 $\mu m \times$ 500 μm region of the sample, sampled in 50 μm steps which each step indicated by a single pixel. Pixel color refers to domain orientation. Inset: Histogram showing the number of optic axes orientation vs. number of pixels, revealing three distinct domains. (d) Same birefringence map presented in (c), but with interpolation between points sampled by the measurement. White arrows plotted at each measurement point illustrate the local domain orientation and birefringence amplitude.

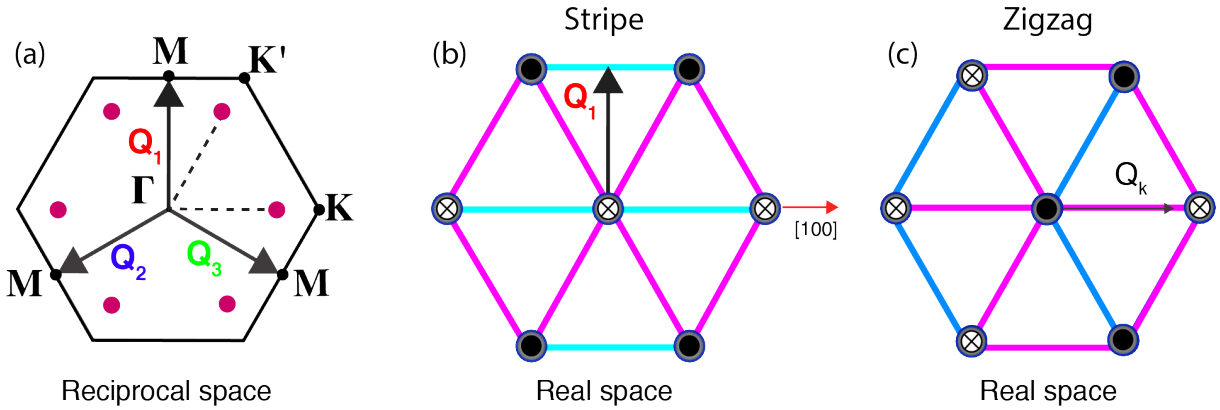

Figure 7.4: (a) Brillouin zone of the triangular Fe-lattice, showing the relevant wavevectors for the possible magnetic ground states. (b) Real space c-axis view of a Fe-layer illustrating of stripe magnetic order for the Q_1 domain. Solid black dots indicate spin up, crosses indicate spin down. Blue bonds connect aligned spins, pink bonds connect anti-aligned spins. (d) Illustration of zigzag order for one of six possible domains.

7.3.1 MAGNETIC GROUND STATE

Contemporary, direct measurements of the magnetic ground state on this material have yet to be published, however, the fact that we optically detect precisely three birefringent domains provides some constraints on its form. Existing neutron data from the 1970s [125] indicated a Wurzite-type ("magnetic ordering of the third kind") structure with spin moments along the c-axis. The wurzite scheme the spin of a single Fe-atom is parallel to 4 out of the 12 nearest-neighbors, and anti-parallel to the other 8 spins.

With this in mind, we consider that in general for the triangular lattice, there are two sets of wave-vectors along the high symmetry directions, Γ - M and in the direction of Γ - K, which may give rise to three nematic domains as are observed by our optical measurements. The first Brillouin Zone for the triangular lattice and associated symmetry directions are illustrated in Fig. 7.4.

First, we consider wavevectors along Γ - M, which are as drawn here given by $Q_1 = \pi/\sqrt{3}(0,2)$, $Q_2 = \pi/\sqrt{3}(-\sqrt{(}3),1)$, $Q_3 = \pi/\sqrt{3}(\sqrt{3},-1)$, and are illustrated by black arrows in Fig. 7.4(a). These are related by three-fold rotation, that is $Q_1 + Q_2 + Q_3 = 0$. The resulting magnetic state is a stripe order with three possible orientations, one of which is illustrated in Fig. 7.4 (b).

Now we consider magnetic states generated by ordering wavevectors in the direction of Γ - K. We write "in the direction" because unlike the M-points discussed above, the points K and K′ are related by an inversion and thus there are only two independent wavevectors, $\boldsymbol{K} = \pi/\sqrt{3}(0,2)$ and $\boldsymbol{K}' = \pi/\sqrt{3}(1,2)$. Ordering with precise Γ - K wavevectors cannot result in three domains. However, a zigzag state (Fig. 7.4 (c)) may be generated by shorter wave vectors connecting Γ to the six magenta points along the K-directions indicated in Fig. 7.4 (a).

This possibility is important to consider because this zigzag phase is also consistent with Wurtzite-type order and with our optical measurements. The key difference being that the formation of a zigzag state completely lowers the point group symmetry of the parent $Fe_{1/3}NbS_2$ lattice from C_6 to C_1. That is, in the zigzag phase there are 6 distinct domains defined by the six possible wavevectors in 7.4 (a). However, our optical birefringence probe is based on the linear polarization of light, which is equivalent under 180-degree rotations. Hence we are sensitive to at most C_2 symmetry. As such, sets of six distinct zigzag domains related by a C_2 rotations will produce the same orientation of principal axes as detected by optical birefringence, giving rise to only three detectable domain orientation This is indeed a possibility consistent with our measurements.

Thus, from our optical measurements it is not possible to distinguish between the stripe and zigzag orders. In the following, we discuss a free energy theory with the stripe case as a starting point, as it is the simpler case. From a theory standpoint, we do find that both possibilities of magnetic ground state explored here give rise to a magnetic-nematic phase transition. Calculations specific the zigzag state may be found in the supplementary information for [30].

7.3.2 LANDAU THEORY

Landau theory for 3-state Potts nematicity in $Fe_{1/3}NbS_2$ was developed by our collaborators Jörn Venderbos and Rafael Fernandes.

Having established possible magnetic ground states, we may gain further insight into the nature of the transition by constructing a phenomenological Landau model. Here, we assume stripe order. We introduce three order parameters L_1, L_2, and L_3 whose wavevectors are parallel to each of the three Γ - M directions respectively. Spin-rotational and 6-fold rotational symmetries restrict the corresponding magnetic Landau free-energy F_M to the form:

$$F_M = a \sum_{i=1,3} L_i^2 + v_0 \left(\sum_{i=1,3} L_i^2 \right)^2 + v_1 \sum_{i<j} L_i^2 L_j^2 + v_2 \sum_{i<j} \left(L_i \cdot L_j \right)^2 \tag{7.2}$$

For simplicity, here we assume commensurate wavevectors, but the results can be extended in a straightforward way to incommensurate order. The Landau coefficients v_1 and v_2 determine the nature of the magnetic state below the N el temperature. In particular, for $v_1 > 0$ and $v_2 > -v_1$ a single-Q magnetic state is favored in which only one of the L_i is nonzero and rotational symmetry is broken. In contrast, other parameter values lead to equal amplitude triple-Q magnetic ordering, preserving the rotational symmetry of the paramagnetic state. While the particular values of these and the other Landau coefficients a and v_0 depend on microscopic considerations related to the mechanism responsible for the magnetic instability, for our purposes a phenomenological approach suffices.

Indeed, our experimental observation of rotational symmetry breaking points uniquely to single-Q AFM order in $Fe_{1/3}NbS_2$(i.e. $v_1 > 0$ and $v_2 > -v_1$), in which $\langle L_i \rangle \neq 0$ for one of the three order parameter components. As seen in Fig. 7.4, the six nearest-neighbor links are

no longer equivalent in the stripe AFM state; four bonds couple anti-parallel spins whereas two bonds couple parallel spins. This rotational symmetry breaking is captured by an order parameter $\boldsymbol{\eta} = (\eta_1, \eta_2)$, which is given in terms of the magnetic components as,

$$(\eta_1, \eta_2) = \left(\boldsymbol{L}_1^2 + \boldsymbol{L}_2^2 - 2\boldsymbol{L}_3^2, \sqrt{3}\boldsymbol{L}_1^2 - \sqrt{3}\boldsymbol{L}_2^2 \right) \tag{7.3}$$

Here $\mathbf{n}$ is a nematic director indicative of rotational symmetry breaking and can be parameterized as $n = n(\cos 2\theta, \sin 2\theta)$. The structure of $\mathbf{n}$ for the triangular lattice contrasts sharply with nematic order in tetragonal systems such as the Fe-pnictides, which is described by a single-component Z_2 Ising-nematic order parameter [137, 140]

The magnetic free energy Eq. 7.2 can be used to derive an effective free energy F_η for nematic order, since the nematic order parameter $\boldsymbol{\eta}$ is a composite magnetic order parameter. The details of this calculation may be found in the Supplementary Materials for [30]. Integrating out magnetic fluctuations and going beyond mean-field theory, one finds,

$$F_\eta = \alpha\boldsymbol{\eta}^2 + \beta\boldsymbol{\eta}^3 \cos 6\theta + \gamma\boldsymbol{\eta}^4 \tag{7.4}$$

where the Landau parameters α, β, and γ depend on the Landau parameters of the magnetic free energy, Eq 7.2. The key observation is that in Eq. 7.4 we recover Eq. 5.4; it is same free energy as that of the 3-state Potts model. [145, 146] This implies that $\mathbf{n}$ is a Z_3 Potts-nematic order parameter. Note that, because of the positive coefficient in the cubic term of Eq. 7.4, the free energy is minimized by one of the three values $\theta = \pi/6, \pi/2, 5\pi/6$.

The existence of this cubic coefficient implies that, in three dimensions, the Potts-nematic transition is mean-field and first-order. This opens up the possibility of a first-order Potts-nematic and magnetic transition, the jump in $\boldsymbol{n}$ triggers a jump in the magnetic correlation length and a simultaneous first-order nematic-AFM transition consistent with the data.

7.4 STRAIN TUNING OF DOMAIN POPULATION

We may test these ideas by observing how the system responds to an external perturbation which couples to the nematic director. As we saw in Chapter 5, one such perturbation is uniaxial strain Here, we show that the relative population of the three AFM domains can be tuned in response to strain.

First we consider the low-strain configuration. The birefringence map shown in Fig. 7.3 (c) and (d) was obtained with the sample affixed to a copper plate by only by vacuum grease, a configuration in which the external strain from thermal contraction is small and not along a particular axis. In this low-strain configuration, all three domains are comparably represented, as illustrated in the histogram inset to Fig. 7.3 (c).

To apply strain, the same sample was glued onto a piezoelectric stack, which upon cooling applies a uniaxial strain of around 0.1 percent. For the first strain configuration (Fig. 7.5 (a)) the sample is glued to piezo such that the piezo poling direction is antiparallel to an Fe-Fe

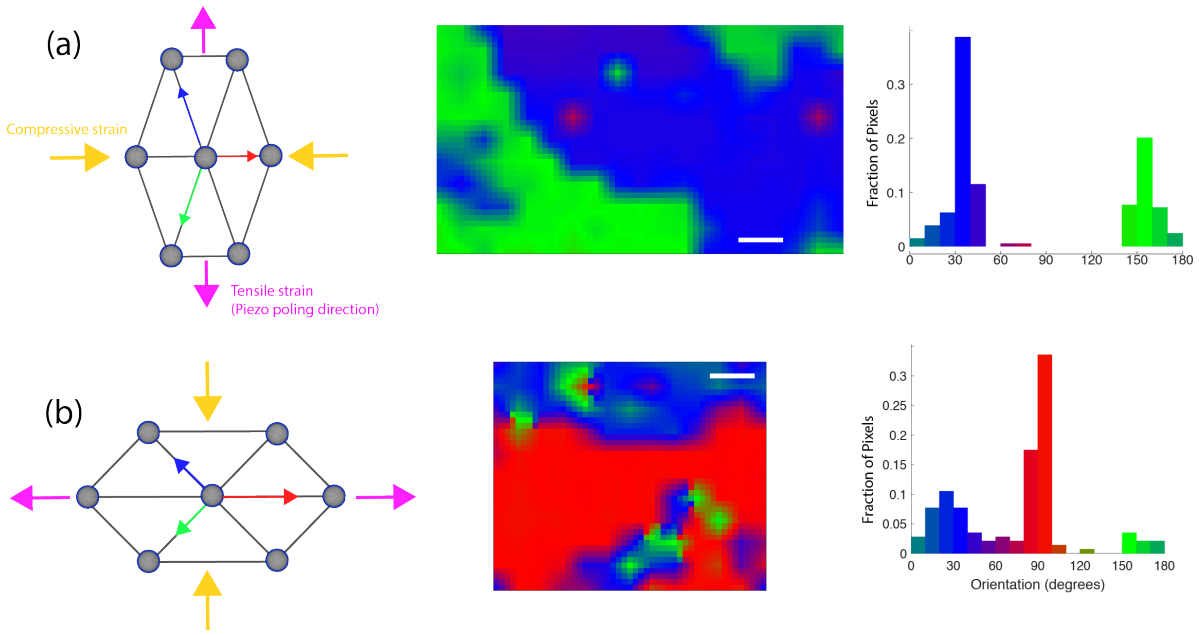

Figure 7.5: Domain population tuning through applied uniaxial strain (a) Illustration of first strain configuration with tensile strain applied perpendicular to the Fe-Fe bond, and compressive strain along a bond. In the resulting birefringence map, the blue and green domains are selected while the red domain is suppressed. (c) Strain configuration with sample rotated 90 degrees from (a). Red domain is selected and blue and green domains are suppressed.

bond. As the piezo is cooled to low temperature, the stack expands, applying tensile strain perpendicular to the Fe-Fe bond, and compressive strain along a bond.

We then locate and image the same region of the sample as was measured to produce the low-strain map in Fig. 7.3. The birefringence map with tensile strain perpendicular to a Fe-Fe bond is shown in Fig. 7.5 (a). This map, together with the domain histogram shows that the areal fraction of the red [100] domains, whose principal axes are parallel and perpendicular to the bond direction, and therefore aligned with the strain axes, is strongly suppressed and redistributed to green and blue domains.

To access the orthogonal configuration, with tensile strain applied along the bond direction, we cleaved and removed the top layers as the sample base is permanently affixed to the piezo. The top layers were then rotated by 90 degrees and re-mounted to the piezo, such that now tensile strain is applied in the bond direction (Fig. 7.5 (b)). As the optical penetration depth is only around 150 nm, the top layers are sufficient to image the same subset of sample. In the cleaving process, the sample edges were inevitably damaged, leaving a smaller area suitable for imaging. As a result the map in Fig. 7.5 (b) covers a slightly smaller area. Nonetheless, the resulting map shows that in this orientation, the areal fraction of the red domains grows at the expense of the green and blue domains.

The repopulation of nematic domains in response to strain follows in a straightforward fashion from the coupling of the strain tensor to the Potts-nematic order parameter, $\boldsymbol{\eta}$ (Eq. 7.4). As we showed in Chapter 5, $\boldsymbol{\eta}$ couples linearly to strain– tensile strain acts as a positive nematic conjugate field oriented parallel to the strain direction, favoring the domain corresponding to this direction. On the other hand, compressive strain acts as a negative conjugate field, which suppresses the corresponding domain and favors the other two domains.

These observations suggests a mechanism for switching and memory phenomena in response to in-plane perturbations, which in addition to strain may include magnetic fields $\boldsymbol{B}$ and currents, $\boldsymbol{J}$. In effect, the coupling of the Z_3 nematic and resulting domain repopulation enables the global symmetry axes of the bulk crystal to continuously follow the direction of an in-plane perturbing field. This is despite the locking of the Nèel vector perpendicular to the plane.

We may see this effect arise by considering a simple Landau model describing the repopulation of the Z_3-nematic domains under uniaxial strain. We can write a free energy, F_s , that contains two symmetry-allowed terms,

$$F_s = \left[(x_1 - x_2)^2 + (x_2 - x_3)^2 + (x_3 - x_1)^2\right] - b\sum_{i=1}^{3} x_i \epsilon \cos 2\left(\theta - \theta_n\right) \tag{7.5}$$

The first term favors equal domain populations whereas the second represents the linear coupling of the nematic order parameter to strain, which breaks the degeneracy of the three domains. Here x_i is the areal fraction of the i^{th} domain, b is the strain-nematic coupling parameter, ϵ is the amplitude of the uniaxial strain, $\theta - \theta_i$ is angle of the strain with respect to the director of domain n, and $\theta_i = 2\pi n/3$.

Using the constraint $\Sigma x_i = 1$ (all of the crystal is ordered, in one of the three domains) and linearizing with respect to $\delta_i = x_i - 1/3$, we find that F_s is minimized for $\delta_i = (3b\epsilon/4)\cos 2(\theta - \theta_i)$.

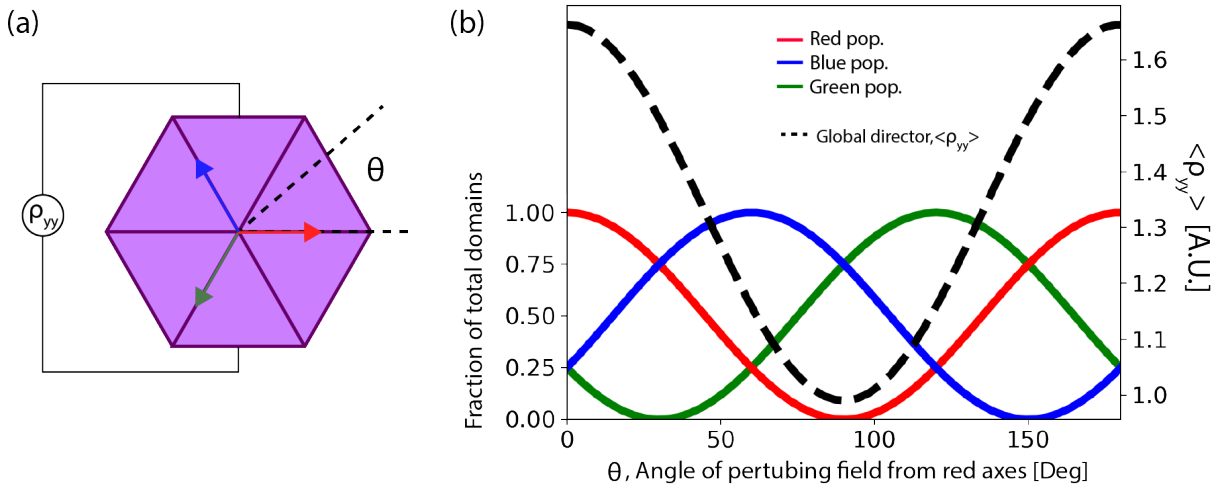

Figure 7.6: (a) Hypothetical measurement set-up, where fixed contacts measure parallel resistivity, ρ_{yy}, along one of the axes of the red domain. Real-space ordering wavevectors of the three domains with respect to the Fe-Fe bonds are indicated by colored arrows. An external field such as strain, $\boldsymbol{B}$ or $\boldsymbol{J}$ is applied at an angle θ with respect to the red domain axis. (b) Left axis: Calculation of fractional domain populations as a function of perturbing field angle θ. Right axis: Black dashed line shows $\langle\rho_{yy}\rangle$ with the arbitrary assumption ρ is maximal when measured along the axis of a domain. The global nematic director and hence $\langle\rho_{yy}\rangle$ continuously follows the direction of the perturbing field.

The model predicts that for tensile strain along a bond, the domain aligned with the strain grows according to $\delta_1 = 3b\epsilon/4$, while the other two shrink, $\delta_2 = \delta_3 = -3b\epsilon/4$. The signs of the δ_i are reversed for tensile strain perpendicular to the bond direction.

As an indicator of the global symmetry, we consider the bulk resistivity anisotropy tensor, $\overleftrightarrow{\boldsymbol{\rho}}_i \equiv R_{\theta_i}\Delta\rho\sigma_z$ where R_{θ_i} is the rotation operator and $\delta\rho$ and σ_z are the resistivity anisotropy and the Pauli z matrix, respectively. We assume that the global symmetry axes align with the spatial average tensor, $\langle\overleftrightarrow{\boldsymbol{\rho}}\rangle$. At equilibrium, all three domains are equally populated ($x_i = 1/3$) and $\langle\overleftrightarrow{\boldsymbol{\rho}}\rangle$ is a null tensor, corresponding to a globally isotropic system. However, an external field applied at an angle θ unbalances the domain population, in which case,

$$\langle\overleftrightarrow{\boldsymbol{\rho}}\rangle \propto \Delta\rho \begin{bmatrix} \cos 2\theta & \sin 2\theta \\ -\sin 2\theta & \cos 2\theta \end{bmatrix} \tag{7.6}$$

which shows that rotational symmetry is broken and the global symmetry axis continuously follows the direction of the perturbation. That is, the unbalancing of the domain population, results in a resistivity tensor whose principal axes continuously follow the direction of the perturbing field. An illustration of this effect is shown in Fig. 7.6. This is in stark contrast with

the Z_2-Ising-nematic system where the global anisotropy axes are the locked to the crystal axes, regardless of the direction of an external perturbation.

This analysis suggests an alternative, and perhaps complimentary mechanism for resistance-switching and magnetic memory effects in $Fe_{1/3}NbS_2$. In this case, the nematic director $\boldsymbol{\eta}$ can couple to perturbing fields such as $\boldsymbol{B}$ or $\boldsymbol{J}$, playing the same role as the in-plane Nèel vector, $\boldsymbol{L}$ does in the easy-plane systems such as CuMnAs and MnTe.

7.5 CONCLUSIONS AND OUTLOOK

In conclusion, we have shown that the onset of AFM order in $Fe_{1/3}NbS_2$ occurs via a first-order transition that lowers the rotational symmetry of the triangular lattice from 6 to at most 2-fold resulting in optical birefringence.

We implemented a novel scanning photo-thermal birefringence microscopy technique, which allowed us to image the orientation of principal optic axis across the sample area. In $Fe_{1/3}NbS_2$ below T_N, maps of local birefringence reveal three domains, characterized by in-plane nematic directors with relative angles $2\pi/3$. By considering a symmetry-based free energy model, we show that a the first-order nature of this transition may be understood in terms of a three-state Potts model where the symmetry-breaking order parameter is a Z_3 nematic, which in turn is a composite magnetic order parameter.

By integrating our measurements with applied strain we demonstrated that the relative population of Z_3 nematic domains can be controlled by an external field. In principle, the coupling of external perturbations to the nematic director could mediate the low-current threshold resistive switching behavior observed in $Fe_{1/3}NbS_2$ even if the Nèel vector is primarily out of plane. The observations and theoretical description presented here open the door for future work investigating AFM switching phenomena, as well as describing nematic orderer in nematic-magnetic systems with 6-fold symmetry [118].

On the technical front, this work presents of a demonstration of a new imaging technique may be used to investigate domain formation in other materials. Typically, AFM domains are imaged using techniques based on dichroism [154, 155], for example X-ray magnetic linear dichroism photoemission electron microscopy (XMLD-PEEM) imaging. Without a doubt, this is an extremely powerful technique– X-rays offer sub-micron resolution and normally beam lines are configured to explore different angles of incidence and etc. In comparison, our birefringence microscopy technique may lack in resolution but our ability to scan the probe polarization through the full 180 degrees allows image the optic axes, as opposed the dichroism (i.e., the difference in response between two orthogonal polarizations). In principle, in the contrast images produced by dichroism techniques three nematic domains we observed in $Fe_{1/3}NbS_2$ would not be distinguishable.

An aside for interested future researchers: We did try XMLD measurements on $Fe_{1/3}NbS_2$. We were able to measure the Fe absorption edge in these samples, even though the iron concentration is somewhat dilute. The trick to getting the absorption edge, we found, was to cleave the samples.

Unfortunately that day there was an artifact in the data which prevented us from detecting dichroism.

Finally we note that the microscopy set-up described here is a relatively modular system, which can be integrated with other techniques including transport and applied strain. Future plans include the integration of a uniaxial strain device (see Appendix C) into this set-up such that strain may be tuned controllably to at low temperature to measure changes in the transition temperature or even image motion of domain walls in response to applied strain.

BIBLIOGRAPHY

[1] Rayen Welch Tyler. The magnetic susceptibility of MnO as a function of the temperature. *Physical Review*, 44(9):776, 1933.

[2] Heung-Sik Kim, Andrei Catuneanu, Hae-Young Kee, et al. Kitaev magnetism in honeycomb α-$RuCl_3$with intermediate spin-orbit coupling. *Physical Review B*, 91(24):241110, 2015.

[3] Jeffrey G Rau, Eric Kin-Ho Lee, and Hae-Young Kee. Spin-orbit physics giving rise to novel phases in correlated systems: Iridates and related materials. *Annual Review of Condensed Matter Physics*, 7:195–221, 2016.

[4] G Jackeli and G Khaliullin. Mott insulators in the strong spin-orbit coupling limit: from Heisenberg to a quantum compass and Kitaev models. *Physical review letters*, 102(1): 017205, 2009.

[5] Christian Balz, Paula Lampen-Kelley, Arnab Banerjee, Jiaqiang Yan, Zhilun Lu, Xinzhe Hu, Swapnil M Yadav, Yasu Takano, Yaohua Liu, D Alan Tennant, et al. Finite field regime for a quantum spin liquid in α- $RuCl_3$. *Physical Review B*, 100(6):060405, 2019.

[6] Y Kasahara, T Ohnishi, Y Mizukami, O Tanaka, Sixiao Ma, K Sugii, N Kurita, H Tanaka, J Nasu, Y Motome, et al. Majorana quantization and half-integer thermal quantum hall effect in a kitaev spin liquid. *Nature*, 559(7713):227–231, 2018.

[7] Arnab Banerjee, Paula Lampen-Kelley, Johannes Knolle, Christian susceptometry, Adam Anthony Aczel, Barry Winn, Yaohua Liu, Daniel Pajerowski, Jiaqiang Yan, Craig A Bridges, et al. Excitations in the field-induced quantum spin liquid state of α-$RuCl_3$. *npj Quantum Materials*, 3(1):8, 2018.

[8] Nityan L Nair, Eran Maniv, Caolan John, Spencer Doyle, Joseph Orenstein, and James G Analytis. Electrical switching in a magnetically intercalated transition metal dichalcogenide. *Nature materials*, pages 1–5, 2019.

[9] Nicola Spaldin. Hidden, entangled, and resonating order, 12/19/2019. Seminar given at the Molecular Foundry, Lawrence Berkeley Lab.

[10] Louis Nèel. Magnetism and the local molecular field. https://www.nobelprize.org/prizes/physics/1970/neel/lecture/, 12/11/1970. Nobel Lecture, December 11, 1970.

[11] Charles Kittel. *Introduction to Solid State Physics*. John Wiley and Sons, 1971.

[12] C Gi Shull, WA Strauser, and EO Wollan. Neutron diffraction by paramagnetic and antiferromagnetic substances. *Physical Review*, 83(2):333, 1951.

[13] Philip W Anderson. Resonating valence bonds: A new kind of insulator? *Materials Research Bulletin*, 8(2):153–160, 1973.

[14] Philip W Anderson. The resonating valence bond state in La2CuO4 and superconductivity. *science*, 235(4793):1196–1198, 1987.

[15] Patrick A Lee, Naoto Nagaosa, and Xiao-Gang Wen. Doping a Mott insulator: Physics of high-temperature superconductivity. *Reviews of modern physics*, 78(1):17, 2006.

[16] T. Jungwirth, X. Marti, P. Wadley, and J. Wunderlich. Antiferromagnetic spintronics. *Nature Nanotechnology*, 11(3):231–241, 2016. ISSN 17483395. doi: 10.1038/nnano.2016.18. URL http://dx.doi.org/10.1038/nnano.2016.18.

[17] M. S. Dresselhaus. *Solid State Physics Part II Optical Properties of Solids*. 2001. Available at: http://web.mit.edu/course/6/6.732/www/6.732-pt2.pdf.

[18] Assa Auerbach. *Interacting electrons and quantum magnetism*. World Pub. Corp., 2009.

[19] John Hubbard. Electron correlations in narrow energy bands. *Proceedings of the Royal Society of London. Series A. Mathematical and Physical Sciences*, 276(1365):238–257, 1963.

[20] PW Anderson. Antiferromagnetism. theory of superexchange interaction. *Physical Review*, 79(2):350, 1950.

[21] Nevill F Mott. The basis of the electron theory of metals, with special reference to the transition metals. *Proceedings of the Physical Society. Section A*, 62(7):416, 1949.

[22] Wolfgang Nolting and Anupuru Ramakanth. *Quantum theory of magnetism*. Springer, 2009.

[23] GH Wannier. Antiferromagnetism. the triangular Ising net. *Physical Review*, 79(2):357, 1950.

[24] Tôru Moriya. Anisotropic superexchange interaction and weak ferromagnetism. *Physical review*, 120(1):91, 1960.

[25] Igor Dzyaloshinsky. A thermodynamic theory of weak ferromagnetism of antiferromagnetics. *Journal of Physics and Chemistry of Solids*, 4(4):241–255, 1958.

[26] Jeffrey G. Rau, Eric Kin-Ho Lee, and Hae-Young Kee. Generic spin model for the honeycomb iridates beyond the kitaev limit. *Physical Review Letters*, 112:077204, Feb 2014.

[27] Leon Balents. Spin liquids in frustrated magnets. *Nature*, 464(7286):199–208, 2010.

[28] A. Little, Liang Wu, P. Lampen-Kelley, A. Banerjee, S. Patankar, D. Rees, C. A. Bridges, J.-Q. Yan, D. Mandrus, S. E. Nagler, and J. Orenstein. Antiferromagnetic resonance and terahertz continuum in α-$RuCl_3$. *Physical Review Letters*, 119:227201, Nov 2017. URL https://link.aps.org/doi/10.1103/PhysRevLett.119.227201.

[29] Liang Wu, Arielle Little, Erik E Aldape, Dylan Rees, Eric Thewalt, Paula Lampen-Kelley, Arnab Banerjee, Craig A Bridges, J-Q Yan, Derrick Boone, et al. Field evolution of magnons in α- $RuCl_3$ by high-resolution polarized terahertz spectroscopy. *Physical Review B*, 98(9):094425, 2018. URL https://journals.aps.org/prb/abstract/10.1103/PhysRevB.98.094425.

[30] Arielle Little, Changmin Lee, Caolan John, Spencer Doyle, Eran Maniv, Nityan L Nair, Wenqin Chen, Dylan Rees, Jörn WF Venderbos, Rafae Fernandes, James G. Analytis, and Joseph Orenstein. Three-state nematicity in the triangular lattice antiferromagnet $Fe_{1/3}NbS_2$. *Nature Materials*, 2020. doi: https://doi.org/10.1038/s41563-020-0681-0.

[31] Lucile Savary and Leon Balents. Quantum spin liquids. *arXiv:1601.03742*, 2016.

[32] Subir Sachdev. Quantum magnetism and criticality. *Nature Physics*, 4(3):173–185, 2008.

[33] Tian-Heng Han, Joel S Helton, Shaoyan Chu, Daniel G Nocera, Jose A Rodriguez-Rivera, Collin Broholm, and Young S Lee. Fractionalized excitations in the spin-liquid state of a kagome-lattice antiferromagnet. *Nature*, 492(7429):406–410, 2012.

[34] Stephen M Winter, Ying Li, Harald O Jeschke, and Roser Valentí. Challenges in design of Kitaev materials: Magnetic interactions from competing energy scales. *Physical Review B*, 93(21):214431, 2016.

[35] A Yu Kitaev. Fault-tolerant quantum computation by anyons. *Annals of Physics*, 303(1): 2–30, 2003.

[36] Alexei Kitaev. Anyons in an exactly solved model and beyond. *Annals of Physics*, 321(1): 2–111, 2006.

[37] Alexei Kitaev and Chris Laumann. Topological phases and quantum computation. *Les Houches Summer School "Exact methods in low-dimensional physics and quantum computing*, 89:101, 2009.

[38] Jiří Chaloupka, George Jackeli, and Giniyat Khaliullin. Kitaev-heisenberg model on a honeycomb lattice: possible exotic phases in iridium oxides a 2 iro 3. *Physical Review Letters*, 105(2):027204, 2010.

[39] SC Williams, RD Johnson, F Freund, Sungkyun Choi, A Jesche, I Kimchi, S Manni, A Bombardi, P Manuel, P Gegenwart, et al. Incommensurate counterrotating magnetic order stabilized by kitaev interactions in the layered honeycomb α- Li_2IrO_3. *Physical Review B*, 93(19):195158, 2016.

[40] A Biffin, RD Johnson, I Kimchi, R Morris, A Bombardi, JG Analytis, A Vishwanath, and R Coldea. Noncoplanar and counterrotating incommensurate magnetic order stabilized by kitaev interactions in γ- Li_2IrO_3. *Physical Review Letters*, 113(19):197201, 2014.

[41] Kimberly A Modic, Tess E Smidt, Itamar Kimchi, Nicholas P Breznay, Alun Biffin, Sungkyun Choi, Roger D Johnson, Radu Coldea, Pilanda Watkins-Curry, Gregory T McCandless, et al. Realization of a three-dimensional spin–anisotropic harmonic honeycomb iridate. *Nature Communications*, 5, 2014.

[42] Tomohiro Takayama, Akihiko Kato, Robert Dinnebier, Jürgen Nuss, H Kono, LSI Veiga, G Fabbris, D Haskel, and H Takagi. Hyperhoneycomb Iridate β- Li_2IrO_3 as a Platform for Kitaev Magnetism. *Physical Review Letters*, 114(7):077202, 2015.

[43] KW Plumb, JP Clancy, LJ Sandilands, V Vijay Shankar, YF Hu, KS Burch, Hae-Young Kee, and Young-June Kim. α-$RuCl_3$: A spin-orbit assisted Mott insulator on a honeycomb lattice. *Physical Review B*, 90(4):041112, 2014.

[44] X Liu, T Berlijn, W-G Yin, W Ku, A Tsvelik, Young-June Kim, H Gretarsson, Yogesh Singh, P Gegenwart, and JP Hill. Long-range magnetic ordering in Na 2 IrO 3. *Physical Review B*, 83(22):220403, 2011.

[45] SK Choi, R Coldea, AN Kolmogorov, T Lancaster, II Mazin, SJ Blundell, PG Radaelli, Yogesh Singh, P Gegenwart, KR Choi, et al. Spin waves and revised crystal structure of honeycomb iridate Na_2IrO_3. *Physical Review Letters*, 108(12):127204, 2012.

[46] Sae Hwan Chun, Jong-Woo Kim, Jungho Kim, H Zheng, Constantinos C Stoumpos, CD Malliakas, JF Mitchell, Kavita Mehlawat, Yogesh Singh, Y Choi, et al. Direct evidence for dominant bond-directional interactions in a honeycomb lattice iridate Na2IrO3. *Nature Physics*, 11(6):462–466, 2015.

[47] Jennifer A Sears, M Songvilay, KW Plumb, JP Clancy, Y Qiu, Y Zhao, D Parshall, and Young-June Kim. Magnetic order in α-$RuCl_3$ a honeycomb-lattice quantum magnet with strong spin-orbit coupling. *Physical Review B*, 91(14):144420, 2015.

[48] Simon Trebst. Kitaev materials. *arXiv preprint arXiv:1701.07056*, 2017.

[49] Hidenori Takagi, Tomohiro Takayama, George Jackeli, Giniyat Khaliullin, and Stephen E Nagler. Concept and realization of kitaev quantum spin liquids. *Nature Reviews Physics*, 1(4):264–280, 2019.

[50] Ravi Yadav, Nikolay A Bogdanov, Vamshi M Katukuri, Satoshi Nishimoto, Jeroen Van Den Brink, and Liviu Hozoi. Kitaev exchange and field-induced quantum spin-liquid states in honeycomb α-$RuCl_3$. *Scientific Reports*, 6:37925, 2016.

[51] G Guizzetti, E Reguzzoni, and I Pollini. Fundamental optical properties of α-rucl3. *Physics Letters A*, 70(1):34–36, 1979.

[52] A Banerjee, CA Bridges, J-Q Yan, AA Aczel, L Li, MB Stone, GE Granroth, MD Lumsden, Y Yiu, J Knolle, et al. Proximate kitaev quantum spin liquid behaviour in a honeycomb magnet. *Nature Materials*, 2016.

[53] Kejing Ran, Jinghui Wang, Wei Wang, Zhao-Yang Dong, Xiao Ren, Song Bao, Shichao Li, Zhen Ma, Yuan Gan, Youtian Zhang, J. T. Park, Guochu Deng, S. Danilkin, Shun-Li Yu, Jian-Xin Li, and Jinsheng Wen. Spin-wave excitations evidencing the kitaev interaction in single crystalline α-$RuCl_3$. *Physical Review Letters*, 118:107203, Mar 2017.

[54] RD Johnson, SC Williams, AA Haghighirad, J Singleton, V Zapf, P Manuel, II Mazin, Y Li, HO Jeschke, R. Valentí, and R. Coldea. Monoclinic crystal structure of α-$RuCl_3$ and the zigzag antiferromagnetic ground state. *Physical Review B*, 92(23):235119, 2015.

[55] E. Stroganov and Vestn Leningrad. Univ. K. Ovchinnikov. *Fizika, Khimiya*, 12(152), 1957.

[56] Huibo B Cao, A Banerjee, J-Q Yan, CA Bridges, MD Lumsden, DG Mandrus, DA Tennant, BC Chakoumakos, and SE Nagler. Low-temperature crystal and magnetic structure of α-$RuCl_3$. *Physical Review B*, 93(13):134423, 2016.

[57] Yumi Kubota, Hidekazu Tanaka, Toshio Ono, Yasuo Narumi, and Koichi Kindo. Successive magnetic phase transitions in α-$RuCl_3$: XY-like frustrated magnet on the honeycomb lattice. *Physical Review B*, 91(9):094422, 2015.

[58] M. Ziatdinov, A. Banerjee, A. Maksov, T. Berlijn, W. Zhou, H. B. Cao, J. Q. Yan, C. A. Bridges, D. G. Mandrus, S. E. Nagler, A. P. Baddorf, and S. V. Kalinin. Atomic-scale observation of structural and electronic orders in the layered compound α-$RuCl_3$. *Nature Communications*, 7:13774, 12 2016.

[59] S-Y Park, S-H Do, K-Y Choi, D Jang, T-H Jang, J Schefer, C-M Wu, JS Gardner, JMS Park, J-H Park, et al. Emergence of the Isotropic Kitaev Honeycomb Lattice with Two-dimensional Ising Universality in α- $RuCl_3$. *arXiv preprint arXiv:1609.05690*, 2016.

[60] Jennifer Sears. *Neutron and X-ray Diffraction Studies of Structure and Magnetism in α-$RuCl_3$*. PhD dissertation, University of Toronto, 2017.

[61] Jennifer A Sears, Y Zhao, Z Xu, JW Lynn, and Young-June Kim. Phase diagram of α-$RuCl_3$ in an in-plane magnetic field. *Physical Review B*, 95(18):180411, 2017.

[62] Heung-Sik Kim and Hae-Young Kee. Crystal structure and magnetism in α- $RuCl_3$: An ab initio study. *Physical Review B*, 93(15):155143, 2016.

[63] Richard Hentrich, Anja UB Wolter, Xenophon Zotos, Wolfram Brenig, Domenic Nowak, Anna Isaeva, Thomas Doert, Arnab Banerjee, Paula Lampen-Kelley, David G Mandrus, et al. Large field-induced gap of Kitaev-Heisenberg paramagnons in α- $RuCl_3$. *arXiv preprint arXiv:1703.08623*, 2017.

[64] Jiacheng Zheng, Kejing Ran, Tianrun Li, Jinghui Wang, Pengshuai Wang, Bin Liu, Zheng-Xin Liu, B Normand, Jinsheng Wen, and Weiqiang Yu. Gapless spin excitations in the field-induced quantum spin liquid phase of α- RuCl 3. *Physical review letters*, 119(22): 227208, 2017.

[65] Paul M. Chaikin and T. C. Lubensky. *Principles of condensed matter physics*. Cambridge University Press, 2013.

[66] Mexthild Enderle. Neutrons and magnetism. https://www.neutron-sciences.org/articles/sfn/pdf/2014/01/sfn201401002.pdf, 2014.

[67] S-H Baek, S-H Do, K-Y Choi, Yong Seung Kwon, AUB Wolter, S Nishimoto, Jeroen van den Brink, and B Büchner. Evidence for a field-induced quantum spin liquid in α-$RuCl_3$. *Physical Review Letters*, 119(3):037201, 2017.

[68] Ian A Leahy, Christopher A Pocs, Peter E Siegfried, David Graf, S-H Do, Kwang-Yong Choi, B Normand, and Minhyea Lee. Anomalous Thermal Conductivity and Magnetic Torque Response in the Honeycomb Magnet α-$RuCl_3$. *Physical Review Letters*, 118(18): 187203, 2017.

[69] Luke J Sandilands, Yao Tian, Kemp W Plumb, Young-June Kim, and Kenneth S Burch. Scattering Continuum and Possible Fractionalized Excitations in α-$RuCl_3$. *Physical Review Letters*, 114(14):147201, 2015.

[70] G Baskaran, Saptarshi Mandal, and R Shankar. Exact results for spin dynamics and fractionalization in the kitaev model. *Physical Review Letters*, 98(24):247201, 2007.

[71] Johannes Knolle, DL Kovrizhin, JT Chalker, and Roderich Moessner. Dynamics of a two-dimensional quantum spin liquid: signatures of emergent majorana fermions and fluxes. *Physical Review Letters*, 112(20):207203, 2014.

[72] Johannes Knolle, DL Kovrizhin, JT Chalker, and R Moessner. Dynamics of fractionalization in quantum spin liquids. *Physical Review B*, 92(11):115127, 2015.

[73] Xue-Yang Song, Yi-Zhuang You, and Leon Balents. Low-energy spin dynamics of the honeycomb spin liquid beyond the Kitaev limit. *Physical Review Letters*, 117(3):037209, 2016.

[74] J Knolle, Gia-Wei Chern, DL Kovrizhin, R Moessner, and NB Perkins. Raman scattering signatures of Kitaev spin liquids in A_2IrO_3 iridates with A= Na or Li. *Physical Review Letters*, 113(18):187201, 2014.

[75] Gábor B Halász, Natalia B Perkins, and Jeroen van den Brink. Resonant inelastic X-ray scattering response of the Kitaev honeycomb model. *Physical Review Letters*, 117(12): 127203, 2016.

[76] Zhe Wang, S Reschke, D Hüvonen, S-H Do, K-Y Choi, M Gensch, U Nagel, T Rõõm, and A Loidl. Magnetic Excitations and Continuum of a Possibly Field-Induced Quantum Spin Liquid in α- RuCl 3. *Physical Review Letters*, 119(22):227202, 2017.

[77] AN Ponomaryov, E Schulze, J Wosnitza, P Lampen-Kelley, A Banerjee, J-Q Yan, CA Bridges, DG Mandrus, SE Nagler, AK Kolezhuk, et al. Unconventional spin dynamics in the honeycomb-lattice material α-$RuCl_3$ High-field electron spin resonance studies. *Physical Review B*, 96(24):241107, 2017.

[78] A. U. B. Wolter, L. T. Corredor, L. Janssen, K. Nenkov, S. Schönecker, S.-H. Do, K.-Y. Choi, R. Albrecht, J. Hunger, T. Doert, M. Vojta, and B. Büchner. Field-induced quantum criticality in the kitaev system α-$RuCl_3$. *Phys. Rev. B*, 96:041405, Jul 2017.

[79] Daichi Hirobe, Masahiro Sato, Yuki Shiomi, Hidekazu Tanaka, and Eiji Saitoh. Magnetic thermal conductivity far above the néel temperature in the kitaev-magnet candidate α-RuCl 3. *Physical Review B*, 95(24):241112, 2017.

[80] Richard Hentrich, Anja U. B. Wolter, Xenophon Zotos, Wolfram Brenig, Domenic Nowak, Anna Isaeva, Thomas Doert, Arnab Banerjee, Paula Lampen-Kelley, David G. Mandrus, Stephen E. Nagler, Jennifer Sears, Young-June Kim, Bernd Büchner, and Christian Hess. Unusual Phonon Heat Transport in α-$RuCl_3$ Strong Spin-Phonon Scattering and Field-Induced Spin Gap. *Physical Review Letters*, 120:117204, Mar 2018. doi: 10.1103/PhysRevLett.120.117204.

[81] Y. J. Yu, Y. Xu, K. J. Ran, J. M. Ni, Y. Y. Huang, J. H. Wang, J. S. Wen, and S. Y. Li. Ultralow-temperature thermal conductivity of the kitaev honeycomb magnet α-$RuCl_3$ across the field-induced phase transition. *Physical Review Letters.*, 120:067202, Feb 2018.

[82] Jonathan Cookmeyer and Joel E Moore. Spin-wave analysis of the low-temperature thermal Hall effect in the candidate Kitaev spin liquid α- RuCl 3. *Physical Review B*, 98(6): 060412, 2018.

[83] T Yokoi, S Ma, Y Kasahara, S Kasahara, T Shibauchi, N Kurita, H Tanaka, J Nasu, Y Motome, C Hickey, et al. Half-integer quantized anomalous thermal Hall effect in the Kitaev material α- $RuCl_3$. *arXiv preprint arXiv:2001.01899*, 2020.

[84] Martin C Nuss and Joseph Orenstein. Terahertz time-domain spectroscopy. In *Millimeter and submillimeter wave spectroscopy of solids*, pages 7–50. Springer, 1998.

[85] John Corson. *Advances in Terahertz Spectroscopy of High-T_c Superconductors*. PhD dissertation, University of California, Berkeley, 2000.

[86] Ingrid Wilke and Suranjana Sengupta. Nonlinear optical techniques for terahertz pulse generation and detection: Optical rectication and electrooptic sampling. In *Terahertz Spectroscopy*, pages 59–90. CRC press, 2017.

[87] M. Hoffman. *Novel Techniques in THz-Time-Domain-Spectroscopy*. PhD dissertation, Universit at Freiburg im Breisgau, 2006.

[88] Lucas Bilbro. *Fluctuations of Superconductivity in $La_{2-x}Sr_xCuO_4$*. PhD dissertation, The Johns Hopkins University, 2012.

[89] Lionel Duvillaret, Frédéric Garet, and J-L Coutaz. A reliable method for extraction of material parameters in terahertz time-domain spectroscopy. *IEEE Journal of selected topics in quantum electronics*, 2(3):739–746, 1996.

[90] Zero padding does not buy spectral resolution. http://www.ni.com/tutorial/4880/en/. Accessed: 2020-01-01.

[91] The effect of dispersion on ultrashort pulses. https://www.newport.com/n/the-effect-of-dispersion-on-ultrashort-pulses. Accessed: 2020-01-01.

[92] Eric Thewalt. *Mapping nematic order in $BaFe_2(As,P)_2$*. PhD dissertation, University of California, Berkeley, 2018.

[93] NJ Laurita, Bing Cheng, R Barkhouser, VA Neumann, and NP Armitage. A modified 8f geometry with reduced optical aberrations for improved time domain terahertz spectroscopy. *Journal of Infrared, Millimeter, and Terahertz Waves*, 37(9):894–902, 2016.

[94] User guide, photoconductive antenna transmitter and receiver modules. TeTechS antenna user manual.

[95] N Tamura, AA MacDowell, R Spolenak, BC Valek, JC Bravman, WL Brown, RS Celestre, HA Padmore, BW Batterman, and JR Patel. Scanning x-ray microdiffraction with submicrometer white beam for strain/stress and orientation mapping in thin films. *Journal of Synchrotron Radiation*, 10(2):137–143, 2003.

[96] F Keffer and Ch Kittel. Theory of antiferromagnetic resonance. *Physical Review*, 85(2): 329, 1952.

[97] Takeo Nagamiya. Theory of antiferromagnetism and antiferromagnetic resonance absorption, i. *Progress of Theoretical Physics*, 6(3):342–349, 1951.

[98] IS Jacobs, S Roberts, and PE Lawrence. Antiferromagnetic resonance in CoCl2 and FeCl2. *Journal of Applied Physics*, 36(3):1197–1198, 1965.

[99] Arnab Banerjee, Jiaqiang Yan, Johannes Knolle, Craig A Bridges, Matthew B Stone, Mark D Lumsden, David G Mandrus, David A Tennant, Roderich Moessner, and Stephen E Nagler. Neutron scattering in the proximate quantum spin liquid α-$RuCl_3$. *Science*, 356(6342):1055–1059, 2017.

[100] Stephan Reschke, Franz Mayr, Sebastian Widmann, Hans-Albrecht Krug von Nidda, Vladimir Tsurkan, Mikhail V Eremin, Seung-Hwan Do, Kwang-Yong Choi, Zhe Wang, and Alois Loidl. Sub-gap optical response in the Kitaev spin-liquid candidate α-RuCl3. *Journal of Physics: Condensed Matter*, 30(47):475604, 2018.

[101] S Reschke, F Mayr, Zhe Wang, Seung-Hwan Do, K-Y Choi, and A Loidl. Electronic and phonon excitations in α-$RuCl_3$. *Physical Review B*, 96(16):165120, 2017.

[102] M Sparks, DF King, and DL Mills. Simple theory of microwave absorption in alkali halides. *Physical Review B*, 26(12):6987, 1982.

[103] E Helgren, NP Armitage, and G Grüner. Frequency-dependent conductivity of electron glasses. *Physical Review B*, 69(1):014201, 2004.

[104] LN Bulaevskii, CD Batista, MV Mostovoy, and DI Khomskii. Electronic orbital currents and polarization in Mott insulators. *Physical Review B*, 78(2):024402, 2008.

[105] Andrew C Potter, T Senthil, and Patrick A Lee. Mechanisms for sub-gap optical conductivity in Herbertsmithite. *Physical Review B*, 87(24):245106, 2013.

[106] Daniel V Pilon, Chun Hung Lui, T-H Han, D Shrekenhamer, Alex J Frenzel, William J Padilla, Young S Lee, and Nuh Gedik. Spin-induced optical conductivity in the spin-liquid candidate herbertsmithite. *Physical Review Letters*, 111(12):127401, 2013.

[107] Adrien Bolens, Hosho Katsura, Masao Ogata, and Seiji Miyashita. Mechanism for subgap optical conductivity in honeycomb kitaev materials. *Physical Review B*, 97(16):161108, 2018.

[108] Adrien Bolens. Theory of electronic magnetoelectric coupling in $d5$ Mott insulators. *arXiv preprint arXiv:1805.02488*, 2018.

[109] Stephen M Winter, Kira Riedl, David Kaib, Radu Coldea, and Roser Valentí. Probing α-$RuCl_3$ beyond magnetic order: Effects of temperature and magnetic field. *Physical Review Letters*, 120(7):077203, 2018.

[110] T. Holstein and H. Primakoff. Field dependence of the intrinsic domain magnetization of a ferromagnet. *Physical Review*, 58(12):1098–1113, 1940. doi: 10.1103/physrev.58.1098.

[111] J.h.p. Colpa. Diagonalization of the quadratic boson hamiltonian. *Physica A: Statistical Mechanics and its Applications*, 93(3-4):327–353, 1978. doi: 10.1016/0378-4371(78)90160-7.

[112] Wei Wang, Zhao-Yang Dong, Shun-Li Yu, and Jian-Xin Li. Theoretical investigation of magnetic dynamics in α-$RuCl_3$. *Phys. Rev. B*, 96:115103, Sep 2017. doi: 10.1103/PhysRevB.96.115103. URL https://link.aps.org/doi/10.1103/PhysRevB.96.115103.

[113] Stephen M Winter, Kira Riedl, Pavel A Maksimov, Alexander L Chernyshev, Andreas Honecker, and Roser Valentí. Breakdown of magnons in a strongly spin-orbital coupled magnet. *Nature Communications*, 8(1):1152, 2017.

[114] S Toth and B Lake. Linear spin wave theory for single-q incommensurate magnetic structures. *Journal of Physics: Condensed Matter*, 27(16):166002, 2015. doi: 10.1088/0953-8984/27/16/166002.

[115] Takafumi Suzuki and Sei-ichiro Suga. Effective model with strong kitaev interactions for α-$RuCl_3$. *Physical Review B*, 97(13):134424, 2018.

[116] S. E. Korshunov. Nature of phase transitions in the striped phase of a triangular-lattice Ising antiferromagnet. *Physical Review B - Condensed Matter and Materials Physics*, 72(14):1–10, 2005. ISSN 10980121. doi: 10.1103/PhysRevB.72.144417.

[117] Andrew Smerald, Sergey Korshunov, and Frédéric Mila. Topological Aspects of Symmetry Breaking in Triangular-Lattice Ising Antiferromagnets. *Physical Review Letters*, 116(19):1–5, 2016. ISSN 10797114. doi: 10.1103/PhysRevLett.116.197201.

[118] Rafael M Fernandes and Jörn WF Venderbos. Nematicity with a twist: rotational symmetry breaking in a moir\'e superlattice. *arXiv preprint arXiv:1911.11367*, 2019.

[119] Sajedeh Manzeli, Dmitry Ovchinnikov, Diego Pasquier, Oleg V Yazyev, and Andras Kis. 2d transition metal dichalcogenides. *Nature Reviews Materials*, 2(8):17033, 2017.

[120] R. H. Friend, A. R. Beal, and A. D. Yoffe. Electrical and magnetic properties of some first row transition metal intercalates of niobium disulphide. *Philosophical Magazine*, 35(5):1269–1287, 1977. ISSN 00318086. doi: 10.1080/14786437708232952.

[121] S. S. Parkin and R. H. Friend. 3d transition-metal intercalates of the niobium and tantalum dichalcogenides i. Magnetic properties. *Philosophical Magazine B: Physics of Condensed Matter; Statistical Mechanics, Electronic, Optical and Magnetic Properties*, 41(1):65–93, 1980. ISSN 13642812. doi: 10.1080/13642818008245370.

[122] M. Eibschutz, S. Mahajan, F. J. Disalvo, G. W. Hull, and J. V. Waszczak. Ferromagnetism in metallic intercalated compounds FexTaS 2 (0.20<x<0.34). *Journal of Applied Physics*, 52(3):2098–2100, 1981. ISSN 00218979. doi: 10.1063/1.329629.

[123] O. Gorochov, A. Le Blanc-Soreau, J. Rouxel, P. Imbert, and G. Jehanno. Transport properties, magnetic susceptibility and mössbauer spectroscopy of Fe0 · 25NbS2 and Fe0 · 33NbS2. *Philosophical Magazine B: Physics of Condensed Matter; Statistical Mechanics, Electronic, Optical and Magnetic Properties*, 43(4):621–634, 1981. ISSN 13642812. doi: 10.1080/01418638108222164.

[124] Yoichi Horibe, Junjie Yang, Yong Heum Cho, Xuan Luo, Sung Baek Kim, Yoon Seok Oh, Fei Ting Huang, Toshihiro Asada, Makoto Tanimura, Dalyoung Jeong, and Sang Wook Cheong. Color theorems, chiral domain topology, and magnetic properties of FexTaS2. *Journal of the American Chemical Society*, 136(23):8368–8373, 2014. ISSN 15205126. doi: 10.1021/ja5026134.

[125] B Van Laar, HM Rietvel, and DJW Ijdo. Magnetic and crystallographic structures of MexNbS2 and MexTaS2. *J. Solid State Chem*, 3:154–160, 1971.

[126] S. Fan, I. Manuel, Amal Al-Wahish, K. R. O'Neal, K. A. Smith, C. J. Won, J. W. Kim, S. W. Cheong, J. T. Haraldsen, and J. L. Musfeldt. Electronic chirality in the metallic ferromagnet Fe1/3TaS2. *Physical Review B*, 96(20):1–6, 2017. ISSN 24699969. doi: 10.1103/PhysRevB.96.205119.

[127] Spencer Doyle, Caolan John, Eran Maniv, Ryan A. Murphy, Ariel Maniv, Sanath K. Ramakrishna, Yun-Long Tang, Ramamoorthy Ramesh, Jeffrey R. Long, Arneil P. Reyes, and James G. Analytis. Tunable Giant Exchange Bias in an Intercalated Transition Metal Dichalcogenide. 2019.

[128] P. Wadley, B. Howells, J. elezny, C. Andrews, V. Hills, R. P. Campion, V. Novak, K. Olejnik, F. Maccherozzi, S. S. Dhesi, S. Y. Martin, T. Wagner, J. Wunderlich, F. Freimuth, Y. Mokrousov, J. Kune , J. S. Chauhan, M. J. Grzybowski, A. W. Rushforth, K. W. Edmonds, B. L. Gallagher, and T. Jungwirth. Electrical switching of an antiferromagnet. *Science*, 351(6273):587–590, 2016. doi: 10.1126/science.aab1031.

[129] S. Yu Bodnar, L. Šmejkal, I. Turek, T. Jungwirth, O. Gomonay, J. Sinova, A. A. Sapozhnik, H. J. Elmers, M. Klaüi, and M. Jourdan. Writing and reading antiferromagnetic Mn 2 Au by Neél spin-orbit torques and large anisotropic magnetoresistance. *Nature Communications*, 9(1):1–7, 2018. ISSN 20411723. doi: 10.1038/s41467-017-02780-x.

[130] Takahiro Moriyama, Kent Oda, Takuo Ohkochi, Motoi Kimata, and Teruo Ono. Spin torque control of antiferromagnetic moments in NiO. *Scientific Reports*, 8(1):1–6, 2018.

[131] D. Kriegner, K. Výborný, K. Olejník, H. Reichlová, V. Novák, X. Marti, J. Gazquez, V. Saidl, P. Němec, V. V. Volobuev, G. Springholz, V. Holý, and T. Jungwirth. Multiple-stable anisotropic magnetoresistance memory in antiferromagnetic MnTe. *Nature Communications*, 7:1–7, 2016. ISSN 20411723. doi: 10.1038/ncomms11623.

[132] D. Kriegner, K. Výborný, K. Olejník, H. Reichlová, V. Novák, X. Marti, J. Gazquez, V. Saidl, P. Němec, V. V. Volobuev, G. Springholz, V. Holý, and T. Jungwirth. Multiple-stable anisotropic magnetoresistance memory in antiferromagnetic MnTe. *Nature Communications*, 7:1–7, 2016. ISSN 20411723. doi: 10.1038/ncomms11623.

[133] J. Železný, H. Gao, K. Výborný, J. Zemen, J. Mašek, Aurélien Manchon, J. Wunderlich, Jairo Sinova, and T. Jungwirth. Relativistic néel-order fields induced by electrical current in antiferromagnets. *Physical Review Letters*, 113(15):1–5, 2014.

[134] J. Železný, H. Gao, Aurélien Manchon, Frank Freimuth, Yuriy Mokrousov, J. Zemen, J. Mašek, Jairo Sinova, and T. Jungwirth. Spin-orbit torques in locally and globally noncentrosymmetric crystals: Antiferromagnets and ferromagnets. *Physical Review B*, 95 (1):1–18, 2017.

[135] S. Mankovsky, S. Polesya, H. Ebert, and W. Bensch. Electronic and magnetic properties of 2H-NbS2 intercalated by 3d transition metals. *Physical Review B*, 94(18):1–8, 2016. ISSN 24699969. doi: 10.1103/PhysRevB.94.184430.

[136] Eduardo Fradkin, Steven A Kivelson, Michael J Lawler, James P Eisenstein, and Andrew P Mackenzie. Nematic fermi fluids in condensed matter physics. *Annu. Rev. Condens. Matter Phys.*, 1(1):153–178, 2010.

[137] R. M. Fernandes, A. V. Chubukov, J. Knolle, I. Eremin, and J. Schmalian. Preemptive nematic order, pseudogap, and orbital order in the iron pnictides. *Physical Review B - Condensed Matter and Materials Physics*, 85(2):1–31, 2012. ISSN 10980121. doi: 10.1103/PhysRevB.85.024534.

[138] Rafael M Fernandes, Peter P Orth, and Jörg Schmalian. Intertwined vestigial order in quantum materials: Nematicity and beyond. *Annual Review of Condensed Matter Physics*, 10:133–154, 2019.

[139] Jiun-Haw Chu, James G Analytis, Kristiaan De Greve, Peter L McMahon, Zahirul Islam, Yoshihisa Yamamoto, and Ian R Fisher. In-plane resistivity anisotropy in an underdoped iron arsenide superconductor. *Science*, 329(5993):824–826, 2010.

[140] Morten H Christensen, Jian Kang, and Rafael M Fernandes. Intertwined spin-orbital coupled orders in the iron-based superconductors. *Physical Review B*, 100(1):014512, 2019.

[141] Eric Thewalt, Ian M. Hayes, James P. Hinton, Arielle Little, Shreyas Patankar, Liang Wu, Toni Helm, Camelia V. Stan, Nobumichi Tamura, James G. Analytis, and Joseph Orenstein. Imaging Anomalous Nematic Order and Strain in Optimally Doped BaFe2 (As, P)2. *Physical Review Letters*, 121(2), 2018.

[142] Andrey V Chubukov, David Pines, and Jörg Schmalian. A spin fluctuation model for d-wave superconductivity. *arXiv preprint arXiv:0201140*, 2002.

[143] JWF Venderbos. Symmetry analysis of translational symmetry broken density waves: Application to hexagonal lattices in two dimensions. *Physical Review B*, 93(11):115107, 2016.

[144] Rafael Fernandes and Jorn W.F. Venderbos. Private communication. 4-20-2019.

[145] Matthias Hecker and Jörg Schmalian. Vestigial nematic order and superconductivity in the doped topological insulator Cu x Bi2Se3. *npj Quantum Materials*, 3(1):1–8, 2018. ISSN 23974648. doi: 10.1038/s41535-018-0098-z.

[146] M.E. Straley, J.P. and Fisher. Three-state Potts model and anomalous tricritical points. *Journal of Physics A Mathematical General*, 6:1310–1326, 1973. doi: 10.1088/0305-4470/6/9/007.

[147] Tomoya Higo, Huiyuan Man, Daniel B. Gopman, Liang Wu, Takashi Koretsune, Olaf M.J. Van 'T Erve, Yury P. Kabanov, Dylan Rees, Yufan Li, Michi To Suzuki, Shreyas Patankar, Muhammad Ikhlas, C. L. Chien, Ryotaro Arita, Robert D. Shull, Joseph Orenstein, and Satoru Nakatsuji. Large magneto-optical Kerr effect and imaging of magnetic octupole domains in an antiferromagnetic metal. *Nature Photonics*, 12(2):73–78, 2018. ISSN 17494893. doi: 10.1038/s41566-017-0086-z. URL http://dx.doi.org/10.1038/s41566-017-0086-z.

[148] V. Saidl, P. Němec, P. Wadley, V. Hills, R. P. Campion, V. Novák, K. W. Edmonds, F. Maccherozzi, S. S. Dhesi, B. L. Gallagher, F. Trojánek, J. Kuneš, J. Železný, P. Malý, and T. Jungwirth. Optical determination of the Néel vector in a CuMnAs thin-film antiferromagnet. *Nature Photonics*, 11(2):91–96, 2017. ISSN 17494893. doi: 10.1038/nphoton.2016.255.

[149] Performance of the cryostation microscope. https://www.montanainstruments.com/blog/article/1099/Performance-of-Cryostation-Microscope/. Accessed: 2020-01-01.

[150] AM Simpson and W Wolfs. Thermal expansion and piezoelectric response of pzt channel 5800 for use in low-temperature scanning tunneling microscope designs. *Review of scientific instruments*, 58(11), 1987.

[151] Clifford W. Hicks, Mark E. Barber, Stephen D. Edkins, Daniel O. Brodsky, and Andrew P. Mackenzie. Piezoelectric-based apparatus for strain tuning. *Review of Scientific Instruments*, 85(6), 2014. ISSN 10897623. doi: 10.1063/1.4881611.

[152] Kok Wee Song and Alexei E Koshelev. Surface nematic order in iron pnictides. *Physical Review B*, 94(9):094509, 2016.

[153] Fan Yang, Stephen F Taylor, Stephen D Edkins, Johanna Palmstrom, Ian R Fisher, and Benjamin L Lev. Imaging nematic transitions in iron-pnictide superconductors with a quantum gas. *arXiv preprint arXiv:1907.12601*, 2019.

[154] S. Yu. Bodnar, M. Filianina, S. P. Bommanaboyena, T. Forrest, F. Maccherozzi, A. A. Sapozhnik, Y. Skourski, M. Kläui, and M. Jourdan. Imaging of current induced N\'eel vector switching in antiferromagnetic Mn$_2$Au. *arXiv preprint at arXiv:1902.02063*, 2019.

[155] A. A. Sapozhnik, M. Filianina, S. Yu Bodnar, A. Lamirand, M. A. Mawass, Y. Skourski, H. J. Elmers, H. Zabel, M. Kläui, and M. Jourdan. Direct imaging of antiferromagnetic domains in Mn2Au manipulated by high magnetic fields. *Physical Review B*, 97(13):1–5, 2018. ISSN 24699969. doi: 10.1103/PhysRevB.97.134429.

PART III

APPENDIX

A

JANIS INSTRUMENTS CONTINUOUS FLOW CRYOSTAT

This appendix includes a description of how to cool down the Janis instruments continuous flow cryostat used in the Small THz system in room 358. Because there is not a detailed manual in the lab, and because most of our cryostats are cryo-free nowadays, this may become somewhat of a lost art.

This cryostat consists of an outer vacuum chamber (OVC), a helium line, and an inner sample space. Helium is inserted into the system from a dewar via a transfer line. Once a helium flow is established, liquid passes through a vaporizer and is emitted as gas into the sample space. The sample space is continuously pumped by a roughing pump hence "continuous flow". Helium is exhausted into the lab. To start using this system, you first need to pump down the OVC. This is done using one of the Pfeiffer turbo pumping stations in the lab. Ideally you will want to pump for several hours so that the OVC reaches around 10^{-5} Torr. For best results, you may consider continuously pumping the outer vacuum chamber with the turbo even while cooling. Attach the roughing pump to the sample space pumping port but do not begin pumping. Connect the roughing pump to the sample space pumping port, making sure to install a valve between the pumping line and the sample space.

To begin cooling, obtain a 60 L dewar of liquid Helium. Two people are needed to insert the transfer line into the dewar. Of the transfer lines in our lab, the long one works best. Flow through the transfer line is controlled by a needle valve, which may be progressively opened and closed by adjusting the knurled knob on the dewar end of the transfer line. Close the needle valve all the way by tightening the knob all the way up. Then unscrew the knob two full turns to open the needle valve (this is a good starting point). Have one person hold the dewar end of the line vertically above the dewar while standing on a stool, while the second holds the nozzle side. Lift both ends up simultaneously and slowly insert the line into the dewar. The introduction of the room-temperature transfer line into the dewar will build up pressure in the dewar, driving helium gas through the line. Insert the line into the dewar partially, its vertical position may be fixed using a optical post collar. Tighten the o-ring onto the dewar. Now you may either wait until you establish a flow of helium from the nozzle, or you may directly insert the nozzle into the helium transfer port of the cryostat and turn on the roughing pump. Monitor the dewar pressure (should not be more than 10-15 PSI). The temperature should slowly begin to drop. If the temperature does not drop, then you may have an ice blockage in your transfer line. The

only solution to this unfortunately is to remove the line, heat it up, and purge with dry nitrogen before starting again.

There is one heater+Cernox sensor combination installed on the sample stick itself, one on the vaporizer. Temperature is monitored with a "CryoCon" PID controller, which may control both sample and vaporizer temperature on two separate channels. This is connected via a round pin connector at the top of the cryostat. Typically we want to keep the vaporizer around liquid helium temperature, 4 K. When cooling initially the vaporizer temperature should start to drop before the sample temperature starts to drop. Often the vaporizer temperature will increase a small amount just before the sample starts to get cold. It is best to set both temperatures to 4 K on initial cooldown, and then control the sample temperature to do measurements. At low temperatures, ice will form around the valve connecting the roughing pump to the chamber.

You may find that you have to open the needle valve further and/or insert the transfer line deeper into the dewar (which also will change the dewar pressure) to achieve the desired temperature, but generally operation in the regime of 4 -30 K is quite straightforward. For some reason the PID stability is worse in the range of about 60-150 K, it can take a long time for the temperature to stabilize in this range. Tweaking needle valve/ dewar pressure is usually necessary.

One neat feature of this cryostat is that, if you have enough liquid Helium, you can actually take measurements at 2 K. To do this open the needle valve all the way, and tighten the valve to the rouging pump but not all the way. This will cause liquid Helium to pool in the sample space, which you will be able to see through the quartz windows on cryostat. The helium will appear quite turbulent. Once you have a liquid level above the sample, reduce the flow through needle valve and slowly open the valve to the roughing pump. This will reduce the pressure in the chamber, allowing the helium temperature to drop below 4 K. You can actually watch the superfluid phase transition occur with your own eyes– When the temperature reaches 2 K, the liquid in the chamber will change sharply from bubbly turbulence to perfectly transparent tranquility. Once the superfluid phase is achieve, do your measurements quickly– this takes a lot of Helium and will only last a short time!

B

CRYO-FREE MAGNET CRYOSTAT

My first project in this group involved a good deal of archaeology in trying to resurrect an two old wet cryo superconducting magnets, both from Oxford Instruments. One of these magnets came from another group and was determined to have a helium leak in one of the welds– it has since been sent to salvage. The second magnet was left outdoors for years by LBL facilities and provided an excellent home for several spiders. If anyone is interested, that magnet is still in the lab, in a large crate next to the door in room 358. I had an extremely difficult time finding any documentation with respect to that instrument. Good luck!

As I result I am writing here, in case it is for some reason lost, the serial number for our currently function Janis system which is 7TL-CF-XOM-12. All relevant drawings and dimensions should be retrievable from Janis Instruments upon request, should they not be located in the lab. Most information, manuals, and tools regarding the magnet should be found in a large blue RubberMaid container located in the lab.

In the early days of using this system, we had an unfortunate accident which quenched the magnet. A screw driver was left on the optical table near the coil, and was pulled in through the optical window when the field was energized. Fortunately the coil wasn't damaged but the layers of Mylar insulation were completely destroyed and the magnet had to be shipped back to Janis Instruments for repair. I share this story simply to state: when the magnet is to be used again please follow the safety procedures. These are outlined in the Work Planning and Control (WPC) document for our lab. Field lines are marked on the floor of the lab. Check, double check, and check a third time for any magnetic tools in the vicinity of the magnet before energizing the field.

Finally, I'd like to note two concerns which may be of interest for those wishing to use the magnet in the future. First, the CVD diamond windows are possibly depolarizing at optical frequencies. This has not yet been investigated in great detail, but it is something that should be quantified. Changing the inner windows is not simple – it must be preformed by a technician from Janis instruments as failure of these windows while the coil is energized will result in a quenching of the magnet. Second, the pulse tube cooler which provides the cooling power for the coil introduces significant vibrations to the sample. While this is not an issue for THz measurements because both the sample and spot size are large, it will be an issue for stability in measurements in at IR/visible wavelengths.

C

UNIAXIAL STRAIN DEVICE

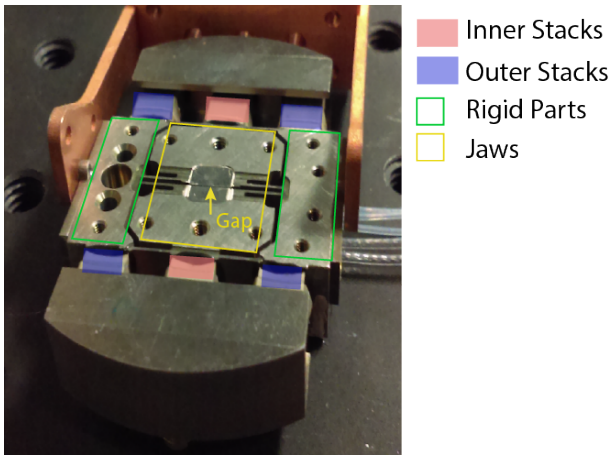

Figure C.1: Photo of the strain rig with no sample mounted. Red and blue overlaid rectangles indicated the location of the inner and out piezo stacks, respectively. Yellow box indicates the mobile jaws of the device, while green boxes indicated the rigid parts surrounding the jaws. A yellow arrow indicates the gap, which changes in size upon application of voltage to the piezos.

The uniaxial strain device (or the "rig") described here was designed and constructed by our collaborators in the Clifford Hicks group at Max Planck Institute (MPI) in Dresden. The basic operating principle of such devices is described in Ref. [151]. This appendix will describe how our rig may be integrated into our Montana Instruments 4 K cryostat– enabling optical measurements under applied strain. Note that for the strain measurements described in Chapter 4, strain was applied in a less sophisticated manner: samples were mounted directly to a piezo electric stack. The benefit of this direct mounting technique is that is relatively easy to implement. However as mentioned in Chapter 4, the piezo expands along its poling direction while cooling by about 0.1%. While voltage may be applied to the piezo to change the strain, due to this strain induced by expansion while cooling it may not be possible to tune the sample through zero applied strain.

Our rig is shown in Fig. C.1. It is model 1505B and was built in 2016 in Dresden. The rig is machined from Titanium– the body consists three connected Ti parts. In the center is a set flexible "jaws", over which the sample platform is mounted. On either side of the jaws is a rigid Ti part. These are coupled to the jaws via flexible connections. Six total piezos are used to apply uniaxial strain. The inner piezos are attached such that they directly push/pull on the flexible jaws, where a sample platform assembly is typically mounted (Fig. 1c shows the rig with no sample platform installed). The outer piezos pull/push on the rigid parts on either side of the jaws, providing additional strain. For example, to apply compressive strain, the inner piezos are driven at a positive voltage, $+V$ while the outer piezos are driven at $-2/3V$. Because the inner piezos push directly on the jaws and the outer piezos push on the rigid parts, driving the two sets of piezos at opposite voltages will apply strain in the same direction.

Uniaxial strain in the compressive or tensile direction is the change in length of the sample over the total sample length, $\Delta L/L$. This is monitored via a capacitive sensor integrated into the rig body. The "gap" between the jaws is measured by a capacitive sensor, which consists of two parallel titanium plates on opposing sides of the jaws. As the jaws move closer together or further apart, the capacitance measured between the two plates changes. We measure this capacitance using a Keysight LCR meter. The LCR meter settings used are as follows:

Setting	**Value**
Mode	C_p-D
Bias	0 V
Level	200 mV
Frequency	100 kHz
Meas. Time	Long

Table C.1: LCR meter settings

The area of the capacitor plates is $A = 5.28 \times 10^{-6}$ m^2. Capacitance is related to the gap, d, and the dielectric constant, ϵ_o by $d = (\epsilon_o A)/C$. A LabView program reads the capacitance and the corresponding gap. The distance between the plates at room temperature and zero applied voltage is typically in the range of 50 to 55 μm.

As measured at MPI, without a sample mounted, our rig will have a maximum gap of around 60 μ m and a minimum gap of around 7.5 μm.

C.1 INSTALLATION INTO THE MONTANA CRYOSTATION

To fit the rig in the Cryostation, the ATSM and z-attocube positioner will need to be removed. To raise the rig up to the appropriate height with respect to the top optical window, a set of aluminum spacers amounting to 6 mm of additional height is installed at the cryostat platform.

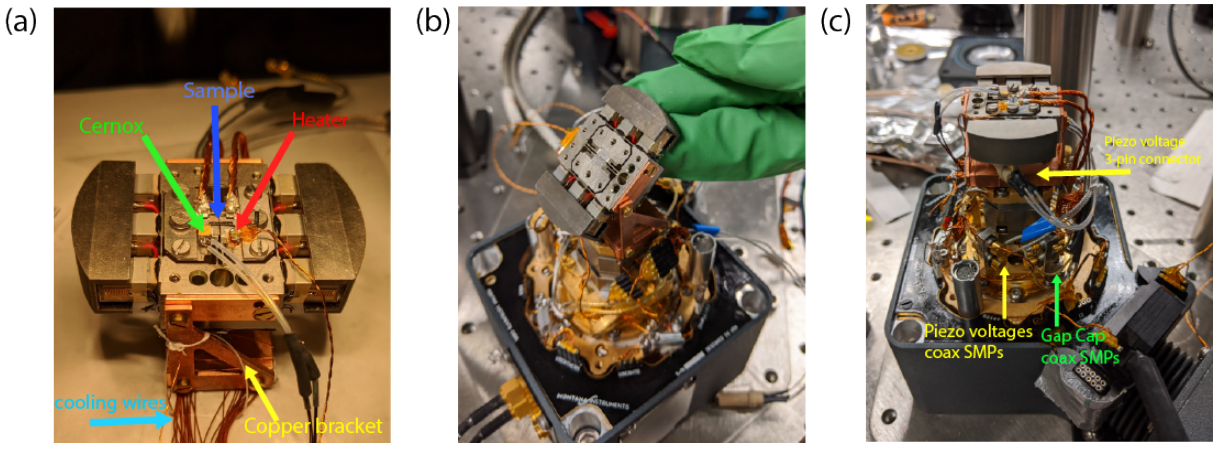

Figure C.2: (a) Rig and copper bracket assembly with a sample platform mounted. A Cernox temperature sensor and resistive heater are affixed the platform. Twisted copper wires are attached to the platform with silver epoxy. These will be clamped between the bracket assembly and flex platform to provide cooling power to the sample. (b) Photo of rig (no sample mounted) tilted up on bracket assembly to enable the tightening of bolts which affix the entire assembly onto Montana cryostation flex platform. (c) Photo showing cable routing. The three high voltage wires to the piezos are converted via a round pin (LEMO insert) connector to two coaxial cables, which are grounded to the cryostat. These, and the two coaxial connected to the gap capacitor are plugged into SMP connectors inside the cryostat, which are in turn routed out of the chamber via a SMP to SMA side panel. Cables are tied down with dental floss. Take care to route cables carefully as the radiation shield will be installed over the entire assembly.

The x and y attocube positioner are installed on top of the spacers, with the gold flex assembly platform installed on top of the attocubes. Finally, the copper bracket and rig assembly is bolted directly to the flex platform.

The rig is supported by a copper bracket (see Fig. C.2 (a)) which bolts into the flex platform. The rig is attached to the bracket on either side with a brass bolt. Cooling power is brought to the sample by copper wires which are epoxied onto the sample platform (see section below). These wires are bent and clamped flat between the rig bracket assembly and the flex platform as shown in Fig. C.2. Note that sample platform preparation and mounting (see below) must be done with the rig out of the cryostat. Once this step is complete the rig may be carefully transferred to the Cryostation.

To install the rig in the cryostation one of the brass bolts is removed, allowing the rig to pivot upward. This allows access to the two bolts which tighten the bracket assembly to the flex platform. One can hold the rig in place with one hand while tightening the bolts as shown in Fig. C.2 (b). After this is done, reinstall the second brass bolt to fix the rig horizontally.

Take care to route cables carefully as the radiation shield will be installed over the entire assembly. A photo of a successful cable-routing configuration is shown in Fig. C.2 (c). In particular, make sure that the copper cooling wires do not touch the radiation shield when it is installed, as this will reduce the already limited cooling power to the sample.

Note that because of the large size of the rig, it must sit a bit further below the top window of the cryostat than our typical sample stage. Focusing the laser on the sample requires the use of a longer-focal length objective, in this case an Olympus LMPlanFLN 10x, with focal length around 2 cm.

C.1.1 ELECTRICAL CONNECTIONS

There are five wires which come out of the rig body. Three of these wires are connected to the piezos: one for the inner stacks voltage, one for the outer stacks voltage, and one for the ground. These three wires are converted into two coaxial cables via a custom-made cable which connects to the round three-pin LEMO insert: the inner and outer stacks voltage wires go to the conductor of each coax and the ground goes to the coax shield. These are plugged into an SMP connector inside the cryostat (see Fig. C.2 (c)) and subsequently routed to the SMP to SMA feed-through side panel which brings the connections out of the cryostation. One can check if the connections to the piezo stacks are intact by measuring the capacitances across the round pin connector with a digital multimeter. The pin out is illustrated in Fig. C.3. The piezos are wired in parallel, so the capacitances add: two inner stacks should have a total capacitance of 1.35 uF while the four inner stacks should have a capacitance of 2.7 uF. [1]

1 Note: At the time of writing of this appendix, the outer piezos measure 1.8 uF, indicating that one of the stacks has become disconnected. This will be diagnosed and hopefully repaired shortly, however, note that should such a situation arise again it is possible to use the rig and apply a strain using only the inner piezos.

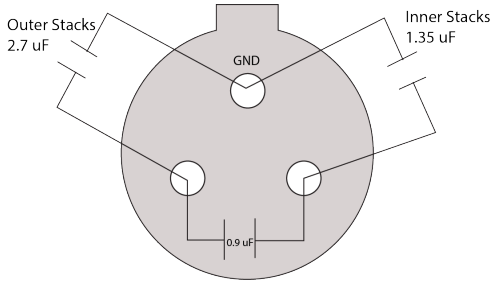

Figure C.3: Schematic of pinout for correct piezo capacitances on LEMO connector.

The other two wires coming out of the rig body are connected to either side of the gap capacitor, and go directly to coax. These are routed out through the same feed through panel and eventually are connected to the LCR meter.

There is additional wiring required for temperature control of the sample. With the z-attocube unplugged, there are two spare 5-pin single conductor feedthroughs in the cryostation which may be used. The two heater (resistor) leads are routed from the platform to one of the feedthrough plugs via a twisted pair. The nominal heater resistance is 100 Ω. The temperature sensor is a calibrated Cernox SD-1050 from Lake Shore. The two leads of the Cernox are sliced into a QuadLead cable to enable four-wire measurement– the nominal resistance at room temperature is around 63 Ω. The resulting four QuadLead connections are plugged into the second 5-pin feedthrough. The heater and thermometer are connected via a custom-made cable to a Lake Shore 350 PID temperature controller. The calibration curve for this particular Cernox sensor is stored on the controller and loaded in the Input B control loop. Leave Input A as is, it is configured for the ATSM stage.

C.2 DRIVING THE PIEZOS

The piezos are driven by a home-assembled high-voltage (HV) box, shown in Fig. C.4. Although home-assembled, this box is officially approved for use at LBL. The box consists of two identical Ultravolt low-current, bipolar power supplies which output -1000 to 1000 V. When connected to feedthrough panel, the HV power supply is grounded through cryostat ground– that is, the HV power supply and subsequently the rig piezos are all grounded to the cryostat platform and the rig body itself. The HV power supply is set by a LabView program which sets the auxiliary outputs of the Zurich Instruments lock-in amplifier, which provide control voltages which -10 to 10 V. The output of the power supply will be the control voltage multiplied by 100. Note that in order for the power supply to output a voltage, the voltage on the "Enable" input on the box must be set to a TTL high (at least 3.3 V). Black SMA cables, which are rated for HV, were purchased specifically for this application. The current supplied by the Ultravolt power supplies ranges from 0-600 μA, and may be set by applying a voltage of 0-10 V to the Current Limit

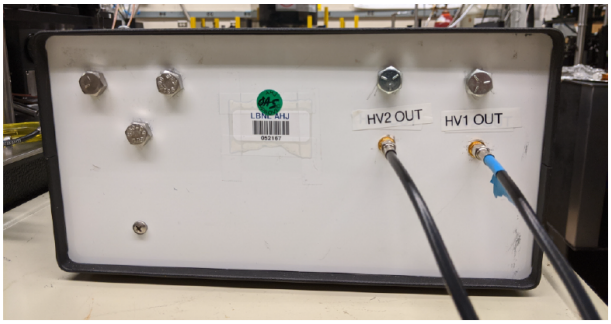

Figure C.4: High Voltage power supply for driving piezos. Note that HV connections are made using black SMA coaxial cables, which are rated for HV and were purchased for this application. HV1 drives the inner stacks, HV2 drives the outer stacks. Control voltages from the Zurich Instruments lock-in are provided via BNC connections on the back panel (not pictured).

input on the box. The current limit does not need to be set for the power supply to operate, but it is easy to set via LabView if desired.

As mentioned previously, for the best results, drive the piezos such that for an inner piezo voltage V, the outer piezos follow at $-2/3V$. However in some instances it may be necessary to control the voltages independently. For example, if working at room at room temperature, do not drive the piezos at more than +150 V or in the other direction, -20 V. Driving the piezo voltages at large negative values at room temperature risks de-poling the piezos. When cold, the piezo voltages may be increased to +600 V / -300 V.

In our current configuration, at cryogenic temperatures the piezos voltages are being set by a PID control with feedback based on the size of the gap as measured by the LCR meter. In our present configuration (using only the inner stacks) we are finding that at low temperatures it may take some time of applying voltage for the gap to reach a constant value. Additionally there is significant hysteresis when cycling from compressive to tensile strain. For example when only using the inner stacks we find after applying compressive strain it may take several hours of applying negative voltage for the gap to return to its nominal value. If the gap will not return to its equilibrium (zero-voltage) value (50-55 μm), it may be necessary to turn off the power supply and thermally cycle the piezos. Warming to 250 K should be sufficient to reset the equilibrium gap.

Note that, just like the attocube positioner piezos, the rig piezos must be grounded while changing the temperature of the rig over a large range, for example during the initial cooldown. While installed in the cryostat, the piezos may be grounded by plugging in a pair of SMA ground caps on the feedthrough panel. When uninstalled and in storage, the piezos should also be grounded– a ground cap which connects all three of the pin contacts on the round pin connector should be installed. This will minimize risk of accidental charging of the piezos.

C.3 SAMPLE MOUNTING AND TEMPERATURE CONTROL

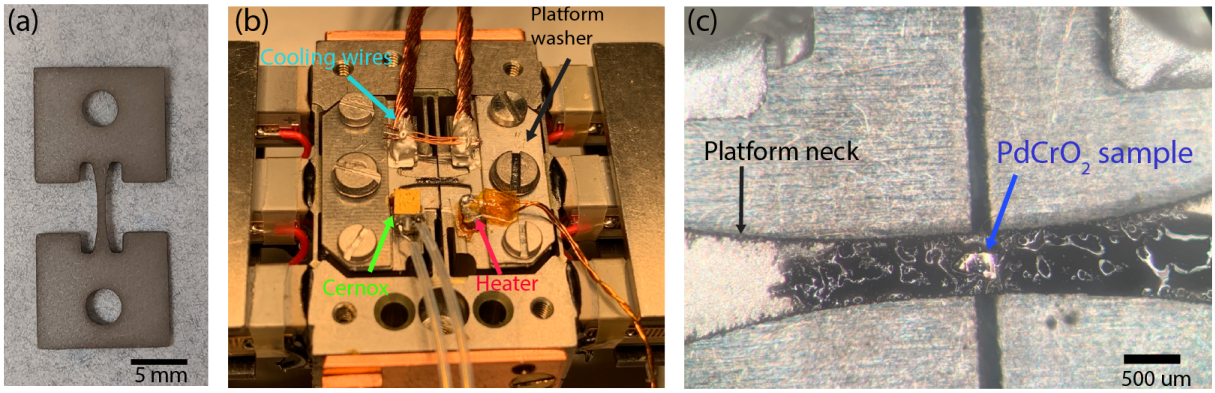

Figure C.5: (a) Narrow-neck Titanium platform. (b) Photo of sample and platform mounted onto the rig. The platform is affixed to the rig with a set of platform washers and six total (metric) titanium bolts. Cernox, heater, and cooling wires are installed for temperature control. (c) Microscope image of a μm $PdCrO_2$ sample mounted to platform with Stycast.

Samples may be mounted in a variety of ways. For example, samples are may be mounted on two opposing platforms attached to either side of the jaws, while the center of the sample is free standing above the gap. This is the standard configuration of the now commercially available Razorbill device.

While this is still a work-in-progress, for our rig, so far we have found that mounting the sample directly to a single platform with a narrow-neck design has proven simplest solution for our application, as shown in Fig. C.5 (a). Platforms are affixed the rig as shown in Fig. C.5 (b). Six metric bolts and a pair of Ti-foil clamps ("platform washers") are used to uniformly clamp the platform onto the rig. These platforms were originally intended for use with the pnictide superconductors, which we did study in the rig at room temperature in the microdiffraction beam line at the ALS. In general, these platforms will work well for transfer of strain to thin samples (tens of microns or thinner), for example $PdCrO_2$, as shown in Fig. C.5 (c), where a roughly 250 μm sample is mounted directly on the the 500 μm wide neck. A thin layer of epoxy (order of 1μm thick) is best for applying uniform strain. The sample in Fig. C.5 (c) is mounted atop a thin layer of filled Stycast 2850 epoxy. For better strain transfer it would be beneficial in the next iteration of the experiments to use the unfilled Stycast 1266, as it is less viscous and easier to apply a thin layer of epoxy.

While use of narrow-neck platform greatly simplifies the sample mounting procedure, this method does limit amount of strain that may be applied to the sample. In this case, the platform is being strained rather than the sample directly. Given strain is the change in length over total length, $\Delta L/L$, we can estimate the maximum total strain that can be applied to the

platform is roughly 50μm/5 mm, or 1 %. This is in principle a huge strain. But reality, this estimate ignores plastic deformation of the Ti-platform itself which becomes a factor at large strains (greater than 0.4%). This also assumes perfect strain transfer to the sample through the epoxy. While work on this is ongoing, we hope to achieve strains up to around 0.3% using this method.

The biggest challenge faced so far in using this device in conjunction with our optical measurements has been mounting the sample and implementing adequate cooling and temperature control. For transport measurements at MPI, strain rigs are cooled in Helium gas, so the entire rig, including the cools down. In contrast, in our cryostation it is necessary to develop a method of thermally linking the sample to the cold finger. In the present configuration, two twisted bundles of copper wires are affixed to the tabs protruding from beneath the platform washers on either end of the platform (see Fig. C.5 (b)) and are clamped between the rig assembly and cryostation flex platform (Fig. C.1). On the opposite side of the platform, a Cernox temperature sensor and heater are mounted with G-varnish. Both the Cernox and heater are mounted atop a small piece of cigarette paper, which provides electrical insulation between these components and the Ti platform while maintaining thermal contact.

The result of all this is: there is a lot of stuff glued to these platforms. Typically the order of operations for installing everything is as follows. First we affix the cooling wires to the platform with silver epoxy, and cure the epoxy in an oven. After the wires are affixed, we mount the sample in a thin layer of stycast, and wait for the epoxy to cure at room temperature. Finally, the Cernox temperature and heater are mounted. We have found oftentimes, it is even easier to affix the Cernox and heater to the platform in-situ, that is, with the rig already installed in the cryostation. This is because moving the rig and in and out of the cryostat, as well as installing the radiation shield, can cause stress to the wires and make these components fall off. It is also useful to be able to bend Cernox and heater the wires in-situ so as to minimize the stress applied to the components. After everything is arranged and the radiation shield installed, you can mount the cigarette paper and Cernox/heater to the platform with a very thin layer of G-varnish, one at a time. After placing the cernox/heater, press down on component with the wooden end of a cotton swab for several minutes. After the varnish has set for a few minutes initially, the cotton swab may be held in place with an optical card holder. We found it is best to leave everything in this position for 1.5 hours before moving on.

As mentioned, this is a work-in-progress: the cooling and temperature control scheme described here works to cool the sample down to around 24 K. Ideally, in the future we would like to be able to reach lower temperatures. An additional sticking point is the frequent failure of the resistive heater. The heater currently in use is a Vishay 100 Ω surface mount resistor with a 1 W power rating. In general is challenging to solder wire contacts to surface mount resistors– cold solder joints on the resistor pads can lead to local heating which will flow the solder and cause the leads to disconnect. To avoid this problem, solder contacts were made by a technician at the ALS. Nonetheless we find that the heater will still fail well below its power rating. Resistor heater fails with around 200 mW applied current. The result is with current configuration if the cryostat at its lowest achievable base temperature, we can only successfully heat the sample

up to 42 K. To scan to higher temperatures without compromising the heater it is necessary to change the base temperature of the cryostat itself, which can be time-consuming. While this is a work-able regime for our ongoing experiments on $PdCrO_2$, this is a problem that needs to be solved in the long run and may involve a different platform design or different choice of heater resistor.

C.3.1 PLATFORM FABRICATION

Narrow- neck Ti platforms were machined at Lawrence Berkeley Lab at the machine shop in Building 77. The design was copied from the one developed by then-MPI postdoc Joonbum Park. Platforms are machined out of 200 μm thick Titanium foil with a wire EDM cutter. There are several fresh platforms in the lab for future experiments, but should new platforms need to be machined it can be done on site if you provide the machinists at Bldg 77 with a CAD design, which can be be provided to future group members upon request. Titanium foil can be purchased directly from MacMaster-Carr.

For simpler platform designs without the delicate narrow-neck feature, such as for example the two opposing-side platforms used commonly in the Razorbill devices, it is possible that they may be fabricated (and quickly) at the machine shop in Building 2.